

UNCLASSIFIED



Australian Government

Department of Defence
Science and Technology

Development of a Low Strain-Rate Gun Propellant Bed Compression Test and its Use in Evaluating Propellant Mechanical Response

Joel R. Mortimer, Andrew H. Hart and Joel Huf

Weapons and Combat Systems Division
Defence Science and Technology Group

DST-Group-TR-3291

ABSTRACT

The mechanical integrity of the propellant bed is a key factor in safe and consistent gun performance. To inform in this regard, a low strain-rate bed compression test was developed, primarily for use at low temperatures and, in conjunction with the time-temperature superposition principle, to simulate the high strain rates that exist in the gun chamber during ignition. A range of single-base propellants was used to determine the appropriate test temperature, strain rate and maximum load to, as close as possible, simulate the mechanical response of the propellant bed during ignition in the gun. Results of this testing are given in terms of visual fracture categorisation, applied stress versus bed density, relative vivacity (following burning of crushed and reference samples) and stress relaxation. Artificial ageing programs were also employed to develop relationships between propellant mechanical integrity and propellant molecular weight distributions as a function of age.

RELEASE LIMITATION

Approved for public release

UNCLASSIFIED

UNCLASSIFIED

Produced by

*Weapons and Combat Systems Division
DST Group
PO Box 1500
Edinburgh SA 5111*

Telephone: 1300 333 362

*© Commonwealth of Australia 2016
AR-016-684
September 2016*

APPROVED FOR PUBLIC RELEASE

UNCLASSIFIED

UNCLASSIFIED

Development of a Low Strain-Rate Gun Propellant Bed Compression Test and its Use in Evaluating Propellant Mechanical Response

Executive Summary

The low strain-rate gun propellant test described in this report was developed under the auspices of Project JP2086 for the comparative assessment of propellants from the Mulwala Existing Facility (MEF) and Modernised Mulwala Facility (MMF) with respect to the effect of age on propellant bed mechanical integrity.

Two test configurations were designed, for small and large calibre natures respectively, based on similar designs found in the literature. Test fixture dimensions were selected such that bed response was able to be repeatably measured whilst also being able to apply representative loads to the propellant bed. The repeatability of test results was assessed for a range of propellant grain sizes and found to be satisfactory, although the largest grain form tested, BS-NACO, produced results indicating that its grain size was at the upper limit of that which could be repeatably tested. Procedures that were developed to ensure accurate and repeatable results are presented in this report, namely: bed packing methodology for optimal initial bed density; temperature conditioning duration determination to ensure homogenous bed conditions; and data analysis procedures to extract the propellant bed response from the measured combined bed and apparatus response.

The determination of the most appropriate test conditions, in terms of: strain rate (0.02 s^{-1}), maximum applied pressure (100 MPa for the small and 40 MPa for the large diameter assemblies) and test temperature (-60°C) was effected via a study of a range of single base propellant types of interest to Project JP2086, namely AR2211, AR2220, FNH-025 and BS-NACO over a range of temperatures (ambient, -15°C , -40°C and -60°C). The prime consideration in this determination was replication, as far as was possible, of the conditions expected to be present during ignition in the gun, keeping in mind the low operational temperature requirements of the aforementioned propellants in service. As brittleness is characteristic of propellant at the high strain rates involved in gun firings, the degree of brittleness was assessed via: visual inspection and categorisation of crushed samples to determine levels of fracture; inspection of applied stress versus bed density; bulk modulus versus applied stress; bulk modulus versus bed density; Heckel plots derived from the measured force versus piston displacement data; relative vivacity analysis of crushed samples fired in a closed vessel; and computation of time-temperature shift factors derived from stress relaxation measurements.

UNCLASSIFIED

Authors

Joel Mortimer

YTEK Pty Ltd.

Joel Mortimer completed a Bachelor of Engineering (Materials & Mechanical Systems) degree from the Australian National University in 2007. Joel has been a contractor within both Weapons Propulsion Group and Explosives and Pyrotechnics Group since 2011 and has worked on a breadth of S&T activities in each of the gun, rocket and explosives domains.

Andrew Hart

Weapons and Combat Systems Division

Andrew Hart completed a Bachelor of Engineering (Chemical) degree at the University of Adelaide in 2001. Andrew commenced work for DST Group in 2002 as a member of Weapons Propulsion Group where his work initially focussed on R&D relating to cast-composite rocket motors. The emphasis of his work then shifted to gun propellants, and for the past 8 years he has been involved in a wide range of gun propellant related research activities in support of defence acquisition programs and served as the DST Group S&T Advisor for Project JP2086 from 2010 until project closure in 2015.

Joel Huf

YTEK Pty Ltd.

Joel Huf completed a Bachelor of Engineering (Mechanical) degree from Monash University in 2010 and began working for YTEK providing contract services to the Weapons Propulsion and Explosives groups within DST Group in 2011. Since that time he has provided R&D support in the fields of energetic material sensitiveness; explosives and propellant production; propellant ageing, ballistic and mechanical property characterisation; as well as assisting in the commissioning of several new test facilities. He is also currently serving as a Combat Engineer in the Australian Army Reserves.

Contents

1. INTRODUCTION.....	1
2. EXPERIMENTAL	2
2.1 Propellants.....	2
2.2 Low Strain-Rate Bed Compression Test.....	3
2.2.1 Test Assembly	3
2.2.2 Choice of Bed Dimensions	5
2.2.3 Use of Release Agent.....	6
2.2.4 Bed Packing Method	7
2.2.5 Thermal Conditioning	9
2.2.6 Maximum Test Load	14
2.2.7 Data Analysis	14
2.2.7.1 Point of Initial Contact.....	15
2.2.7.2 Correction for Axial Compliance	17
2.2.7.3 Correction for Radial Compliance	22
2.3 Damage Induced Surface Area Evaluation	23
3. RESULTS AND DISCUSSION	24
3.1 Repeatability of Applied Stress versus %TMD.....	24
3.2 Choice of Test Temperature.....	31
3.2.1 Applied Stress versus %TMD Discussion.....	31
3.2.2 Visual Inspection	36
3.2.3 Time-Temperature Considerations.....	40
3.2.4 Stress Relaxation Data.....	42
3.3 Damage Induced Surface Area.....	46
3.3.1 Relative Vivacity Analysis	46
3.3.2 Effect of Molecular Weight Distribution.....	50
4. CONCLUSIONS AND RECOMMENDATIONS.....	57
5. ACKNOWLEDGEMENTS	58
6. REFERENCES	59
APPENDIX A ENGINEERING DRAWINGS	64
APPENDIX B ADIABATIC COMPRESSION CALCULATIONS.....	72
APPENDIX C PROPELLANT VISUAL INSPECTION.....	77
C.1 AR2211	77
C.2 AR2220	80
C.3 FNH-025	87

C.4 BS-NACO	91
APPENDIX D BULK MODULUS AND HECKEL PLOTS	103

Nomenclature

Symbol	Description
a	Burn rate coefficient
ADI	Australian Defence Industries
AISI	American Iron and Steel Institute
AOP	Allied Ordnance Publication
AR	Australian Rifle
$A_s(t)$	Instantaneous propellant burning surface area
DBP	Dibutylphthalate
dim_{max}	Maximum grain dimension
DISA	Damage Induced Surface Area
DNT	Dinitrotoluene
DOM	Date of Manufacture
DPA	Diphenylamine
DST	Defence Science and Technology
E	Young's modulus
EC	Ethyl Centralite
FNH	Flashless Non-Hygroscopic
GPC	Gel Permeation Chromatography
HRC	Rockwell C Hardness
k	Number of perforations
K_b	Bulk modulus
K_h	Heckel number
L	Grain length
L_0	Initial average grain length
ℓ_{bed}	Bed Height
M	Mass of propellant
$m_g(t)$	Instantaneous mass of combustion gases

$m_s(t)$	Instantaneous uncombusted propellant sample mass
<i>MEF</i>	Mulwala Existing Facility
<i>MMF</i>	Modernised Mulwala Facility
M_N	Number Average Molecular Weight
<i>MRP</i>	Mulwala Redevelopment Project
<i>MW</i>	Molecular Weight
M_W	Weight Average Molecular Weight
N	Number of tests
n	Burn rate exponent
<i>NACO</i>	Navy Cool
<i>NC</i>	Nitrocellulose
<i>NG</i>	Nitroglycerine
<i>NEQ</i>	Net Explosive Quantity
P	Closed vessel pressure after full combustion
<i>PDI</i>	Polydispersity Index
P_{max}	Maximum closed vessel pressure
P_{theory}	Theoretical maximum closed vessel pressure
$p(t)$	Instantaneous closed vessel pressure
p_o	Pressure external to compression die
p_i	Average internal compression die pressure
R	Universal gas constant ($8.314 \text{ J.K}^{-1}.\text{mol}^{-1}$)
r	Radial position
r_o	Outer die radius
r_i	Inner die radius
<i>SA</i>	Surface Area
<i>SR</i>	Secret Research
T	Temperature of gaseous combustion products
t	Time

TMD	Theoretical Maximum Density
$V(t)$	Dynamic vivacity
V_{cv}	Volume of empty closed vessel
V_{grain}	Volume of single propellant grain
$V_g(t)$	Instantaneous volume of combustion gases in closed vessel
$V_s(t)$	Instantaneous volume of unburned propellant in closed vessel
$x(t)$	Instantaneous linear depth burned
\bar{x}	Mean bed packing density
Δr	Change in die radius
σ	Standard deviation
σ_h	Hoop stress
σ_l	Longitudinal stress
σ_r	Radial stress
ϕ (or $\phi_{propellant}$)	Average grain diameter
ϕ_0	Average initial grain diameter
ϕ_{bed}	Bed diameter
ϕ_{p0}	Average initial perforation diameter
ρ	Grain density
ν	Poisson's ratio
%TMD	Percentage of theoretical maximum density
%TMD _{initial}	Initial percentage of theoretical maximum density

This page is intentionally blank

1. Introduction

In support of Project JP2086, Mulwala Redevelopment Project (MRP), a mechanical property (bed friability) test capability was developed to inform on the mechanical integrity of propellant produced at the Modernised Mulwala Facility (MMF). The test fixture design was based largely on tests developed at the Naval Surface Warfare Centre (NSWC) [1,2] and at the Aberdeen Proving Ground [3], which were used in various quasi-static compaction studies. Quasi-static compression is relatively simple to perform and is reported to provide good indications with respect to propellant bed behaviour during the first stages of ignition and combustion in a gun [4]. Although capable of testing a variety of propellant natures, the test commissioning activities reported herein were performed using only single-base propellants produced at the Mulwala Existing Facility (MEF), as it is propellants of this type that are of interest to Project JP2086.

Propellant bed structural integrity is a key factor in safe and consistent gun performance. As such, the ability to quantify propellant strength and the level of fracture induced by application of a representative mechanical load is of high value. Fracturing of propellant grains at any stage before or during a firing leads to an increase in the propellant surface area available for combustion, and hence higher peak pressures and erratic ballistic performance [4,5]. Single-base gun propellants are composed primarily of nitrocellulose (NC) long-chain molecules, with the strength of the propellant being primarily determined by the strength and molecular weight (MW) distribution of the polymer chains [6,7]. The NC chains are arranged in a semicrystalline manner, the degree of crystallinity being determined by characteristics of the neat NC and by the propellant manufacturing processes. For example the extrusion process, involving high shear stresses, induces molecular alignment parallel to the extrusion axis (in at least the outer grain layers) and hence there exists a degree of directionality in grain strength [8,9,10]. Extrusion and other manufacturing processes may also introduce flaws such as voids and cracks [11] which act as sites of stress concentration and potentially fracture initiation [5]. The NC polymer chains also break down with age and the resultant reduction in average MW reduces the strength of the propellant. Hence propellant composition, grain form, processing operations and age all contribute to the strength of the propellant.

As with all polymeric materials, temperature is a key factor in determining the response of a propellant to applied stress. As the temperature is lowered, the material transitions from ductile/plastic (predominately due to dislocation motion) to brittle (due to chemical rupture of bonds at the atomic level) modes of behaviour. NC is known to undergo such a transition gradually as the temperature is lowered from ambient [12], with the nature of the transition depending on the strain rate associated with the application of stress (lower strain rate leads to a lower glass transition temperature) [13]. Low temperature mechanical property testing is required as the brittle state caused by such temperatures is potentially of concern should it lead to excessive propellant fracture under dynamic ignition conditions in the gun [14,15]. The incorporation of plasticisers in the propellant can be used to lower the temperature at which the propellant transitions to the brittle state by dispersing small molecules between the large NC polymer chains, providing separation and 'free space' between the chains, which increases the slideability between chains [16,17,18].

In developing test conditions for strain rate, maximum applied stress and test temperature, the first consideration was that resultant modes of propellant response should be as close as possible to those encountered during a gun firing. In addition, it was desirable to use test conditions capable of producing damage induced surface area (DISA), at levels sufficient to aid detection by subsequent closed vessel analysis, in order to permit a comparative assessment between propellants.

2. Experimental

2.1 Propellants

Mechanical properties are reported for two Australian small-calibre propellants: AR2211 and AR2220, and two large calibre propellant natures: FNH-025 and BS-NACO. The small calibre propellant natures are diphenylamine (DPA) stabilised, dinitrotoluene (DNT) deterred single-base propellants manufactured with Grade C1 NC. Propellant FNH-025 is a DPA-stabilised, DNT-deterred, single-base propellant manufactured with Grade C1 NC, with a higher concentration of DNT than the small calibre propellants, although distributed homogeneously throughout the grain. BS-NACO is an ethyl centralite (EC) stabilised, single-base propellant, manufactured with the less highly nitrated Grade E NC.

Dimensional characteristics of the propellants are presented in Table 1. All testing was performed using propellant as received, besides grain density determination, which was by helium pycnometry with grains first ground and sieved, with material passing through a 1.00 mm sieve but retained on a 0.425 mm sieve tested as per Method 502/83 of [19]. The resulting ground and sieved propellant was then placed in the pycnometer sample holder, heated at 80°C for an hour to remove moisture, then desiccated for at least two hours over silica that had been recently activated, as per [20]. Density determinations were performed in quintuple, and the average values were used as approximations of theoretical maximum density (TMD) in the presentation of data. Grain dimensions are from lot information supplied by Thales.

Table 1: Propellant grain form, dimensions in mm

Propellant	Lot DOM	Grain Length	Grain Diameter	Perforations	TMD* (g/cm ³)
AR2211 MEM 5007	May '11	1.89	1.47	1	1.637 ± 0.005
AR2220 MEM 4326	Apr '05	2.74	1.73	1	1.632 ± 0.010
FNH-025 MEM 4003A	Aug '02	8.18	3.71	7	1.592 ± 0.004
BS-NACO MEM 4880	Jun '10	12.95	5.9	7	1.605 ± 0.007

*Quoted uncertainty is equal to 1.96 times the standard deviation of five averaged values.

2.2 Low Strain-Rate Bed Compression Test

2.2.1 Test Assembly

The assembly comprises a cylindrical die in which the granular propellant is contained and a close-fitting piston, positioned between the frame and crosshead of an Instron 5500R1185 universal materials tester. For this study, all tests were conducted at a constant bed strain rate of 0.02 s^{-1} (piston displacement rate divided by original bed height l_0 ; see Section 3.2.3 for a discussion of how this average strain rate is expected to manifest on the granular level), in accordance with that used by [3] in similar tests. Figure 1A shows a typical experimental setup.

Two versions of the test assembly have been manufactured: a larger diameter version, with an internal diameter of 50 mm, designed for testing large calibre gun propellants; and a smaller die assembly of 20 mm internal diameter for testing small calibre propellants. Engineering drawings are provided in Appendix A. The clearances between the outer diameter of the piston and the inner diameter of the die were designed to be as small as possible, to minimise the likelihood of the ingress and subsequent 'pinching' of crushed propellant fragments, whilst still permitting ease of piston insertion into the die. Clearances of 15 – 20 μm and 20 – 25 μm were used for the small and large diameter assemblies respectively. To mitigate against the hazards associated with the ingress of fine propellant fragments between the piston and die, a groove was incorporated into the piston design, 5 mm from the piston face, as shown in Figures A.3 and A.7, Detail A. Any propellant particles passing between the die wall and piston and reaching this groove would experience reduced frictional forces and therefore pose a lower likelihood of initiation. For the same reasons, the piston shafts were modified to have a 5 μm reduction in diameter compared with the ends of the pistons. The pistons were manufactured from AISI-D2 tool steel, hardened to 57 - 60 HRC. The die wall was manufactured from the same tool steel, but hardened to 50 - 54 HRC to prevent locking of the two components. Before testing, it was calculated that at the applied strain rates, propellant temperature increases due to adiabatic compression of the air in the die are negligible and so do not pose safety concerns (see Appendix B).

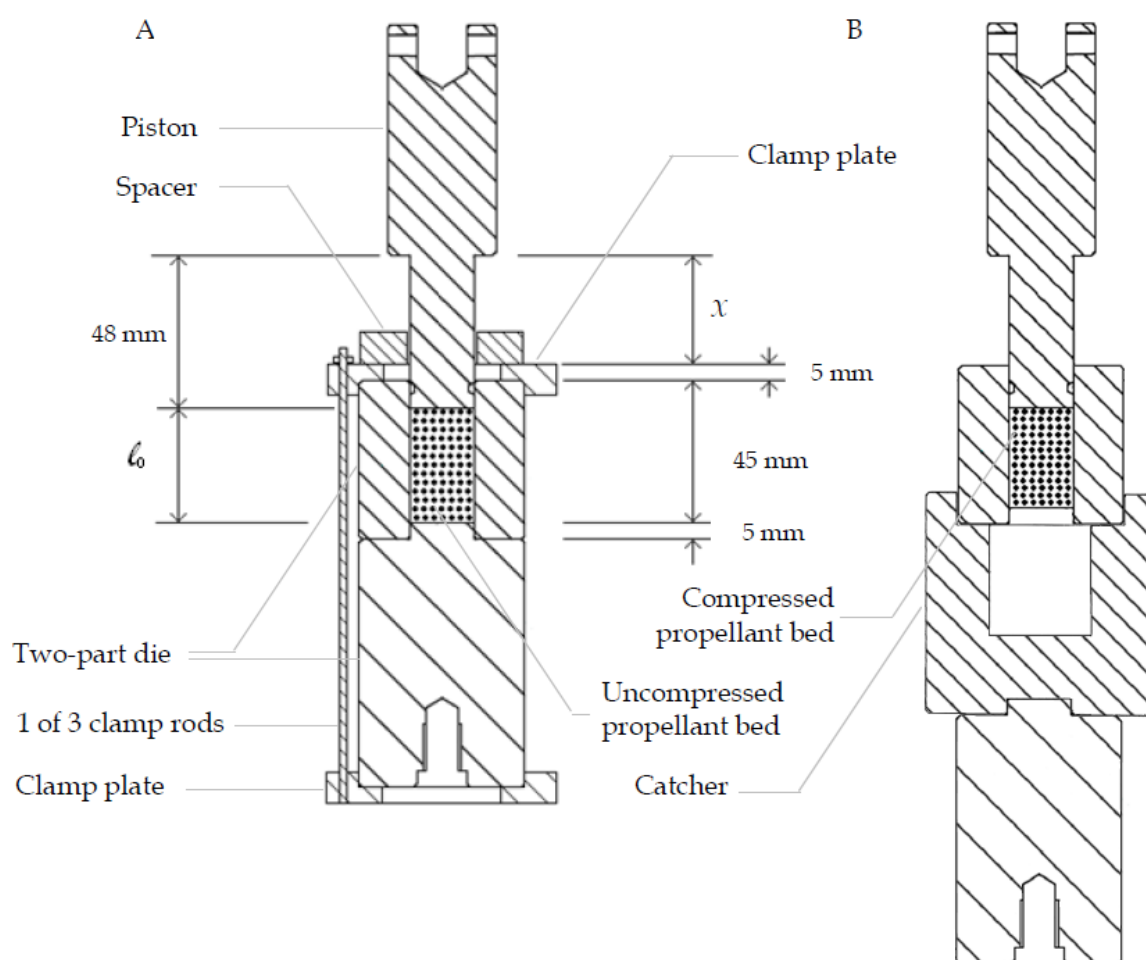


Figure 1: Low strain-rate bed compression test assembly section view (20 mm diameter assembly):
 A) assembly for bed compression; and B) assembly for sample removal.

As a safety precaution to prevent sample overcompression, synthetic resin bonded paper spacers were used as shown in Figure 1A and Figure 2. To ensure that bed expansion during removal of the applied load did not cause separation of the two-part die, clamps were integrated into the design as shown in Figure 1A. To facilitate sample removal, a two-piece die was designed, complete with catcher (Figure 1B), enabling remote sample removal at a constant rate. This feature was used for the samples crushed at ambient, at a rate of 30 mm/min. The samples crushed at cold temperatures underwent a combination of elastic deformation, along with a level of fracture, and so were able to be removed manually via gentle manipulation of the propellant bed with a laboratory spatula. Figure 2 shows a photograph of both large and small diameter test assemblies, complete with clamps and spacers.

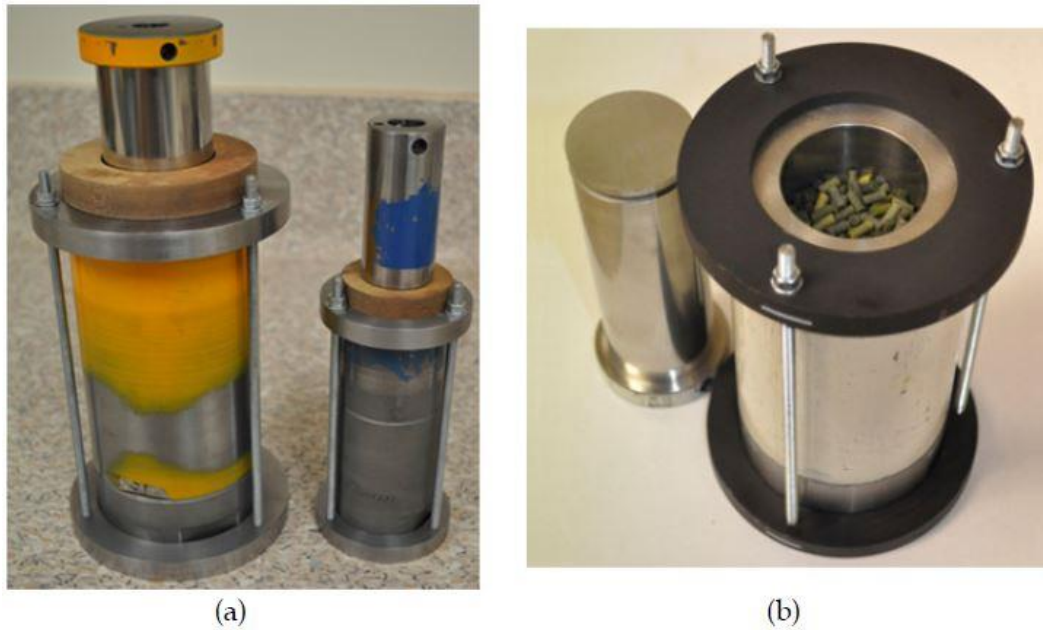


Figure 2: (a) Large (50 mm) and small diameter (20 mm) test assemblies, complete with clamps and spacers; (b) 50 mm test assembly with FNH-025 propellant bed.

2.2.2 Choice of Bed Dimensions

In order to reproducibly measure the mechanical response of a propellant bed, the influence of individual grains must be minimised. This requires use of a die with large bed dimensions relative to grain dimensions. Two bed compression studies from the literature were used to formulate heuristics to satisfy this requirement [2,3], with the more stringent of the two being adhered to for this study where possible, see Table 2.

Table 2: Comparison between bed design heuristics, die and propellant geometries from similar facilities reported in the literature [2,3] and the DST Group design.

	ℓ_{bed}^* (mm)	ϕ_{bed} (mm)	$\frac{L_{bed}}{dim_{max}}$	$\frac{\phi_{bed}}{dim_{max}}$	$\frac{\phi_{bed}}{\phi_{propellant}}$
Selected Heuristics			> 6	> 5	> 10
Ref. [2]	135 - 155	127.0	> 6.0	> 5.1	> 11.9
Ref. [3]	40	82.9	> 2.3	> 4.7	> 8.4
AR2211	31.7	20.0	16.8	10.6	13.6
AR2220	32.9	20.0	12.0	7.3	11.5
FNH-025	83.6	50.0	10.2	6.1	13.5
BS-NACO	80.5	50.0	6.2	3.9	8.4

*Bed height calculated using TMD from Table 1 and initial %TMD from Table 3 to calculate initial bulk density.

Each bed compression test was conducted using a fixed propellant mass (10 g for the small and 140 g for the large diameter test assemblies), to provide the required mass to achieve a loading density of 0.20 g/cm^3 in subsequent closed vessel firings (refer to Section 2.3). This resulted in bed height-to-largest propellant dimension ratios of at least 12.0 and at least 6.2 for the 20 mm and 50 mm diameter configurations respectively, satisfying the heuristic (ratio > 6). For the ratio of bed diameter to maximum grain dimension heuristic, this study achieved at least 7.3 and at least 3.9 for the 20 mm and 50 mm diameter configurations respectively. The 50 mm configuration fails the heuristic (ratio > 5) when BS-NACO is used. The third heuristic, that bed diameter-to-grain diameter ratio be maximised (ratio > 10), is formulated to avoid non-uniformity in bed porosity near the die wall [21] which may lead to increased variability in results [3]. BS-NACO again is the only propellant to fail this heuristic. The reason for BS-NACO failing the heuristic is that it was necessary to limit the die diameter of the large test fixture to 50 mm in order to achieve acceptable maximum test pressure. For the heuristic to have been met, a 60 mm diameter die would have been necessary, which would have limited the maximum test pressure to 35 MPa rather than the 50 MPa available with the current 50 mm diameter test assembly. The aforementioned load limits are dictated by the 100 kN capacity of the test frame. Section 3.1 assesses the repeatability in stress versus %TMD for the four aforementioned propellants.

2.2.3 Use of Release Agent

During commissioning with an inert small calibre gun propellant simulant composed of 91% cellulose acetate butyrate and 9% triacetin (TMD of 1.78 g/cm^3), compressed to between 30 and 50 MPa in the 50 mm dies, sample removal at rates of 10 to 30 mm/min proceeded in a 'jerky' fashion: audible shudder and an oscillating force-extension trace were noted, see Figure 3. This behaviour was not observed during removal of the same inert simulant from the 20 mm dies.

It was postulated that friction between the sample and die caused sample egress to proceed by a process of rapid stress buildup and release. As this is undesirable when using live material, use of a friction-reducing die coating was sought. Frekote 700-NC mold release agent by Loctite (Henkel) was chosen as it boasts a high slip, gloss finish with no contaminating transfer once cured. Use of this agent was found to facilitate smooth sample removal at a substantially reduced load. Figure 3 shows representative load traces for sample removal with and without the use of the mold release agent.

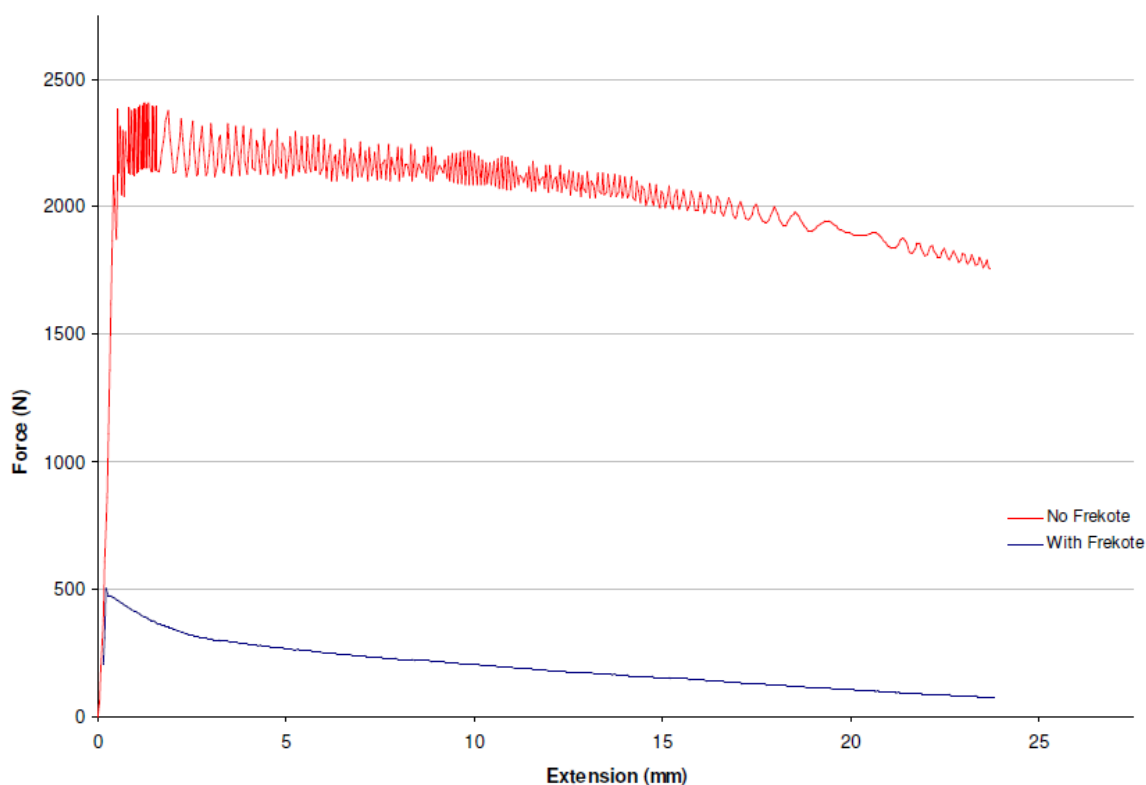


Figure 3: Influence of friction reducing agent on initial stages of sample removal from the die. Removal performed at 30 mm/mm in the 50 mm die with an inert propellant simulant.

A minimum of three layers of Frekote were applied to the inner die bore, with a minimum 10 minute curing time between applications. The Frekote was applied using a safewipe that had been immersed in the Frekote and wrapped around a rod of appropriate length and diameter. To ensure a uniform coating, after application the die was rolled continuously for two minutes while the majority of the solvent evaporated. After this time, any unevaporated drops were removed by gently dabbing with a dry safewipe and the dies then left to cure. After each 10 minute curing period, the inner bore was lightly polished with a dry safewipe and the piston passed through the die to ensure ease of insertion and passage. Any hindrance to the passage of the piston was taken as the end point of layer application. Frekote was periodically reapplied as considered necessary based upon visual inspection of the dies. No irregularities during sample removal were noted either audibly or in the load trace once the Frekote was employed.

2.2.4 Bed Packing Method

It is desirable to perform bed compression test with beds of reproducible initial packing density to aid comparison of results. Additionally, beds of maximal initial packing density are desired, as this reduces the amount of grain rearrangement that occurs during compression, and combined with similar initial packing density, will provide conditions conducive to achieving reproducible compression behaviour. Preliminary comparison of several bed packing methods was undertaken using BS-NACO. Methods trialled involved combinations of: pouring in a single stage; pouring in three stages; agitating the bed to

reduce voids created by the bridging of grains using either a vibrating table or by gently tapping the die assembly on the bench; and stirring and rearranging each layer. It was found that the most consistent and effective levels of bed consolidation were realised when the propellant was poured in three stages, tapping the die assembly on the bench and rearranging the top layer of grains with a laboratory spatula after each incremental propellant addition. Table 3 summarises the level and reproducibility of bed consolidation achieved using this method for each of the natures assessed in this study.

Table 3: Initial propellant packing densities. Propellant grain length-to-diameter ratios are also shown (\pm values are 1.96 times the standard deviation).

Propellant	L/ϕ	%TMD _{initial}	Data Points
AR2211	1.29	61.2 ± 0.7	8
AR2210	1.33	60.9 ± 0.8	4
AR2220	1.58	59.2 ± 1.0	8
FNH-025	2.20	53.7 ± 0.4	7
BS-NACO	2.19	2.2 ± 1.0	13

Bulk packing densities are known to increase as grain aspect ratio (L/ϕ) decreases towards unity [22], with evidence of a slight maximum around $L/\phi = 1.2$, based on Zhang's numerical 'collective rearrangement' simulations of rigid cylinders (see black trace, Figure 4) [22]. The propellant grains, whilst nominally cylindrical, are perforated and have some internal porosity, partly explaining the lower solid volume fractions of the red trace compared to the black trace. Additional factors that may contribute to this discrepancy include the effect of the die wall on reducing packing density (although see Section 2.2.2), and the possible counter-effect on packing density associated with the employed bed packing process and its effect on the local ordering of grains. Neither of these effects is modelled in [22]. Variability in grain length, diameter, cylindricity and surface roughness also influence the bed packing density. Another small calibre rifle propellant, AR2210, is included in Figure 4 to strengthen the correlation. The dashed curve in Figure 4 corrects for the presence of perforations in the propellant grains by calculating the propellant mass, and subsequently the packing density, should all of the perforations be filled with propellant, using the propellant dimensions and densities in Table 1.

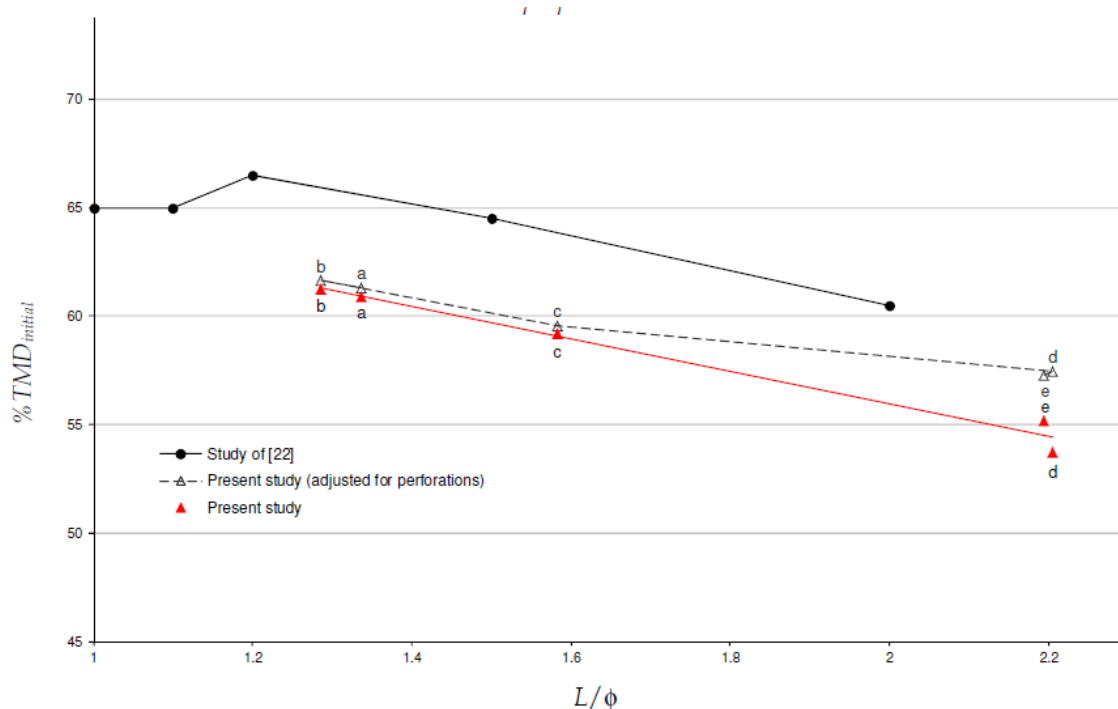


Figure 4: Initial packing density versus length-to-diameter ratio. a) AR2210; b) AR2211; c) AR2220; d) FNH-025 and e) BS-NACO.

2.2.5 Thermal Conditioning

A liquid nitrogen-cooled Instron Series 3119-405 environmental chamber was used for low temperature testing. Thermal conditioning experiments were performed using a range of single-base propellant natures (AR2205, AR2220, FNH-016, FNH-025 and BS-NACO), in order to determine suitable conditioning periods for testing at -60°C , for both the 20 mm and 50 mm dies. The experimental setup involved k -type thermocouples monitoring the temperature in the middle of three propellant beds, as well as temperature in three locations within the environmental chamber: top, middle and bottom, as shown in Figure 5 for the 50 mm diameter test assemblies. The 50 mm diameter dies were covered in aluminium foil so that any bed cooling via direct convective processes was minimised, as is the case during testing when the piston is resting on the propellant bed. Subsequent testing, however, showed that the presence of the aluminium foil had a negligible effect on the cooling rate of the propellant bed. The 20 mm die openings were closed using rubber stoppers through which the thermocouple was passed.

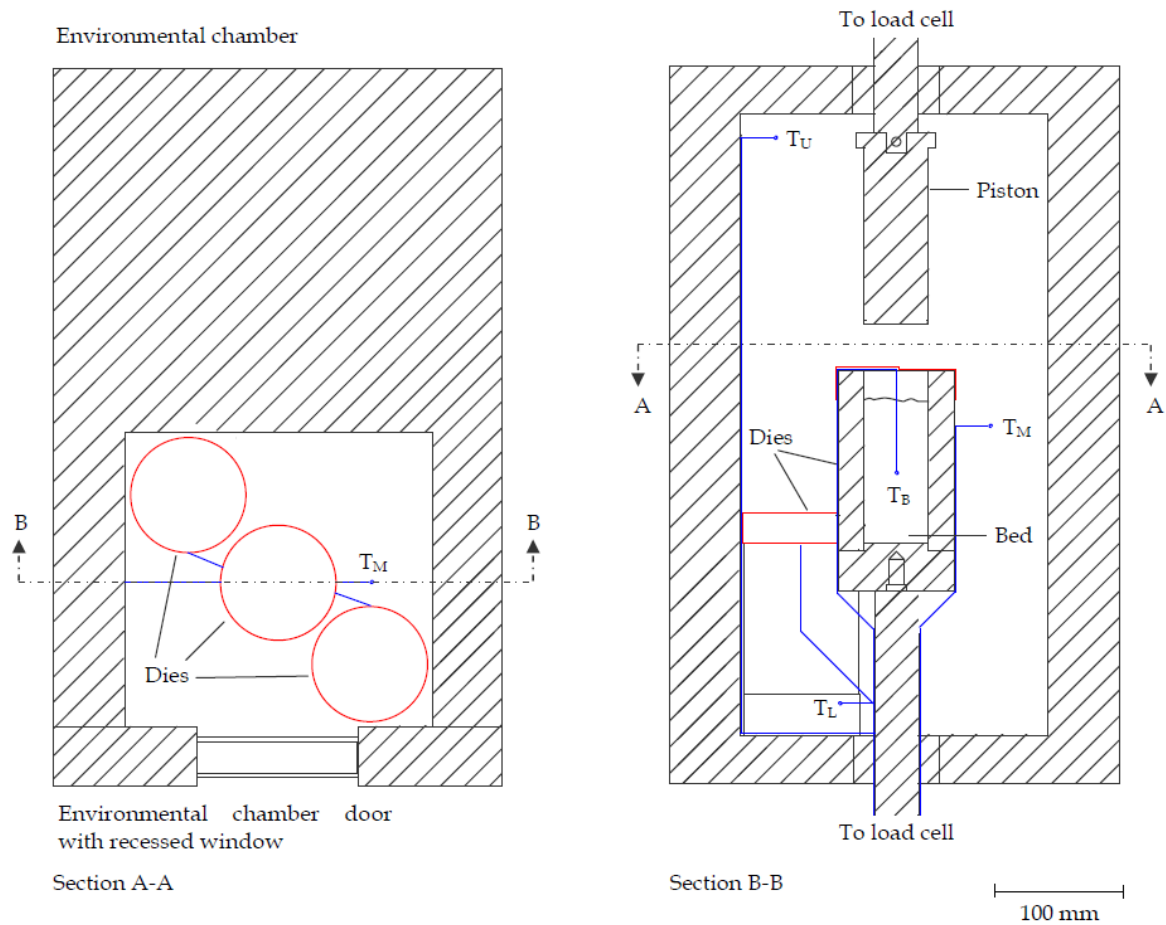


Figure 5: Schematics of the experimental setup for temperature conditioning time period determination. Red indicates aluminium foil covering, blue circles represent k-type thermocouples, blue lines represent thermocouple cable.

The temperature of -60°C at which experiments were performed was selected as it is slightly below the lower limit of terrestrial temperatures of military interest, -57°C [23], and also due to the time-temperature considerations discussed in Section 3.2. Figure 6 and Figure 7 show the results of the thermal conditioning duration determination experiment for AR2220 (20 mm die) and BS-NACO (50 mm die) respectively. The conditioning experiment for the 50 mm die assembly concluded when the liquid nitrogen supply was exhausted. It may be seen in Figure 6 that there is a temperature offset of approximately 5°C between the control temperature and actual bed and chamber temperatures, with use of a control temperature of -60°C producing bed temperatures of -65°C . Hence, for testing at -60°C bed temperature, the control was set to -55°C . Testing was also performed at -40°C , as this is the temperature specified in the Low Temperature Embrittlement Test of [24]. Testing at this nominal temperature was performed using a set point of -38°C , although insufficient thermal conditioning data exist to confirm that this set point results in an actual bed temperature of -40°C .

The 20 mm conditioning tests involved slightly less thermal mass than was used in subsequent testing, where an extra two pistons, and three clamp assemblies were routinely conditioned. In this case however, the relatively constant chamber temperature traces of Figure 6 indicate that the cooling capacity of the environmental chamber is well able to accommodate this scale of thermal mass and the addition of the extra thermal mass is not likely to significantly affect the time required for conditioning. For the 50 mm conditioning experiments, three dies were conditioned simultaneously. For testing proper, two die assemblies with a third piston were conditioned simultaneously. As such, the results presented in Figure 7 are considered conservative as they relate to the conditioning of a greater thermal mass.

The small offset between the propellant and air temperature that is observed at the beginning of the experiments depicted in Figure 6 and Figure 7 may be attributed to the propellant being stored in an adjacent room prior to testing and evidently at a lower temperature than the testing bay. As the experiments were performed with an insulating air layer immediately above the propellant bed (see Figure 5), rather than the piston as was the case during experiments, the conditioning times are conservative as, during testing, a higher cooling rate is expected due to conduction from the top propellant surface through the steel piston. Hence the initial slight offset at ambient temperatures is not thought significant given consideration of the conditioning times.

Based on the above, cold temperature conditioning times were set at a minimum of 1.5 and 2.5 hours for the 20 and 50 mm dies, respectively. For ambient testing the propellant was conditioned in the testing lab and the laboratory temperature measured, see Table 4.

Table 4: Average ambient test temperature for each propellant tested (\pm values are half the data range).

Propellant	Average Test Temperature ($^{\circ}\text{C}$)
AR2211	20.1 ± 0.2
AR2220	25.0 ± 0.2
FNH-025	26.2 ± 0.3
BS-NACO	22.8 ± 0.3

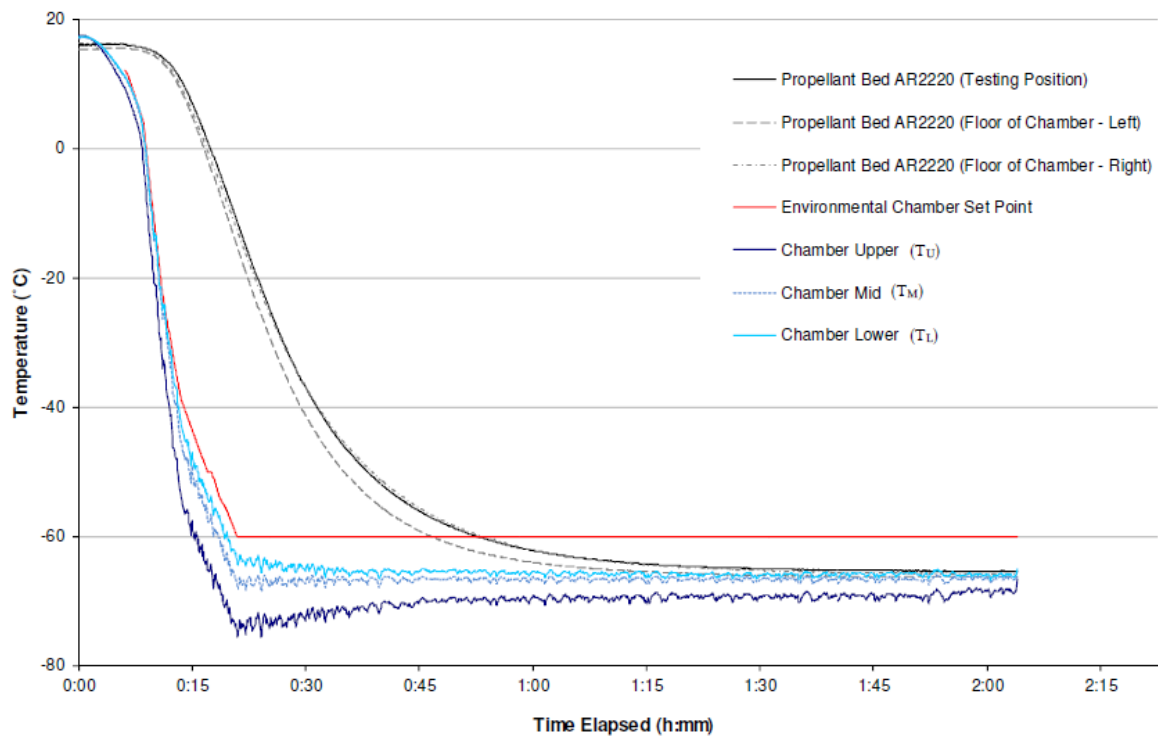


Figure 6: Thermal conditioning duration determination, 20 mm diameter assemblies, AR2220 at -60°C control temperature.

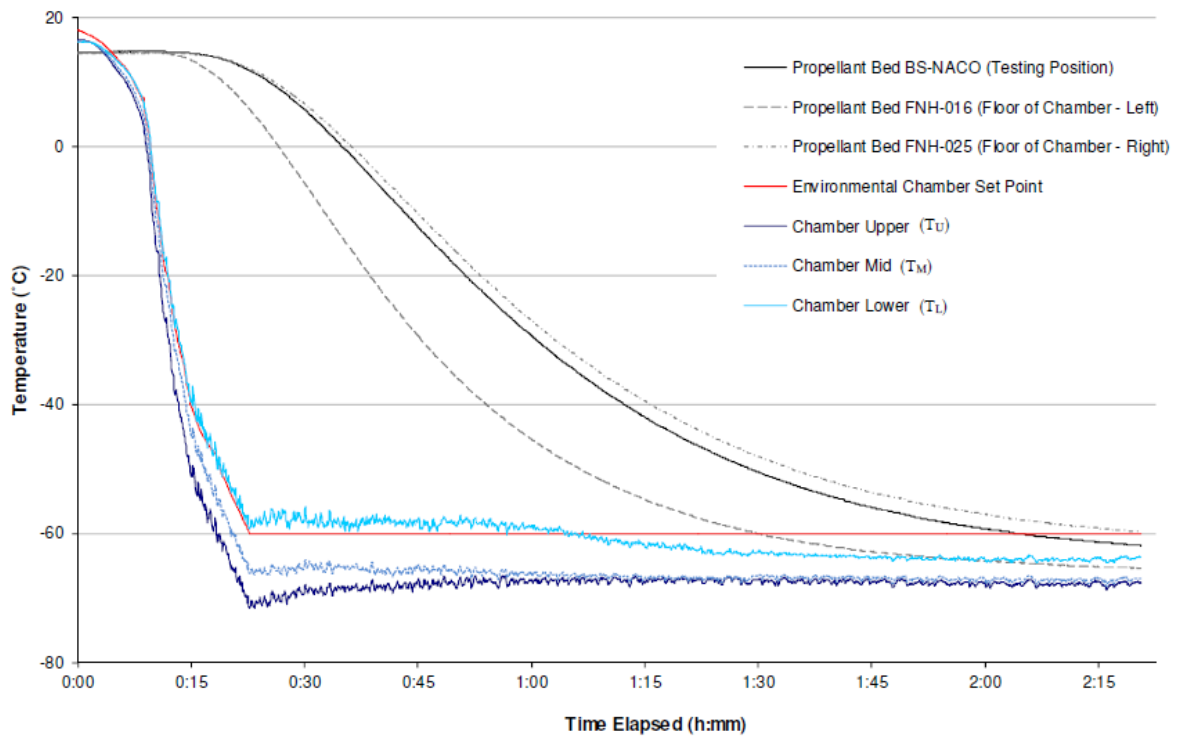


Figure 7: Thermal conditioning duration determination, 50 mm diameter assemblies, BS-NACO, FNH-016 and FNH-025 at -60°C control temperature.

A typical program for a single days testing was either: one test using a 50 mm die, followed by two tests using 20 mm dies; three tests using 20 mm dies; or two tests using 50 mm diameter dies. In the first case, the three dies were conditioned for 2.5 hours, with the 50 mm diameter test assembly in the testing position and the remaining 20 mm diameter test assemblies positioned on the floor of the environmental chamber. The sample in the 50 mm diameter die was then tested after removal of the other dies from the environmental chamber in order to minimise the net explosive quantity (NEQ) of propellant in the vicinity of the test. Following the 50 mm testing and die removal from the chamber, one of the 20 mm diameter assemblies was placed in the testing position, with the remaining die placed on the floor of the environmental chamber. Reconditioning was then undertaken for 1 hour, based on data acquired during commissioning, shown in Figure 8. This figure represents the results of a conditioning experiment involving AR2205 propellant in the three 20 mm diameter dies at the storage/testing positions in the environmental chamber. The data shown in Figure 8 is from the end of the experiment, once cooling had ceased and the door of the environmental chamber opened. This data was used to indicate the rise in temperature of a die removed from the environmental chamber and placed on the bench for a period of time, typically between 10–15 minutes. Over this period of time, the bed temperature was found to rise approximately 20°C to 30°C. Figure 9 was constructed using the complete set of AR2205 data that is partially shown in Figure 8, in an attempt to replicate the conditioning and testing of three 20 mm diameter test assemblies over the course of a day, with 20 minute sample changeover times. Although the exact nature of the transition that would occur in reality, and with different propellant types, from bed heating to cooling is difficult to model without further conditioning testing, the composite Figure 9 was thought an adequate tool for determining reconditioning durations.

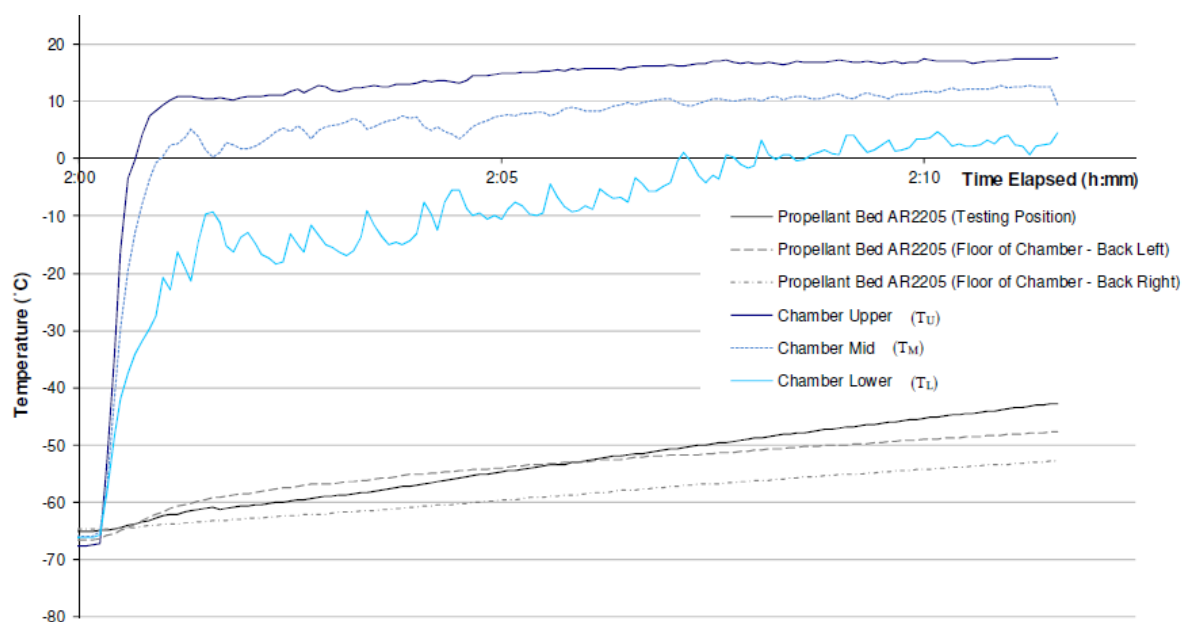


Figure 8: Thermal re-equilibration time determination, 20 mm diameter assemblies, AR2205 beginning at approximately -65°C before cooling ceased and environmental chamber door opened. No aluminium foil covering dies.

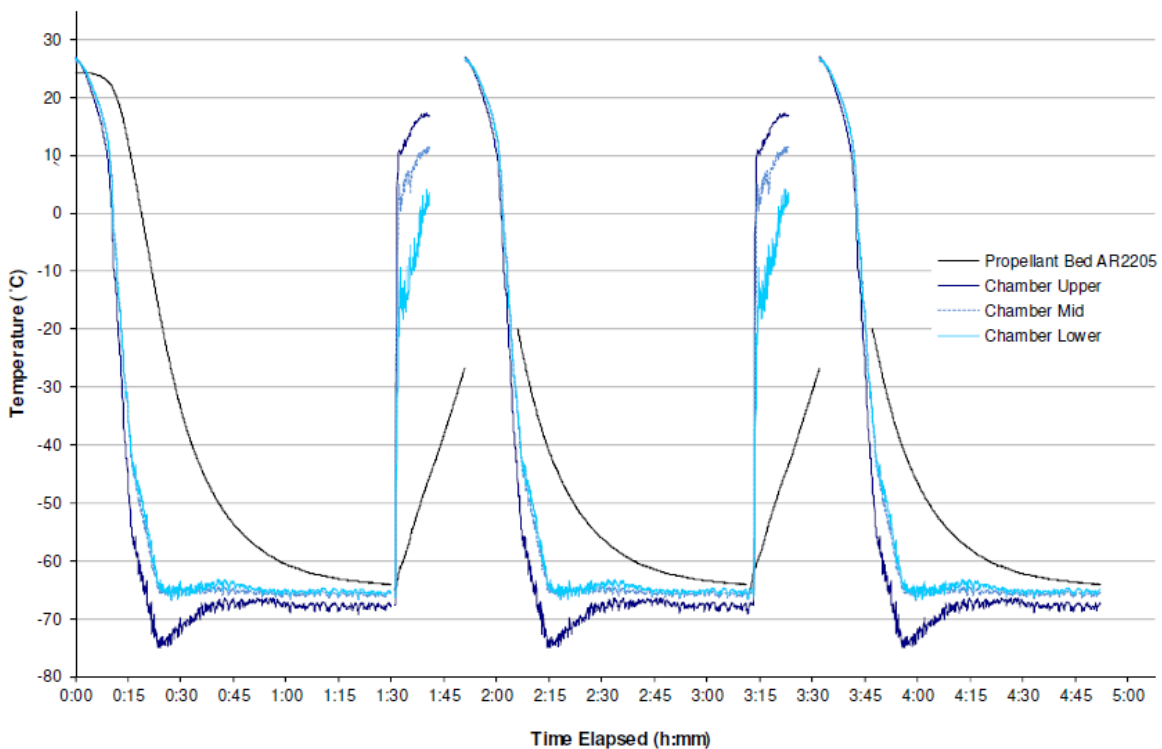


Figure 9: Approximation of the thermal history of the testing of three 20 mm diameter assemblies, all of which begin conditioning at time zero. The bed temperature is that of whichever die is to be tested next.

2.2.6 Maximum Test Load

The maximum testing load that the Instron load frame is able to deliver is 100 kN, equating to applied pressures of 318 MPa and 50 MPa for the small and large dies respectively. The Low Temperature Embrittlement Test of AOP-7 specifies applied pressures of 30 MPa [24]. Based on initial compression testing of small and large calibre propellants at -60°C , the small calibre propellants were found to sustain much lower levels of fracture compared to the large calibre propellants, see Section 3.2.2. It was found that 100 MPa and 40 MPa are suitable maximum applied pressures for testing beds of small and large calibre propellants respectively, with the higher applied pressure necessary for the small calibre propellants to achieve measurable levels of fracture to enable comparison with the fracture characteristics of other propellants.

2.2.7 Data Analysis

The data analysis methodology involves: zeroing the force and extension data to the point of initial piston-propellant bed contact; applying a correction to the piston extension, required due to axial compliance of the apparatus; applying a correction to bed radius due to radial deformation of the die wall; calculating the instantaneous propellant bed volume; and calculating the average stress applied to the propellant bed. This section details this process, with an example provided for AR2220. Likely and maximum expected error due to these operations is also discussed.

2.2.7.1 *Point of Initial Contact*

When performing a bed compression test, the bed packing method described in Section 2.2.4 is used to arrive at a die-piston-bed configuration as shown in Figure 1(A). The bed height is determined by measuring length x in Figure 1(A). This is performed using a digital micrometer and averaging the four measurements taken at equally-spaced angular positions. This assembly is then situated between the two load cells, via the upper and lower connecting rods: the lower via a threaded connection, the upper via a pin connection. The piston is raised above the propellant bed using the fine position control on the Instron control panel. Using the same fine control method the piston is brought steadily closer to the propellant bed, causing the measured load to slowly increase due to air and/or frictional resistance. The point of piston contact with the propellant bed is detected by observation of a more rapid increase in the measured load. Once the point of initial contact is determined, the piston is raised by approximately 0.15 mm, corresponding to 10 gradations of the fine position control.

Figure 10 shows the raw data for compression of AR2220 at -40°C in black, along with the associated axial compliance correction curves in red. The points of initial contact are able to be judged as the points at which the load traces deviate from their initial behaviour, indicated by vertical grey dashed lines. Initial load behaviours observed in Figure 10 include: oscillation without substantial increase (black) and steady increase (red). Based upon the load trace, two options are given for the initial point of contact with the AR2220 data: 0.36 and 0.39 mm, with the latter taken as the 'correct' value and the former chosen as a reasonable alternative for comparison. The result of correcting for the initial contact points in Figure 10 are shown in Figure 11. Following application of the data analysis procedure summarised in Section 2.2.7 above, the results shown in Figure 12 were produced. A 0.15% increase in %TMD at maximum stress (82.4% compared with 82.3%) is noted, giving an uncertainty of approximately $\pm 0.1\%$. Given that all of the data collected to date is as well-behaved as in this typical example, it can be stated that the effect of the choice of initial contact point on the results is minimal.

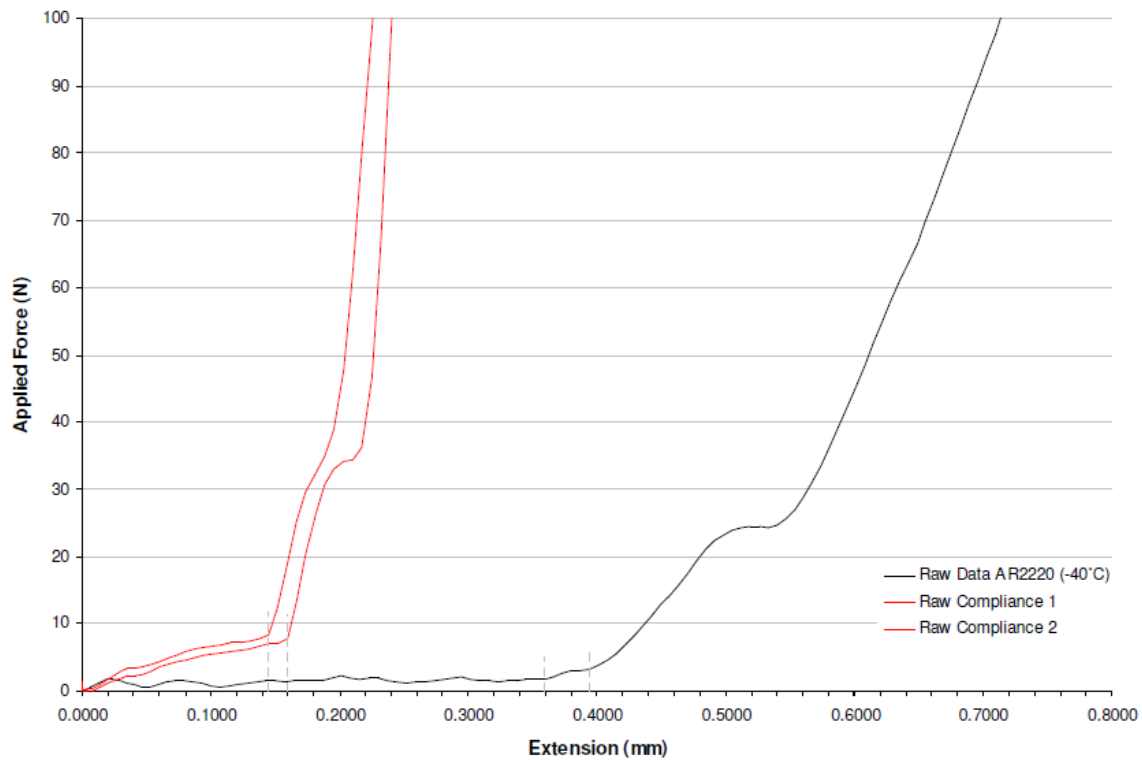


Figure 10: Raw data for AR2220 bed crushed at -40°C , with axial compliance data in red. Possible points of initial contact indicated in dashed grey.

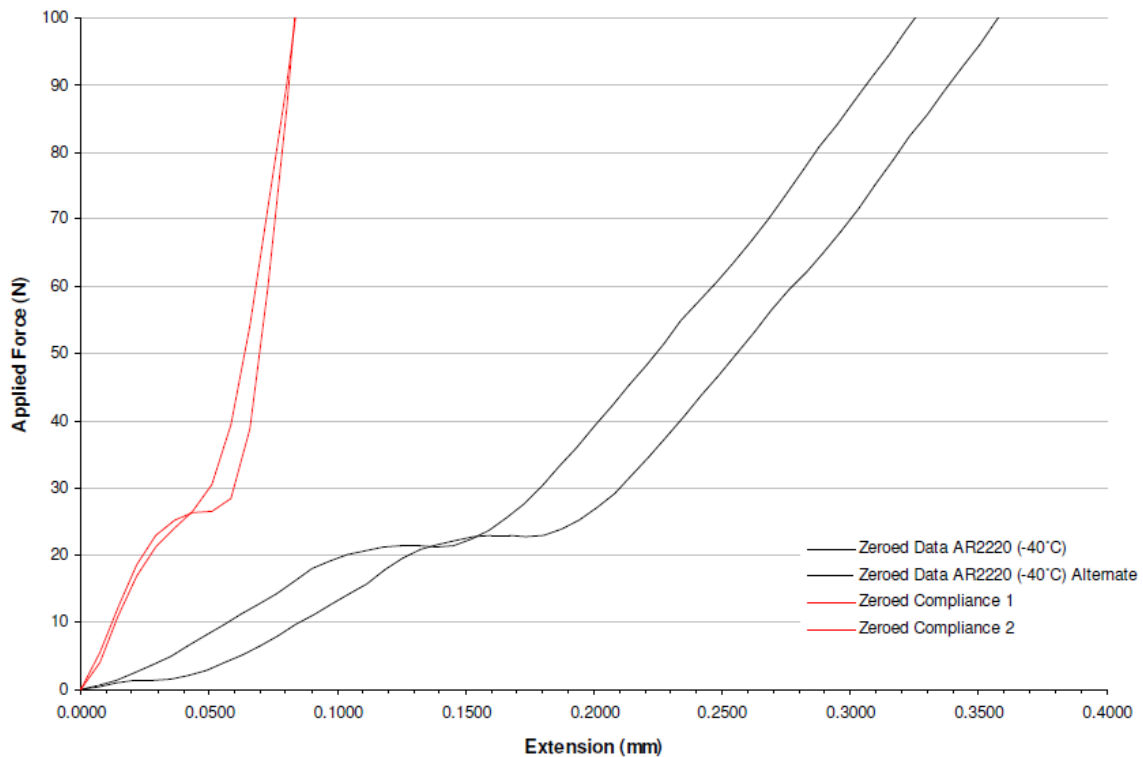


Figure 11: Data for AR2220 bed crushed at -40°C , zeroed to point of initial contact, zeroed axial compliance data shown in red.

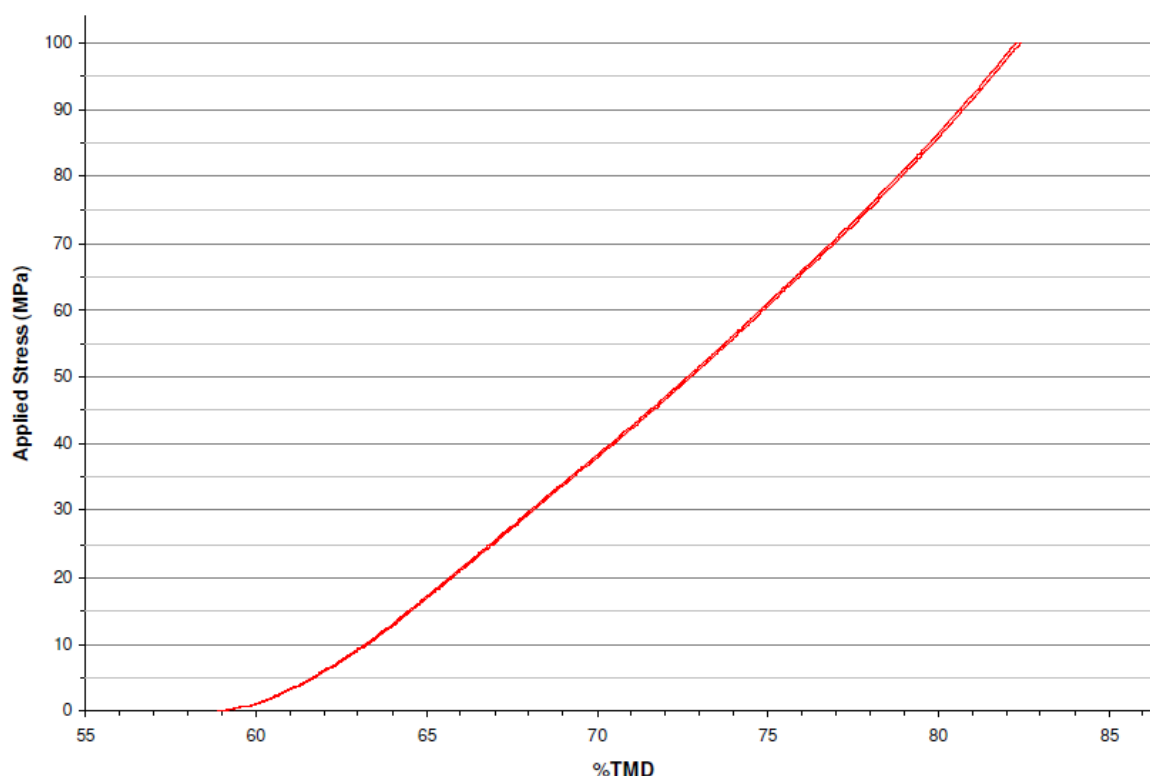


Figure 12: Effect of choice of initial contact point on resultant AR2220 stress versus %TMD curves.

2.2.7.2 Correction for Axial Compliance

Under the applied loads used in the low strain rate mechanical properties test, the assembled apparatus undergoes a level of elastic deformation that needs to be accounted for when analysing the mechanical response of the propellant. The deformation of the assembled apparatus, without propellant, was determined experimentally as a function of applied force. This was performed a minimum of five times for each die-piston configuration at the beginning of each testing campaign and, on occasion, also at the end of a campaign to confirm that the compliance measurements still held. Either two or three representative axial compliance results for a particular die were used to correct subsequent propellant testing results obtained using that die. Tests were performed at 40 mm/min and 100 mm/min for the 20 mm and 50 mm die assemblies respectively (corresponding to the typical crosshead speeds employed when testing propellant), and to 50 kN and 90 kN respectively (corresponding to applied forces greater than those employed when testing propellant). In order to simulate the assembly sequence used when testing propellants the assemblies were 'reset' between tests. This involved loosening and then re-tightening the clamp nuts, removing and then re-inserting the upper pin, and loosening and then re-tightening the lower threaded connection.

Figure 13 shows the effect of applying the axial compliance correction on the AR2220 data at -40°C. The correction algorithm produces data corrected for axial compliance by subtracting the average of the selected compliance curves from the experimental data. In

Figure 13, the red axial compliance traces were acquired immediately prior to the testing program that yielded the AR2220 result in black.

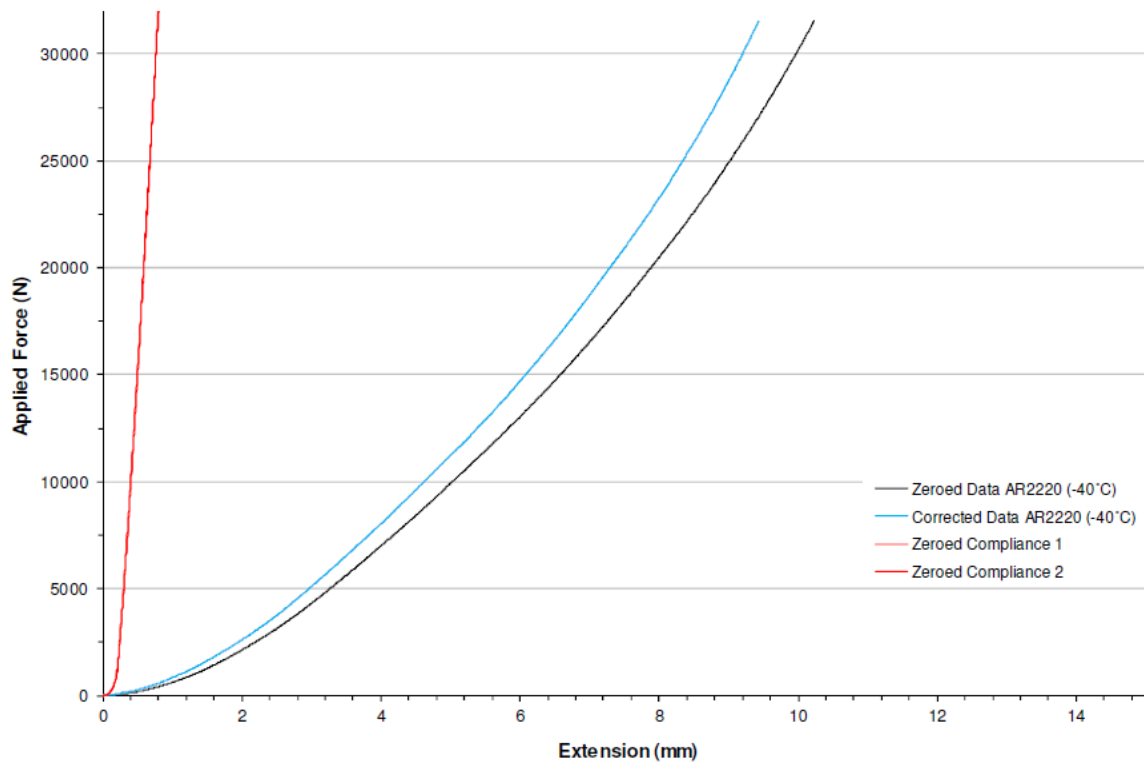


Figure 13: Data for AR2220 crushed at -40°C , corrected for axial compliance.

The uncertainty introduced when correcting for axial compliance was investigated by examining the variation in the ten axial compliance measurements taken over a four day period for one of the 50 mm assemblies and the effect that this variation had on data for FNH-025 crushed at -60°C , which was acquired using the same die during the same four day period. As per the opening paragraph of this section, five compliance measurements were taken on 06-05-13 and five on 09-05-13 to determine the axial compliance correction for this particular 50 mm assembly, shown in Figure 14 and Figure 15. Four tests were performed using the assembly, on the 07, 08, 09 and 10-05-13, all of them corrected using a single compliance curve, indicated on Figure 16. This compliance curve was used for correction as it was one of the curves grouped in a relatively narrow band. Such a distribution of compliance curves was typical across the assemblies, and may be attributed largely to the characteristics of the pin connection between the piston and upper rod. With use, it is thought that the pins became fractionally bent, leading to a situation in which different 'tightnesses' were possible depending on the rotational position of the pin. This is the main reason that compliance measurements were performed prior to a testing campaign, to capture the compliance behaviour using the current state of the pins. Figure 17 shows the analysis results for the FNH-025 data, corrected using the selected compliance data as well as the maximum and minimum outlying traces. Here the outlying compliance curves as indicated in Figure 16 give a difference in %TMD at maximum stress of 0.16% of actual %TMD at maximum stress (68.33 and 68.44% compared with 68.35%). If

the uncertainty due to both determination of the point of initial contact and correction for axial compliance are added together, the result is approximately $\pm 0.15\%$. This uncertainty only applies when the distribution measurements are taken regularly and the initial contact point determination is able to be accurately made.

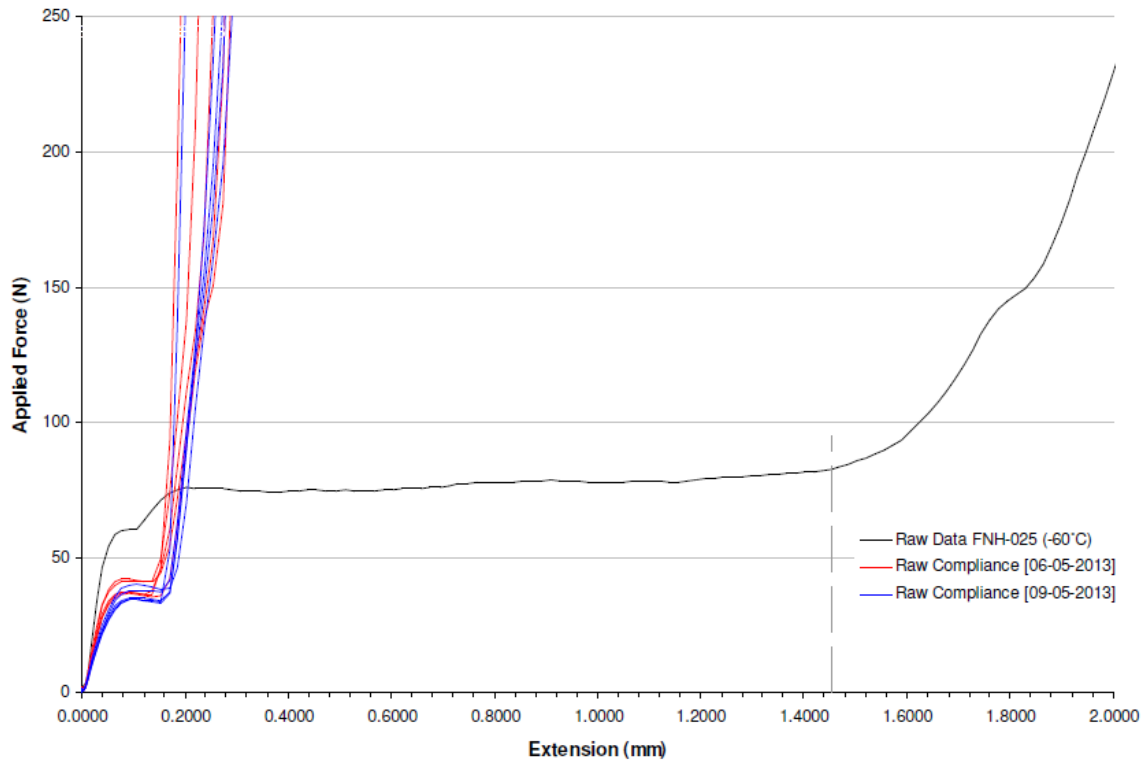


Figure 14: Raw data for FNH-025 crushed at -60°C, along with axial compliance curves.

To investigate the effect that temperature has on axial compliance, five compliance tests were performed using one of the 20 mm assemblies: two tests at ambient followed by three tests at -60°C. For the -60°C testing an initial 1.5 hr conditioning time was applied followed by a 1 hr reconditioning time after each test. A portion of the results is shown in Figure 18.

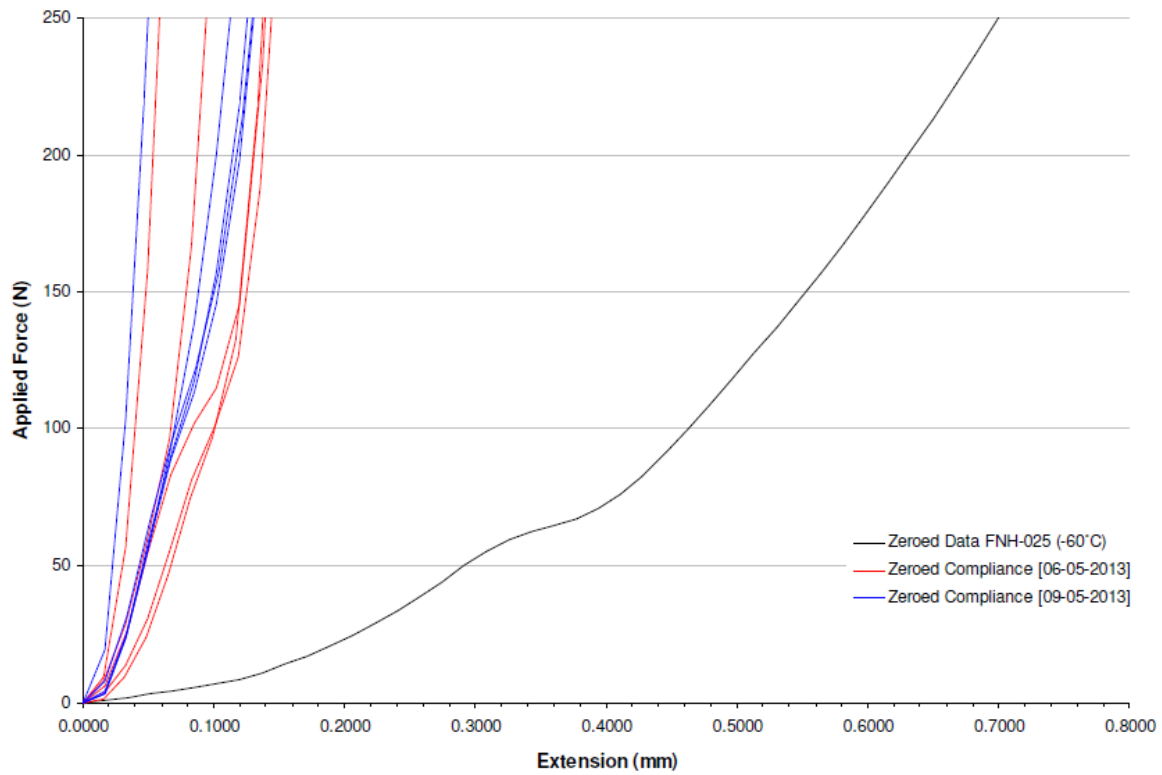


Figure 15: Zeroed data for FNH-025 crushed at -60°C , along with axial compliance curves.

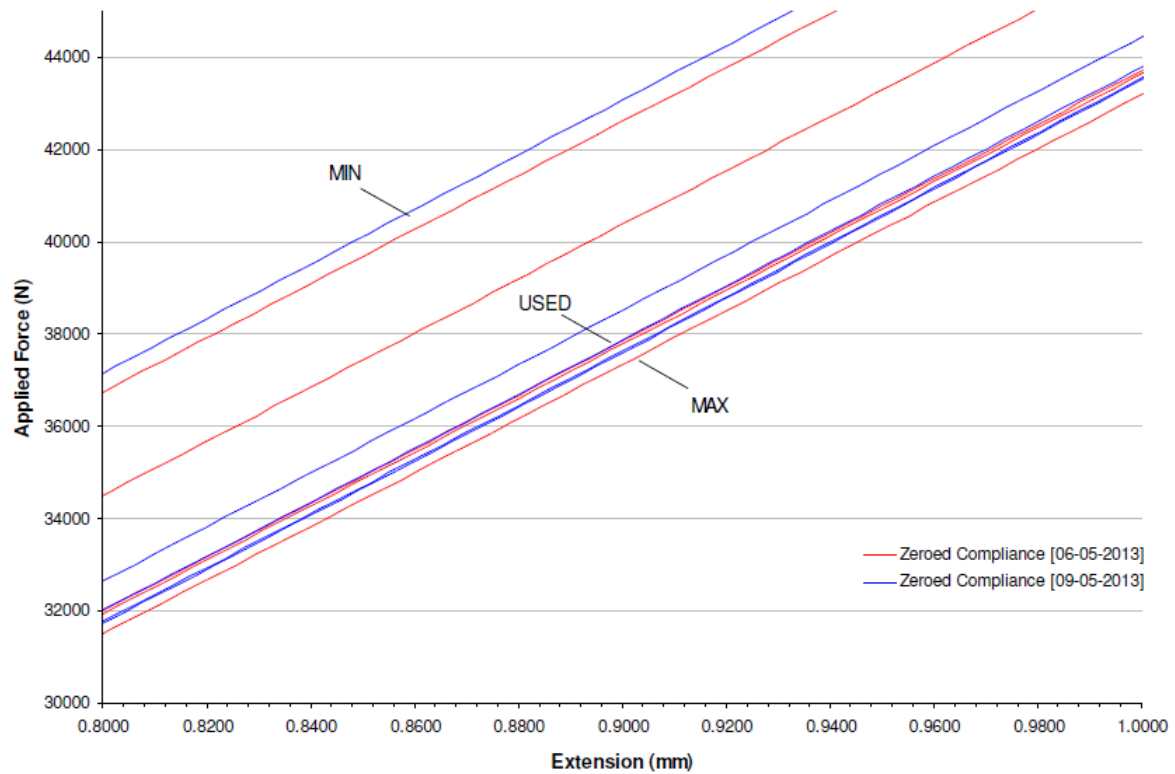


Figure 16: Axial compliance curves, ten over a four day period.

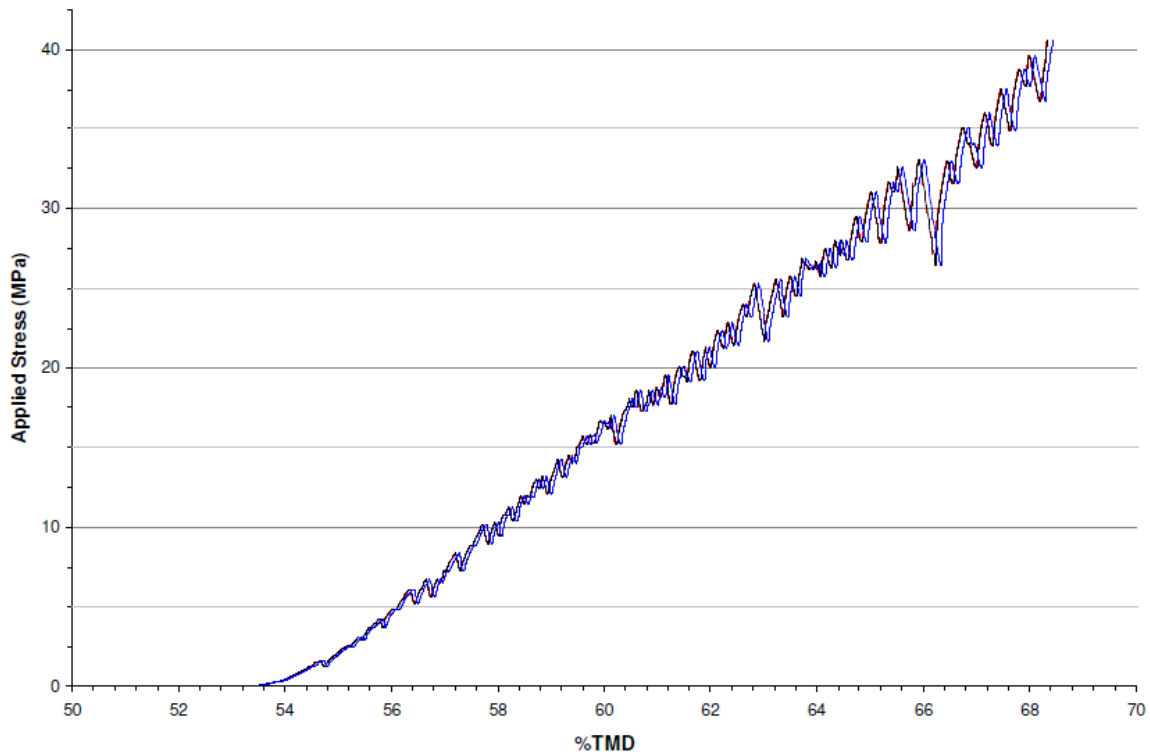


Figure 17: Uncertainty due to axial compliance correction, FNH-025 crushed at -60°C.

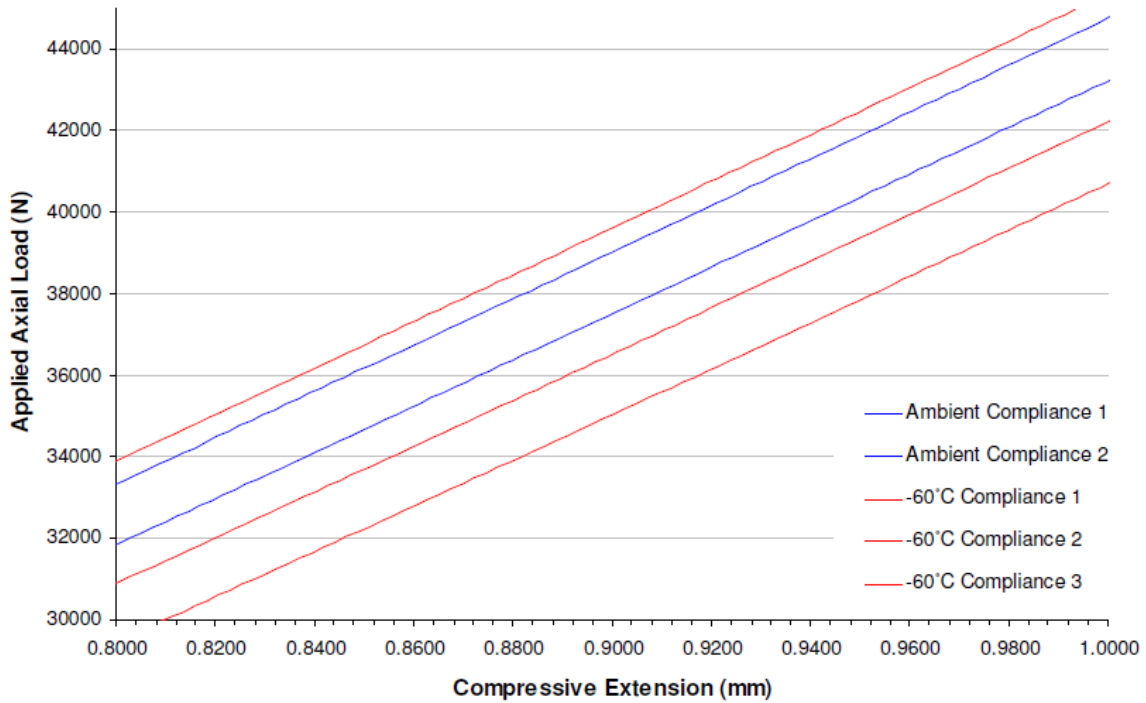


Figure 18: Effect of temperature on axial compliance, 20 mm assembly.

It may be seen that the spread in compliance traces is no greater than in the ambient traces shown in Figure 16. Table 5 confirms that the difference in compliance values, given by the slope of the curves in Figure 18, is negligible across the temperature range tested. This enables the use of compliance measurements taken at ambient to be used when analysing results obtained using the 20 mm assemblies at temperatures as low as -60°C. An analogous result was assumed for the 50 mm assemblies.

Table 5: Effect of temperature on axial compliance, 20 mm assembly

	Axial compliance over the range 10 - 50kN (mm/N)
Ambient Compliance 1	1.810
Ambient Compliance 2	1.810
-60°C Compliance 1	1.798
-60°C Compliance 2	1.817
-60°C Compliance 3	1.833

2.2.7.3 Correction for Radial Compliance

For this work, radial deformation experienced by the die walls as a function of internal bed pressure was theoretically determined using the Lamés Equations that give stresses as a function of radial position, r [25] [26]:

$$\text{Radial stress: } \sigma_r = [(p_i.r_i^2 - p_o.r_o^2)/(r_o^2 - r_i^2)] - [r_i^2.r_o^2.(p_o - p_i)/r^2.(r_o^2 - r_i^2)] \quad (1)$$

$$\text{Hoop stress: } \sigma_h = [(p_i.r_i^2 - p_o.r_o^2)/(r_o^2 - r_i^2)] + [r_i^2.r_o^2.(p_o - p_i)/r^2.(r_o^2 - r_i^2)] \quad (2)$$

In these equations, p_o is pressure outside of the die (taken to be nominal atmospheric pressure), p_i is the internal pressure (assumed to be the average axial stress experienced by the propellant bed, calculated assuming a rigid die wall), r_o is the outer die radius, and r_i is the inner die radius. The radial and hoop stresses were evaluated at the inner die radius, to give inner-wall die stresses. Using Poisson's Ratio (ν) and Young's Modulus (E) for AISI D2 Tool Steel, and assuming zero axial die wall stress, σ_1^1 , the change in radius can be calculated using a generalised form of Hooke's Law for isotropic materials:

$$\Delta r = r.(\sigma_r - \nu.\sigma_h - \nu.\sigma_1)/E \quad (3)$$

Of those prior researchers who corrected for radial compliance, Sandusky and Elban [2] used formulas found in Roark and Young [27] and quoted their maximum radial die expansion to be 0.2 mm. Equations (1), (2) and (3) give close agreement with 0.2 mm for the increase in internal die diameter when modelling their die dimensions and maximum loads. For this study, the calculated radial die expansion was accounted for when determining the applied stress, however the correction was found to have a negligible effect on the result.

¹ Although the compression causes the propellant to exert a frictional force on the wall, it is small in comparison with the applied force.

2.3 Damage Induced Surface Area Evaluation

To gauge the level of fracture resulting from the propellant bed compression, closed vessel testing accompanied by the data reduction methodology proposed by Stein and Jahnk [28] was used. The small calibre propellants were burned in a 54.7 cm³ closed vessel (a 200 cm³ vessel with a modified firing head to reduce the vessel volume) and the large calibre propellants in a 700 cm³ vessel. Propellant loading densities of approximately 0.2 g/cm³ were used for both vessels. SR317C was used as the igniter material, with the igniter mass scaled depending on the closed vessel volume: 0.25 g was used for the small calibre natures and 1.00 g for the large calibre natures, besides FNH-025 tested at -40°C, for which 3.50 g igniters were used. Testing was performed at 21°C.

Vivacity is defined in equation (4) [29,30], with $p(t)$ and P_{max} the instantaneous and maximum pressure respectively, both obtained directly from experimental data.

$$V(t) = \frac{dp(t)/dt}{p(t) \cdot P_{max}} \quad (4)$$

As both the change in vivacity and surface area are measures of progressivity (given burn rate exponents of between 0.7 and 1 [31]), plots of either parameter with fraction burned (calculated as instantaneous pressure divided by peak pressure) should ideally resemble each other, the only difference being a scaling factor [30]. For this reason, relative increases in surface area between uncrushed and crushed propellant samples may, in theory, be derived by taking the ratio of initial crushed vivacity to initial uncrushed vivacity. This is the basis of the relative surface area estimation method proposed by Stein and Jahnk [28] and subsequently specified for use in qualification of propellant in AOP-7 [24]. Using this method, the relative vivacity is plotted from 0.2 to 0.7 fraction burned and the method of least squares used to fit a linear curve to the data. Extrapolation to the ordinate axis then gives the relative increase in surface area. The range in fraction burned over which the analysis is applied is restricted to between 0.2 and 0.7 due to the influence of heterogeneous ignition in the early phases of propellant combustion, and the potential influence of grain slivering in the final stages. These phenomena are discussed at more length in Section 3.3.1. Figure 19 shows an example of this data reduction methodology for FNH-025 and gives measures of Damage Induced Surface Area (DISA) of -9%, -5% and +2% after testing at ambient, -40°C and -60°C respectively. Decreases in initial propellant surface area following crushing at the higher test temperatures indicates that the crushing has involved some plastic deformation, which reduces the initial grain surface area via perforation closure.

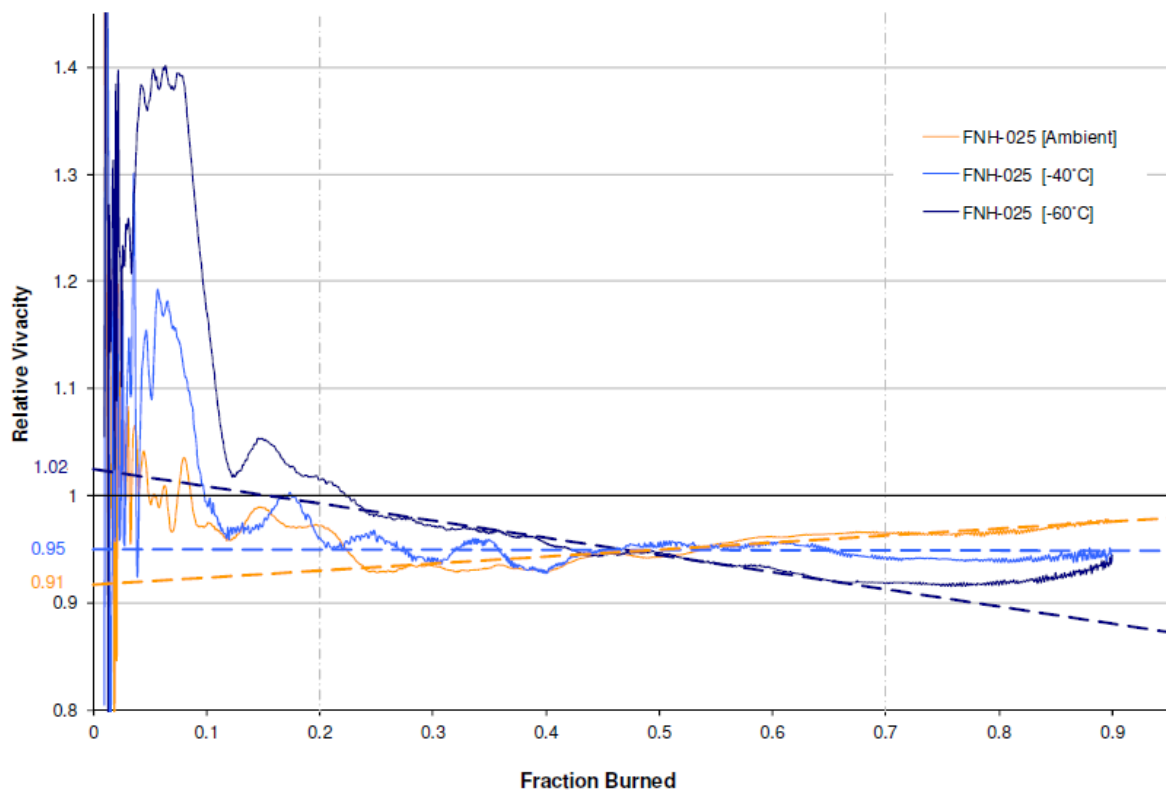


Figure 19: FNH-025 vivacity relative to uncrushed sample versus fraction burned, testing temperatures of -60°C , -40°C and ambient. The extrapolated lines of best fit of the data taken between 0.2 to 0.7 fraction burned are included in bold for the three test temperatures.

3. Results and Discussion

3.1 Repeatability of Applied Stress versus %TMD

The repeatability of results was assessed by running multiple tests on the propellants of interest, focussing on AR2220 and FNH-025. AR2220 was chosen as it is the largest grain to be tested using the 20 mm diameter assembly. For the 50 mm die assembly, FNH-025 was used as a substitute for BS-NACO owing to previously identified mechanical variability in the latter [32]. This mechanical variability is attributed to the use of the more readily gelatinised Grade E nitrocellulose in the BS-NACO propellant which leads to increased variation in grain dimensions and surface defects during manufacture. Figure 20 shows applied stress versus %TMD results for AR2220 at three testing temperatures. All data are plotted with the extent of compaction expressed as a percentage of TMD at ambient conditions. The coloured traces represent tests using beds with initial packing densities within $\pm 0.5\%$ of the $\%TMD_{initial}$ values reported in Table 3 (Section 2.2.4). Results of tests not satisfying this condition correspond to early testing when the bed packing methodologies were still being refined. These results are plotted in grey and are excluded from the compiled version shown in Figure 21. The improved consistency with the initial

bed packing density achieved through the use of the optimised bed packing method is most apparent with the FNH-025 propellant tested at ambient, see Figure 22. In all cases the results are independent of which of the three die-piston configurations were used.

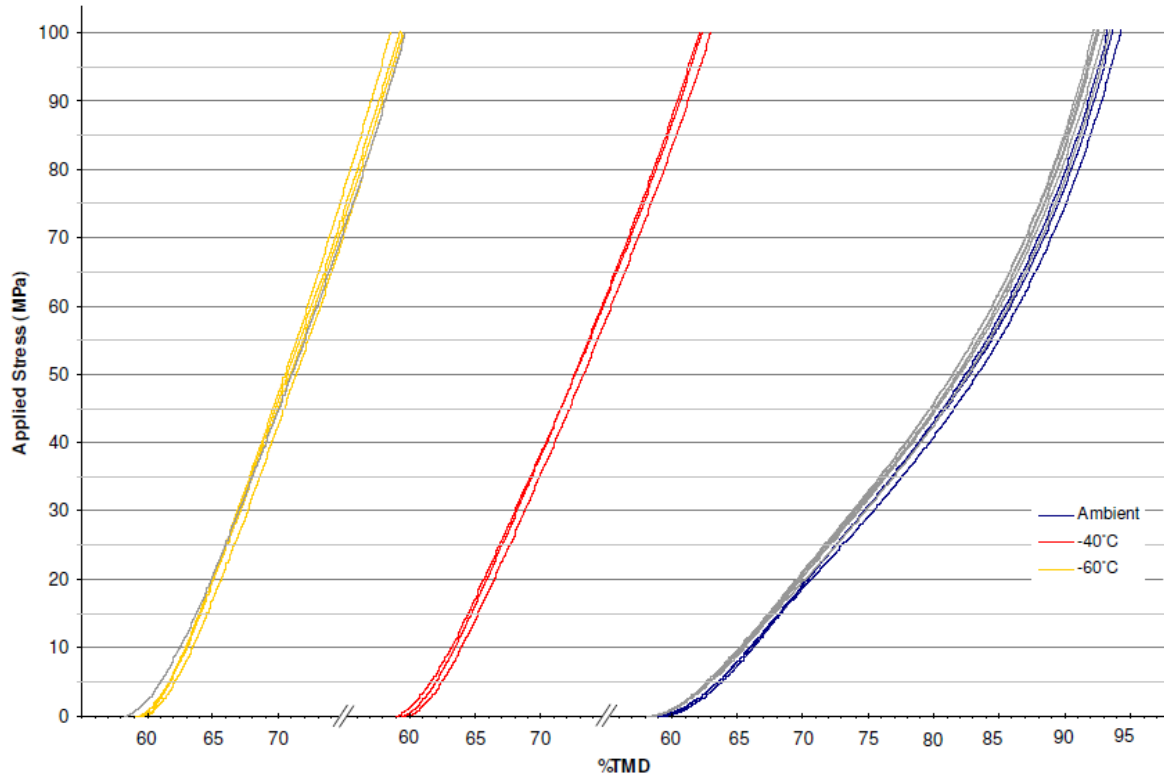


Figure 20: AR2220 stress-%TMD for ambient, -40°C and -60°C testing temperatures. Coloured traces represent results within ± 0.5 initial %TMD; other results shown in grey.

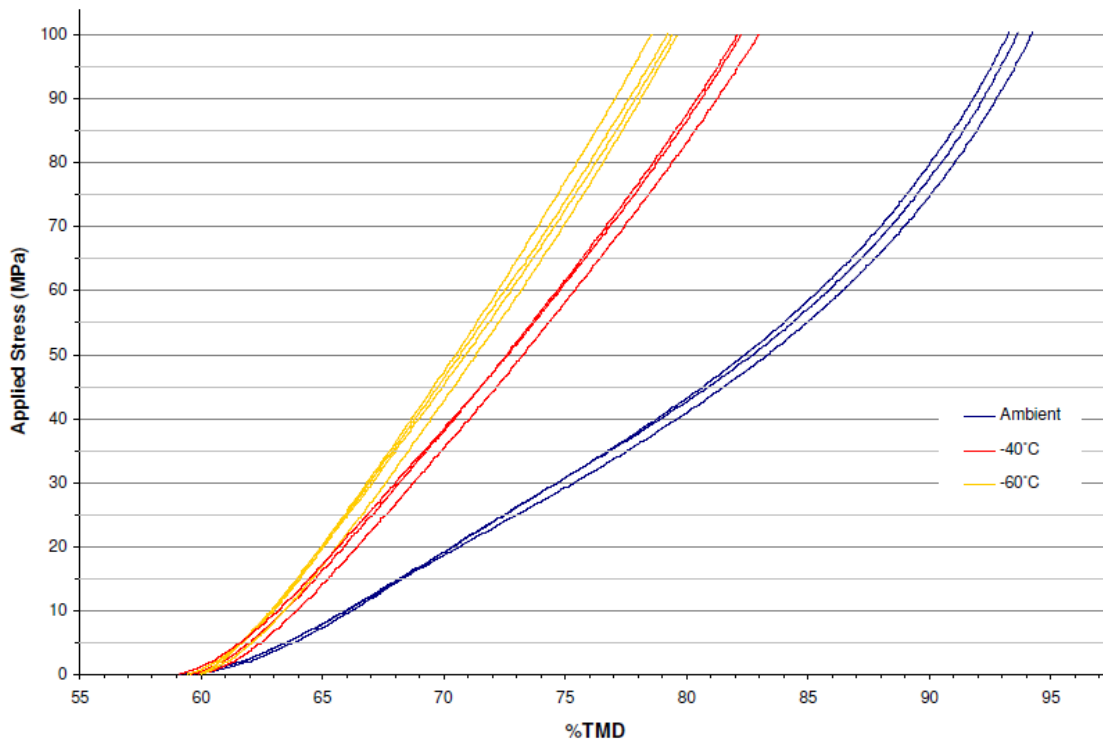


Figure 21: AR2220 stress-%TMD results at ambient, -40°C and -60°C testing temperatures. Only results within ± 0.5 initial %TMD plotted.

As discussed in Section 2.2.2, repeatability should increase with increasing ratio of die diameter to maximum grain dimension until a plateau is reached at the point where the ratio of die dimensions to the largest grain dimension is such that representative, reproducible packing characteristics are achieved. Given the similarity in formulation between the small calibre natures tested, propellant grain form will be a key determinant of any differences in mechanical property response (see also Section 3.2.1). Given that AR2220 has the largest dimensions of the small calibre propellants, and should in theory give the least repeatable results, the agreement shown in Figure 21 in terms of the shape of the curves and %TMD at maximum stress (values provided in Table 6), gives confidence that the die dimensions are suitable. Results are shown in Figure 22 and Figure 23 for FNH-025, Figure 24 and Figure 25 for AR2211 and Figure 26 and Figure 27 for BS-NACO.

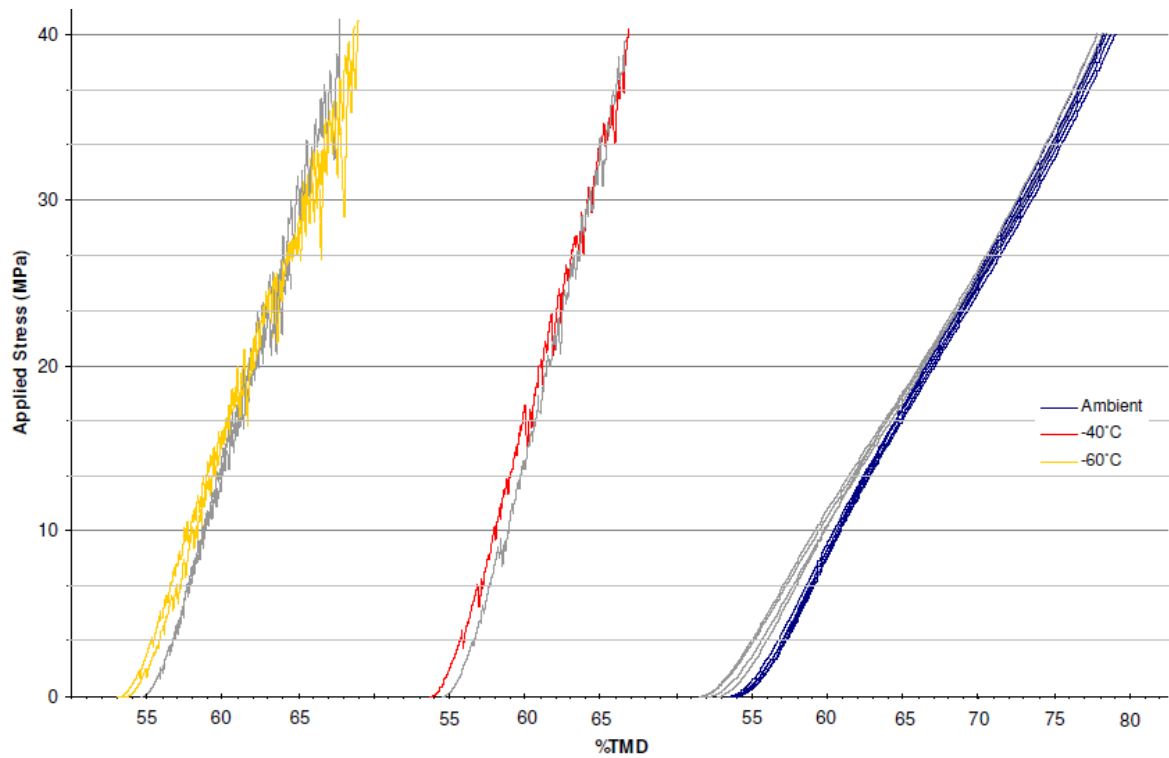


Figure 22: FNH-025 stress-%TMD for ambient, -40°C and -60°C testing temperatures. Coloured traces represent results within ± 0.5 initial %TMD; other results shown in grey.

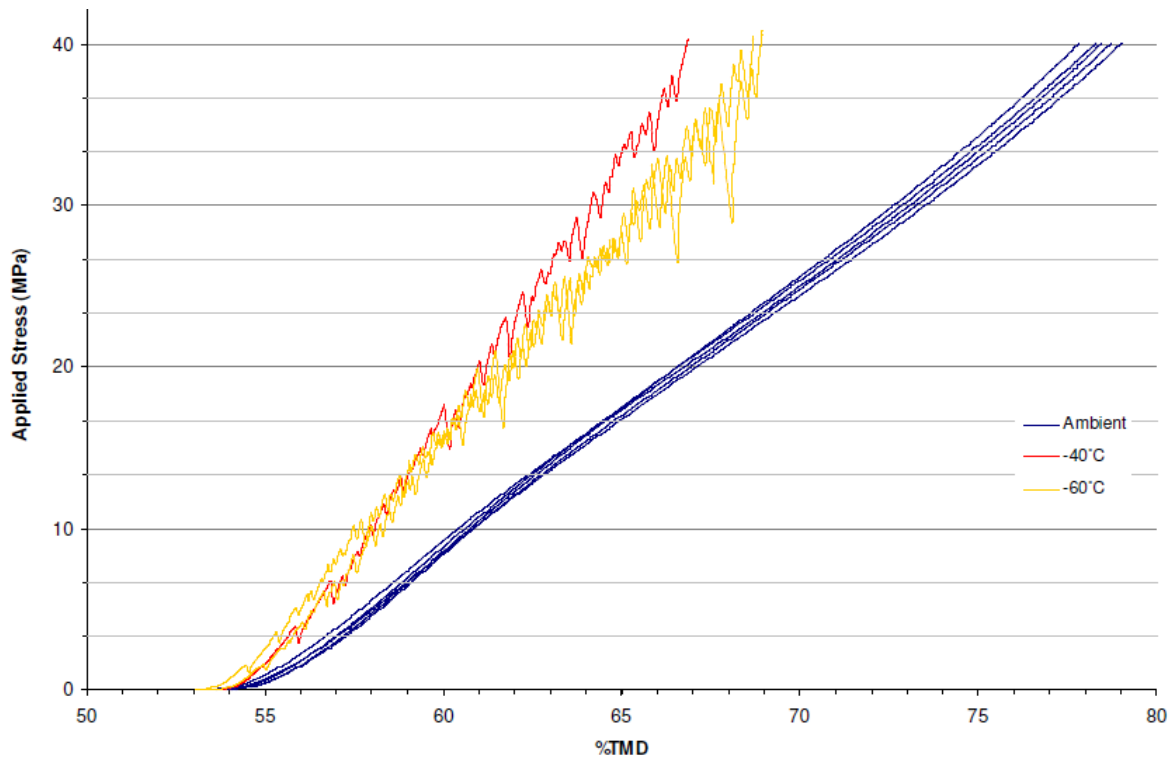


Figure 23: FNH-025 stress-%TMD results at ambient, -40°C and -60°C testing temperatures. Only results within ± 0.5 initial %TMD plotted.

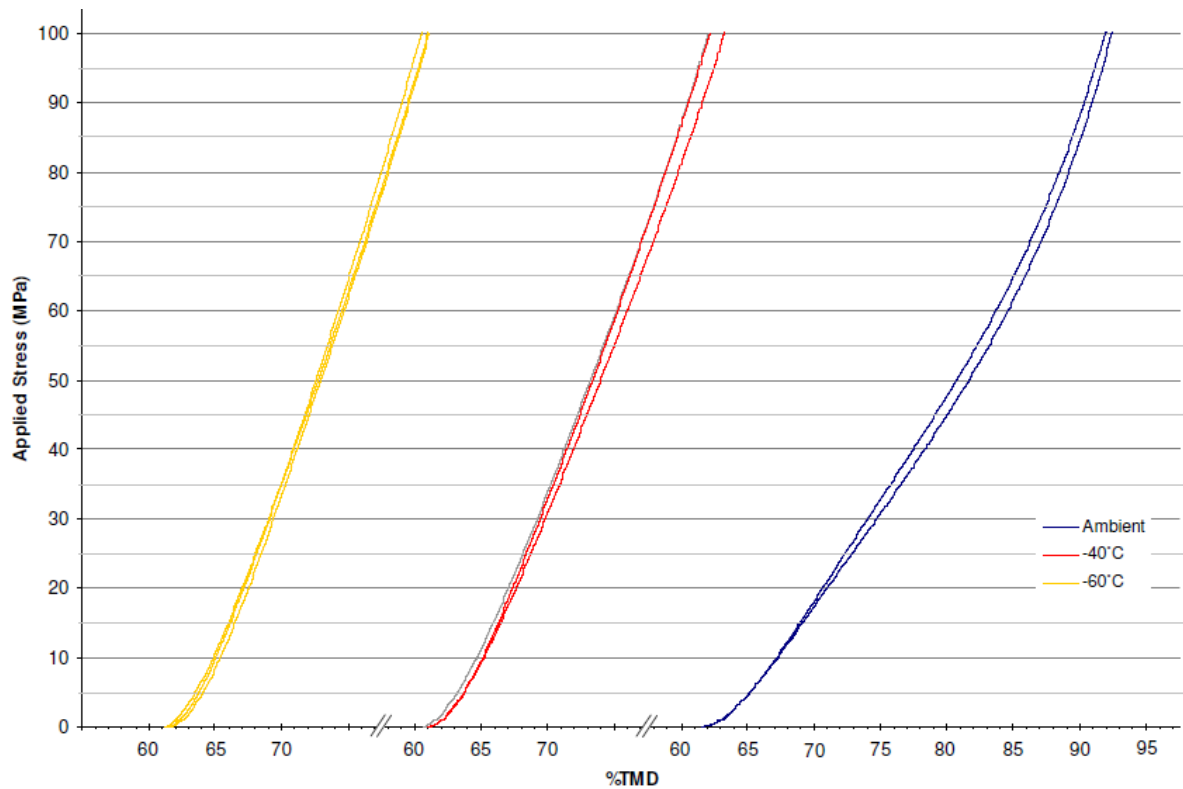


Figure 24: AR2211 stress-%TMD for ambient, -40°C and -60°C testing temperatures. Coloured traces represent results within ± 0.5 initial %TMD; other results shown in grey.

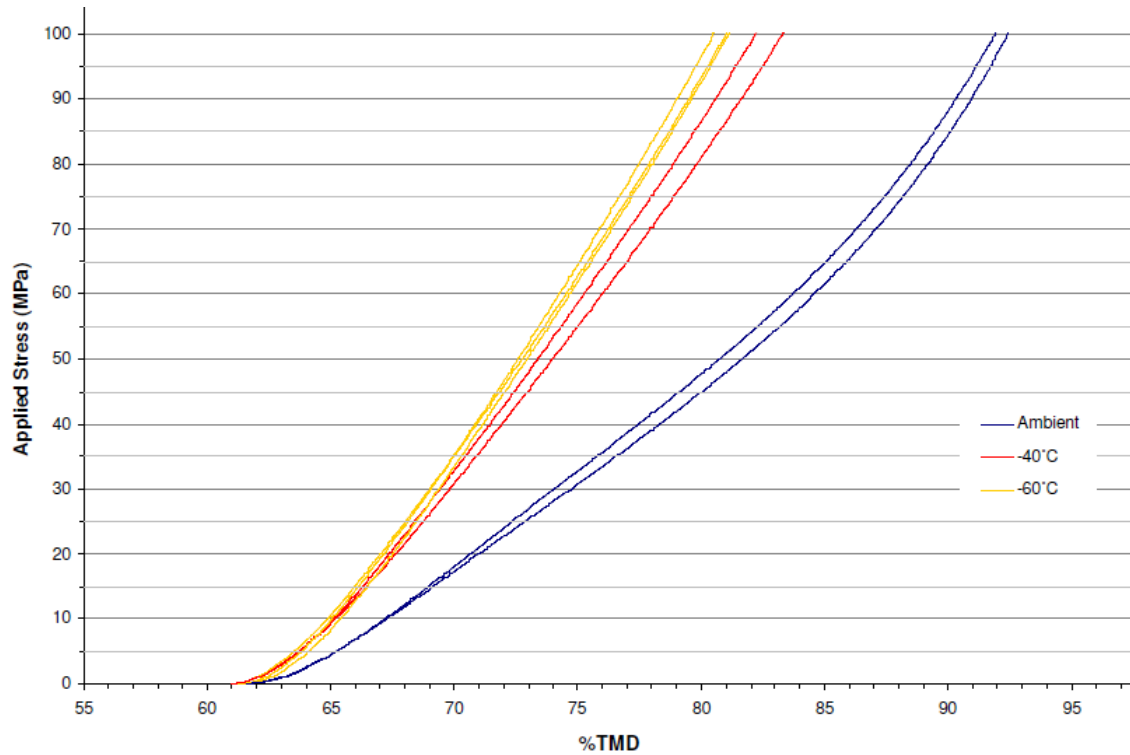


Figure 25: AR2211 stress-%TMD results at ambient, -40°C and -60°C testing temperatures. Only results within ± 0.5 initial %TMD plotted.

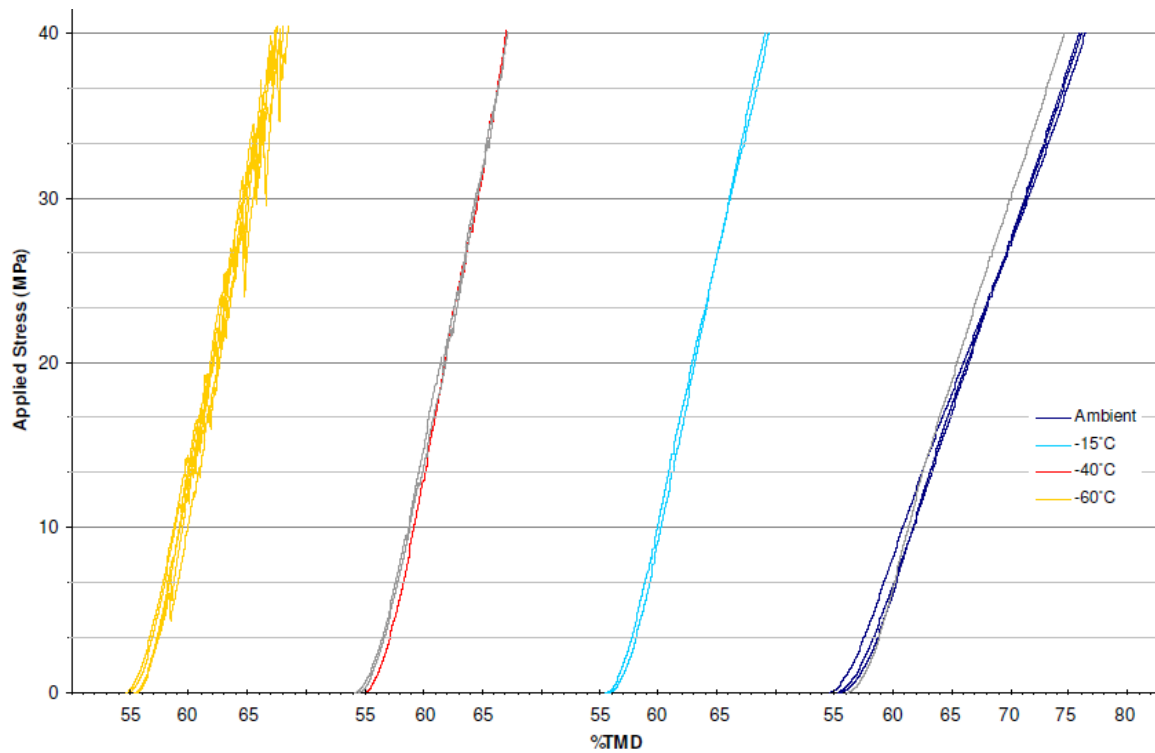


Figure 26: BS-NACO stress-%TMD for ambient, -40°C and -60°C testing temperatures. Coloured traces represent results within ± 0.5 initial %TMD; other results shown in grey.

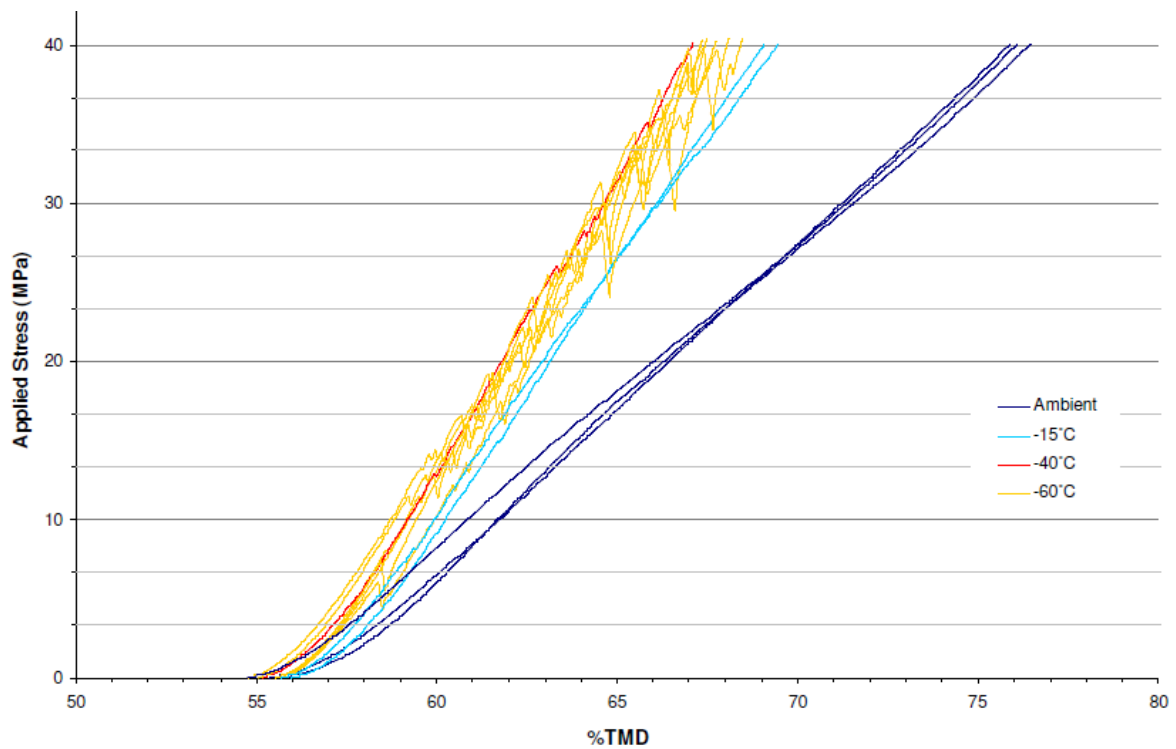


Figure 27: BS-NACO stress-%TMD results at ambient, -40°C and -60°C testing temperatures. Only results within ± 0.5 initial %TMD plotted.

Table 6 summarises the average initial and final packing densities for each propellant, at each test temperature. The values in brackets are derived using only data from tests having initial packing densities within ± 0.5 %TMD.

Table 6: Average initial and final %TMDs for each propellant and testing temperature. In the table, \bar{x} = mean, σ = standard deviation, N = number of samples. Values in brackets represent results acquired with starting packing densities within ± 0.5 initial %TMD.

Propellant		Initial %TMD			Final %TMD		
		\bar{x}	σ	N	\bar{x}	σ	N
AR2211	Cumulative	61.2 (61.3)	0.4 (0.3)	8 (7)			
	Ambient	61.6 (61.6)	0.0 (0.0)	2 (2)	92.2 (92.2)	0.3 (0.3)	2 (2)
	-40°C	60.9 (61.0)	0.2 (0.0)	3 (2)	82.6 (82.8)	0.7 (0.8)	3 (2)
	-60°C	61.4 (61.4)	0.2 (0.2)	3 (3)	80.9 (80.9)	0.3 (0.3)	3 (3)
AR2220	Cumulative	58.9 (59.3)	0.6 (0.3)	18 (10)			
	Ambient	58.6 (59.1)	0.4 (0.2)	10 (3)	93.0 (93.8)	0.6 (0.5)	10 (3)
	-40°C	59.3 (59.3)	0.3 (0.3)	3 (3)	82.5 (82.5)	0.5 (0.5)	3 (3)
	-60°C	59.3 (59.5)	0.6 (0.3)	5 (4)	79.3 (79.2)	0.4 (0.5)	5 (4)
FNH-025	Cumulative	53.4 (53.6)	1.0 (0.3)	15 (8)			
	Ambient	52.9 (53.7)	1.0 (0.2)	9 (5)	78.4 (78.5)	0.4 (0.4)	9 (5)
	-40°C	54.1 (53.7)	0.5 (-)	2 (1)	66.8 (66.9)	0.2 (-)	2 (1)
	-60°C	53.9 (53.2)	0.8 (0.3)	4 (2)	67.5 (68.8)	2.0 (0.2)	4 (2)
BS-NACO	Cumulative	55.1 (55.2)	0.5 (0.4)	15 (12)			
	Ambient	55.4 (55.1)	0.6 (0.5)	4 (3)	75.8 (76.1)	0.8 (0.3)	4 (3)
	-15°C	55.5 (55.5)	0.1 (0.1)	2 (2)	69.3 (69.3)	0.3 (0.3)	2 (2)
	-40°C	54.5 (55.0)	0.4 (-)	3 (1)	67.2 (67.1)	0.1 (-)	3 (1)
	-60°C	55.1 (55.1)	0.3 (0.3)	6 (6)	67.7 (67.7)	0.5 (0.5)	6 (6)

In the ambient BS-NACO results shown in Figure 26, some divergence may be seen in the grey trace and the two navy blue traces which have similar initial %TMDs. This is reflected in a relatively high standard deviation in final %TMD of 0.9 (not shown in Table 6) when these three ambient BS-NACO data are considered. However, inspection of the results for AR2211, which best meets the bed design heuristics of Table 2, at -40°C in Figure 24 shows

a similar degree of divergence in %TMD at final stress (standard deviation of 0.8 based on two results, see Table 6) despite similar initial %TMD. This indicates that such divergence occurs for reasons that cannot solely be attributed to die dimension heuristics. The BS-NACO results however exhibit divergence not only in %TMD at final stress but also in the shape of the ambient compression curves at low stress. The data suggests that the 50 mm assemblies produce repeatable results for BS-NACO at cold temperatures, however when testing at ambient temperatures, results are less repeatable. This is due to the bed being composed of a relatively small number of grains of relatively high aspect ratio, and hence the most likely of all the propellants tested to adopt a bed configuration that exhibits greater variability in mechanical response. This is attributed to the alignment of long chain molecules in the propellant parallel to the extrusion axis that confers greater propellant strength when the propellant is loaded in the axial, as opposed to perpendicular, direction to the grain axis. If it is further accepted that this anisotropy in grain strength decreases as the temperature is lowered and grains become more brittle, the lower repeatability of the ambient BS-NACO results at ambient temperature may be explained.

3.2 Choice of Test Temperature

Due to the dynamic forces created with ignition in the gun, propellant structural integrity across its operational temperature range is a key attribute in ensuring safe and consistent performance. A test temperature that provides realistic equivalent strain rates (see Section 3.2.3) and hence brittle material response is required, as this will enable meaningful conclusions to be drawn as to propellant mechanical integrity. The following sections examine the data acquired at the -40°C and -60°C test conditions to identify the modes of material behaviour and the most appropriate test temperature.

3.2.1 Applied Stress versus %TMD Discussion

Along with the applied stress versus %TMD already presented (Section 3.1), the parameters bulk modulus (K_b) and Heckel number (K_h) have been calculated according to Equations (5) and (6), in order to better understand the mechanisms involved during compression. The bulk modulus measures the resistance of the bed to volumetric change. In our case, that of uniaxial compression, it is not a true bulk modulus (which is defined considering a unit volume responding to triaxial pressure), however the parameter has been used as it is often encountered in the literature. The Heckel number, from the field of powder compaction [33], is a proportionality constant consequent upon the assumption of proportionality between the change in bed density with pressure and the pore fraction.

$$K_b = -V \frac{dP}{dV} \quad \text{Bulk Modulus} \quad (5)$$

$$K_h = \ln \left(\frac{1}{1 - \%TMD} \right) \quad \text{Heckel Number} \quad (6)$$

Considering the small calibre natures first, the bulk modulus plots of Figure 28 and Figure 29 show that AR2220 becomes more brittle as the test temperature is lowered (see also Figure 21 in Section 3.1). For AR2220 at ambient, the bulk modulus plots show initial grain rearrangement/reorientation up to around 15 MPa and 68 %TMD with grains rotating and sliding against and between one another until they reach a constrained or 'locked' state [34,35], with the upper layers compacting first, followed by the lower layers [36]. The bed then follows largely elastic deformation (up to around 30 MPa and 75 %TMD), before plastic deformation mechanisms dominate as the yield stress is exceeded at intergranular contact points (points of stress concentration) leading to local plastic flow. The resultant increase in intergranular contact area slows the increase in contact stresses, as seen in Figure 28, with the transition at approximately 30 MPa from the plateau in bulk modulus (elastic deformation) to steadily increasing bulk modulus with pressure (plastic deformation). As the test temperature is lowered, the granular bed reaches a constrained state at approximately the same %TMD, and stress then rises more rapidly with compression than at ambient (seen in the red and yellow traces of Figure 21), indicating an increase in brittle response component as the temperature is lowered. The same general behaviour was also observed for the AR2211 propellant.

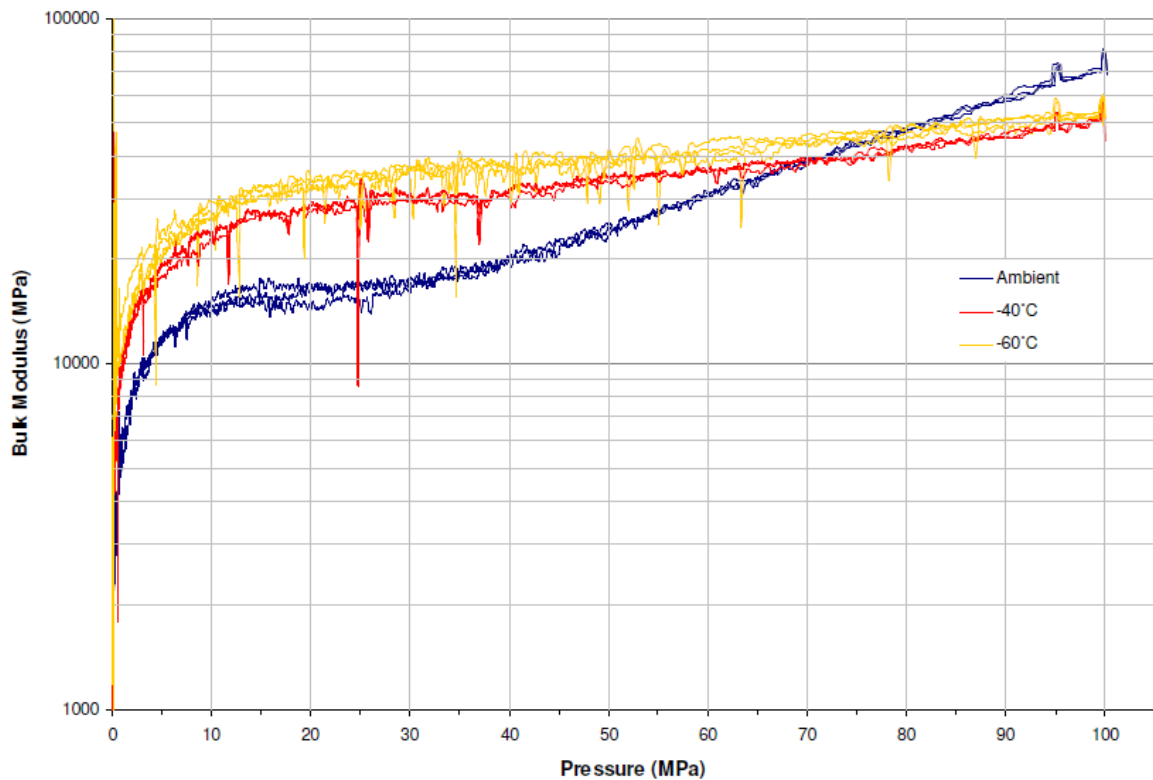


Figure 28: AR2220 bulk modulus versus pressure results at ambient, -40°C and -60°C testing temperatures. Only results within ± 0.5 initial %TMD plotted.

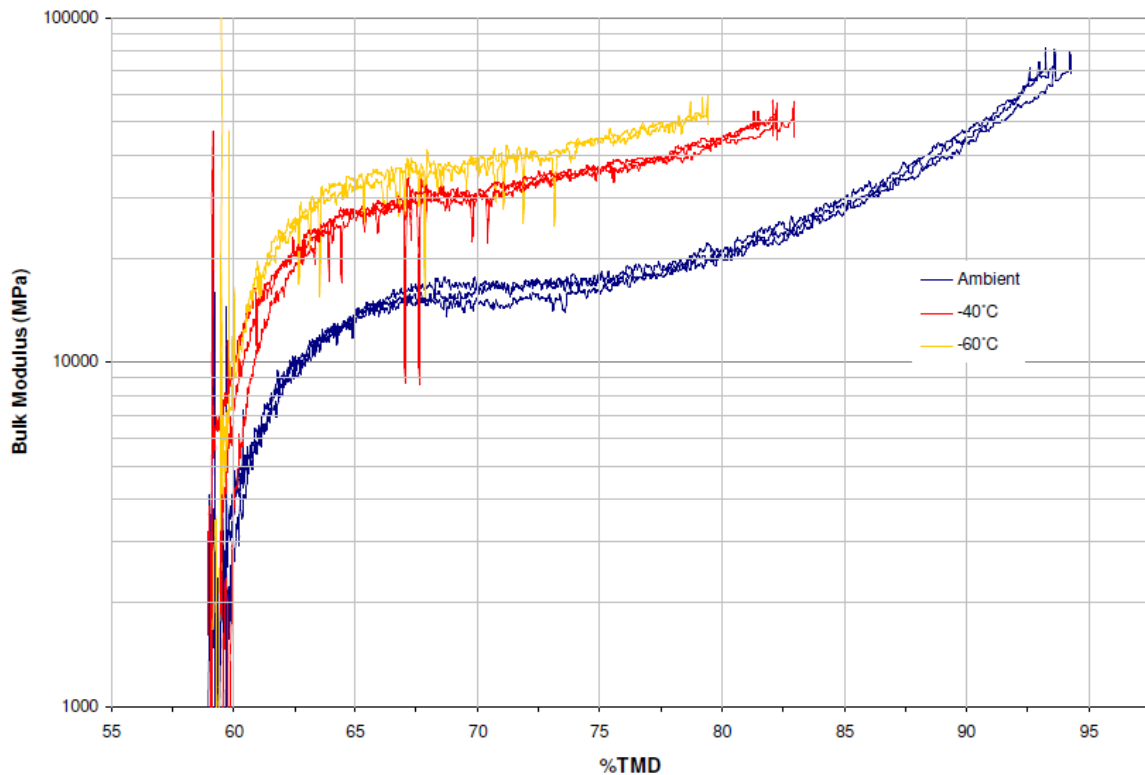


Figure 29: AR2220 bulk modulus versus %TMD results at ambient, -40°C and -60°C testing temperatures. Only results within ± 0.5 initial %TMD plotted.

The Heckel number analysis supports the conclusions drawn from the bulk modulus analysis. In interpreting Heckel plots, the initial non-linear region indicates rearrangement of individual grains (although for materials with low yield strengths, this region may include grain deformation and fragmentation [35]); a linear region indicates plastic deformation [33]; and an upwardly curving section indicates elastic deformation [34]. These three types of behaviour are evident for the ambient temperature trace in Figure 30. At cold temperatures a slight upward curve in the latter stages of compression indicates a level of elastic deformation, although it is known from the visual inspection that some component of plastic deformation also exists at these temperatures. As the density of the compressed aggregate approaches TMD (above say 90 to 95 %TMD corresponding to approximately 75 MPa in Figure 30), elastic compression may be expected, as there will be minimal void spaces remaining into which fragmentation or plastic flow is possible. This behaviour is not evident for AR2220 at high %TMD in the ambient Heckel plot shown in Figure 30, as an upward curving Heckel plot would be expected.

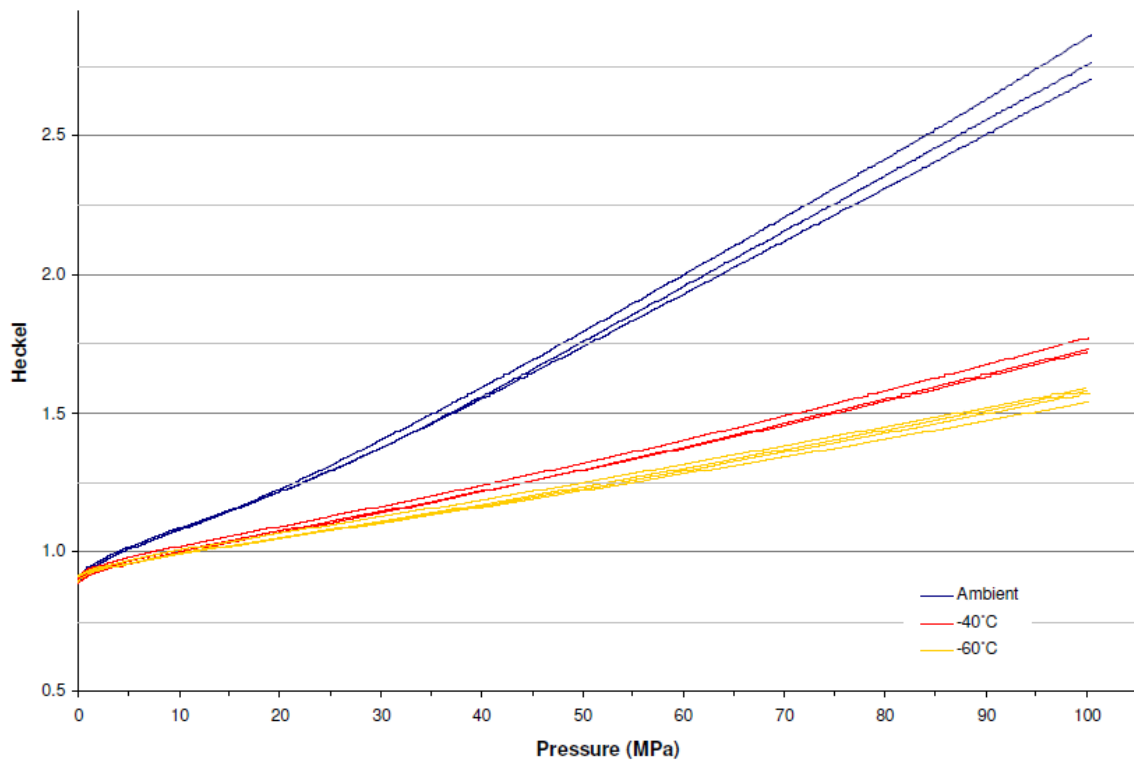


Figure 30: AR2220 Heckel number versus pressure results at ambient, -40°C and -60°C testing temperatures. Only results within ± 0.5 initial %TMD plotted.

Further insight into the compaction mechanisms of the AR2220 propellant as a function of test temperature is afforded by comparing its applied stress versus %TMD characteristics with those of the AR2211 propellant, see Figure 31. Both propellants have similar compositions, differing primarily in grain form. As may be seen most clearly with the ambient results, although AR2211 has a higher initial packing density owing to its lower propellant grain aspect ratio (see Section 2.2.4), AR2220 reaches a higher final packing density, the traces crossing at an applied stress of approximately 20 MPa. This is attributed primarily to the lower contacting surface area of the higher aspect ratio AR2220 propellant, leading to higher contact stresses, and hence greater yield and plastic flow into intergranular voids. The observation that the -60°C traces do not cross, but continue largely parallel, indicates the lack of plastic deformation when undertaking bed compression at this temperature. That at -40°C there is a cross over, or at least convergence, of AR2211 and AR2220 stress versus %TMD traces indicates the presence of some degree of plastic deformation under compression at this temperature.

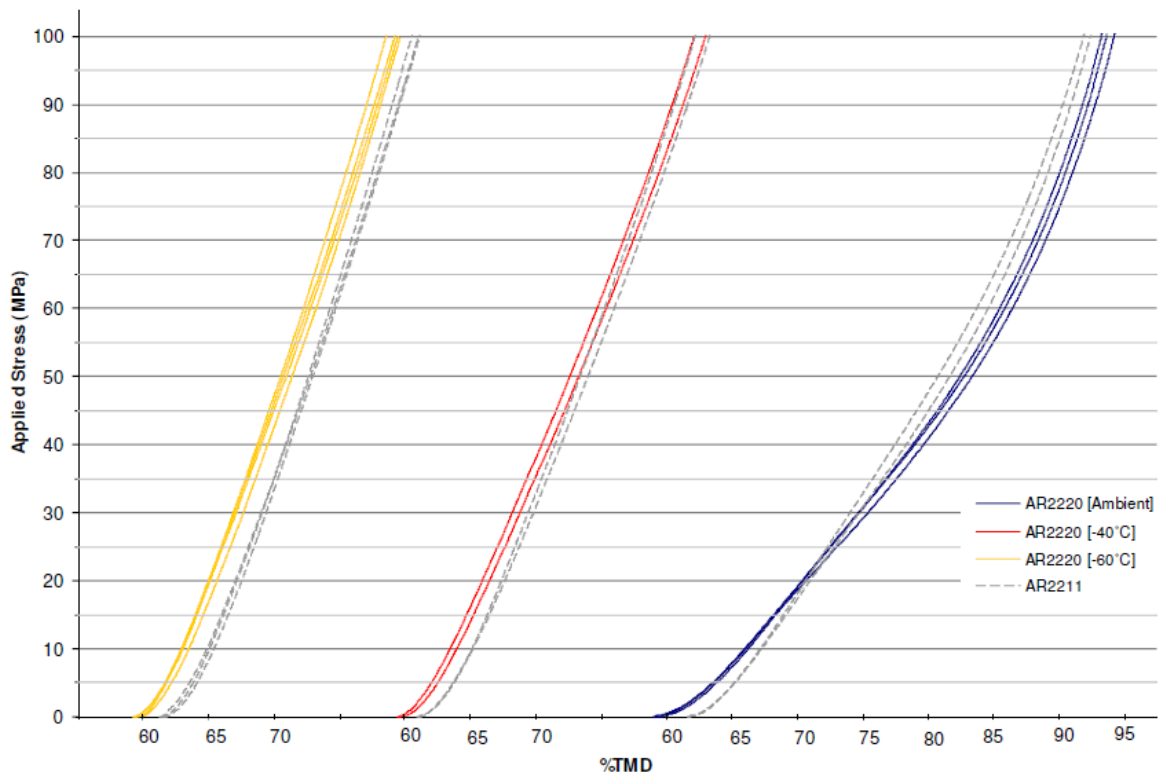


Figure 31: AR2220 stress-%TMD comparison with AR2211, at ambient, -40°C and -60°C testing temperatures. Only results within ± 0.5 initial %TMD plotted.

For the large calibre propellants FNH-025 and BS-NACO, visual inspection showed a far greater extent of brittle fracture than was the case for the small calibre natures, especially at low test temperatures. This appears on the applied stress-%TMD plots (Figure 23 for FNH-025 and Figure 27 for BS-NACO) at low temperatures as characteristic 'saw-tooth' stress build-up and release traces. Following granular bed locking, stress rapidly rises with compression until brittle fracture occurs in a grain. This occurs at the lowest applied pressure and %TMD when crushing at -60°C. Following grain fracture, stress is momentarily relieved as grain fragments fill intergranular voids, increasing the level of bed consolidation. As the piston continues to compress the bed, the stress build up-fracture-stress relief cycle continues. The earlier onset and more frequent fracture at -60°C indicates that the propellant is more brittle at this test temperature than at -40°C.

Hence, for the large calibre propellants, which are prone to brittle fracture at -60°C, particularly FNH-025, the applied stress versus %TMD data show that greater bed consolidation is achieved at this lower temperature, with a lowering of the apparent 'bed modulus' when compared with the -40°C test condition (average slope of the yellow and red traces in Figure 23 for FNH-025). This is supported by the visual inspection of the propellant bed post-compaction which showed a higher proportion of pulverised grains at -60°C (Figure 32 and Figure 33). At -60°C and the applied strain rate of 0.02 s^{-1} , there was no evidence of plastic deformation, thus suggesting that the FNH-025 propellant is very close to its full glass/brittle state at this test condition. Visual inspection of grains tested at -40°C indicated a largely brittle response but some plastic deformation was still evident.

Figure 27 for BS-NACO shows analogous behaviour, with the inclusion of the -15°C test temperature condition showing clearly that at this strain rate, BS-NACO is transitioning from ductile to brittle behaviour as the temperature is lowered, with the -15°C trace having a much more ductile character. The visual evidence suggests that there is still a mixed ductile-brittle (although predominately brittle) mode of response at -60°C for BS-NACO.

Bulk modulus and Heckel plots for the BS-NACO, FNH-025 and AR2211 propellants are provided in Appendix D. For the large calibre natures, the 'jagged' fracture behaviour at cold test temperatures results in fluctuating bulk modulus and Heckel plots. As a consequence, in particular for the bulk modulus, the data is generally presented in terms of the local maximum for visual clarity.

3.2.2 Visual Inspection

For each test temperature, a sample that had undergone bed compression was examined using a fluorescently-illuminated magnifier and categorised according to degree of fracture. The categories were based on an estimation of the volumetric amount of 'fracture' present in the grain being categorised, that is:

- Fracture up to a quarter of the grain's length;
- Fracture between a quarter and half of the grain's length;
- Fracture between half and the full grain length;
- Grain shivered²;
- Web and surface fracture only, and;
- Grain pulverised.

Exemplar FNH-025 grains from each category shown for the three testing temperatures are provided in Figure 32. In the figure, differences in the mode of fracture/deformation at each temperature are evident, with grains crushed at ambient exhibiting more ductile traits, such as evidence of crack propagation by shear deformation and tearing. Note that such an analysis cannot account for internal phenomena beyond those inferable from a surface examination. In addition, difficulty was encountered examining the small calibre natures due to the smaller grain size and graphite coating obscuring smaller signs of fracture. With these limitations in mind, Figure 33 categorises the degree of fracture for AR2211, AR2220, FNH-025 and BS-NACO in terms of percentage by number of grains. Appendix C gives the visual inspection results including degree of fracture by category for each propellant tested.

For FNH-025, as temperature decreases, visual inspection of the grains shows a transition towards brittle modes of fracture, such as snapping. This is likely due to fast crack propagation or cleavage due to the lack of energy dissipation mechanisms available at the lower temperatures; FNH-025 is the most brittle of the propellants tested. BS-NACO showed the same trend with temperature as FNH-025, although with lower fracture proportions as shown in Figure 33. Indeed, BS-NACO did not have any grains 'pulverise' (brittle fracture into fragments all of which are less than half the original grain size) whereas pulverisation was observed for the FNH-025 propellant at -60°C. The small calibre propellants (AR2211 and AR2220) showed visual evidence of plastic deformation at the

² 'Shivered' refers to grains that are fractured along their length into multiple, cohering splinters.

lowest test temperature of -60°C , although to a much lesser extent than that observed at ambient or even -40°C (mainly deformed edges, as in Figure C1.3(A)).

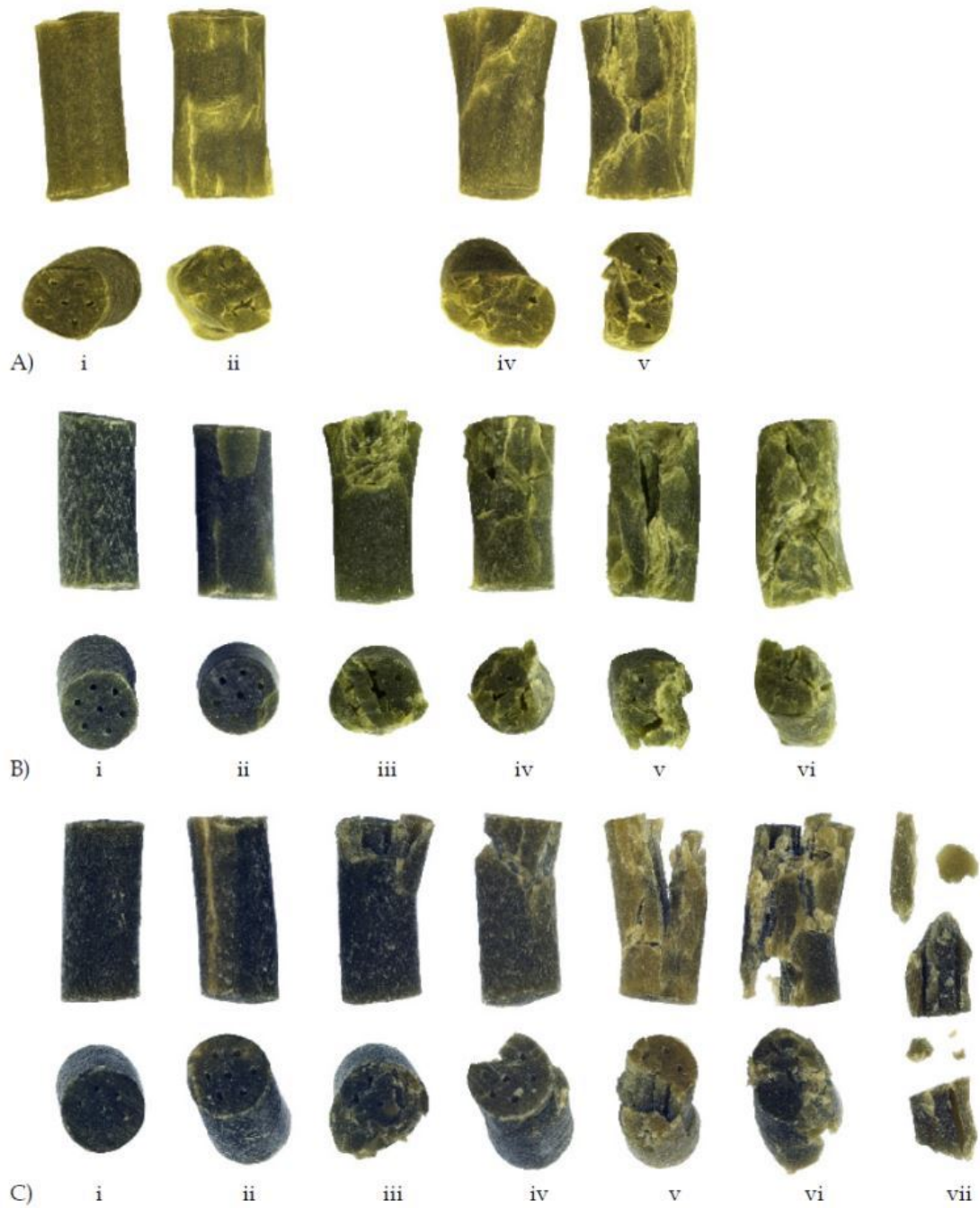


Figure 32: Exemplar FNH-025 grains post compaction. A) compacted at ambient; B) compacted at -40°C and C) compacted at -60°C . i) no fracture; ii) web and surface fracture only; iii) fracture up to $\frac{1}{4}$ grain length; iv) fracture up to $\frac{1}{2}$ grain length; v) fracture up to full grain length; vi) grain shivered; and vii) grain pulverised.

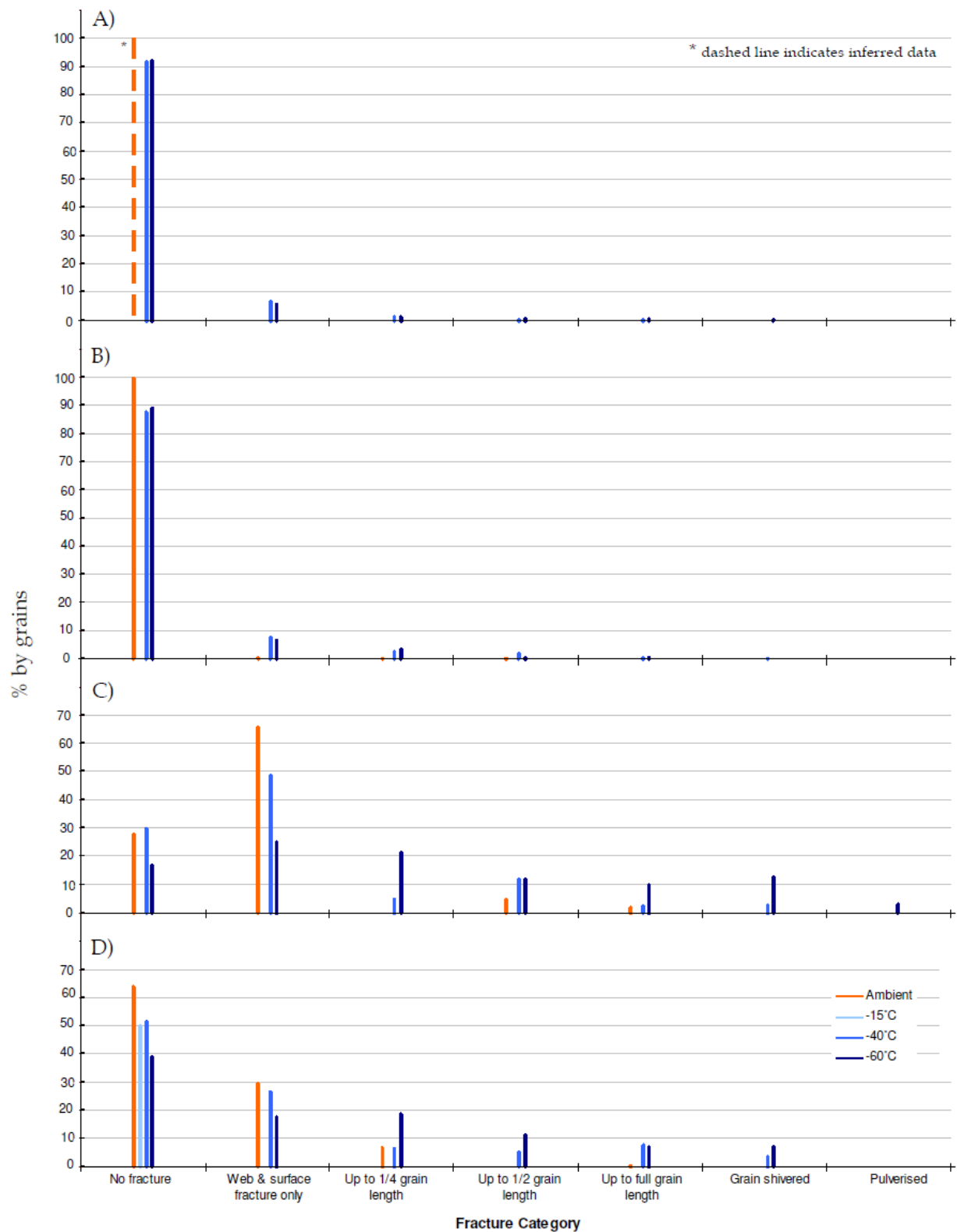


Figure 33: Degree of fracture for unaged propellants by % number of grains as a function of test temperature. A) AR2211; B) AR2220; C) FNH-025; and D) BS-NACO.

Primary factors that determine the relative degree of fracture at a given temperature, pressure and strain rate for single-base propellants are: propellant formulation, including plasticiser levels and NC characteristics such as nitration level and MW distribution; grain geometry (initial packing density due to grain L/ϕ ratio and web thickness); and presence and type of flaws in the propellant grains. The initial packing density is important as it determines the stress distribution upon bed compression, with a higher packing density involving increased intergranular contact area over which to distribute the applied force, thus leading to lower intergranular contact stresses. Increasing web thickness has been stated to increase the resistance to fracture [28]. The degree of fracture for FNH-025 is clearly greater at all test temperatures than for AR2220 and AR2211, as shown in Figure 33, despite having a higher MW (see Table 7). FNH-025 is plasticised, has similar deterrent levels to the AR propellants (although dispersed throughout the grain as opposed to concentrated at the grain peripheries, as is the case with the AR propellants) and is manufactured with the same Grade of NC as the AR propellants, albeit at a lower percentage by weight in the formulation. It is assumed that besides MW (the effects of which are discussed further in Section 3.3.2), from a composition perspective, the presence of plasticiser will have the greatest effect on degree of brittle fracture. As has been noted in the Introduction, the plasticiser will lessen the degree of fracture in the FNH-025 grains, and so the mechanism driving fracture must outweigh this effect; the FNH-025 grain geometry leads to a lower initial packing density, as shown in Figure 4 (see Section 2.2.4), which will lead to higher intergranular stresses at a given applied pressure.

Table 7: MW distribution data for unaged propellant lots used in this study. Values reported relative to polystyrene calibration standards.

Propellant		M_N	M_W	PDI	DOM
AR2210	MEM 4930	57,612 (\pm 4,119)	421,736 (\pm 10,730)	7.3 (\pm 0.4)	Oct 2010
AR2211	MEM 5007	57,163 (\pm 2,730)	425,477 (\pm 9,323)	7.5 (\pm 0.3)	May 2011
AR2220	MEM 4326	56,700 (\pm 4,132)	407,268 (\pm 12,040)	7.2 (\pm 0.6)	Apr 2005
FNH-025	MEM 4003A	60,517 (\pm 3,920)	442,947 (\pm 4,025)	7.3 (\pm 0.4)	Aug 2002
BS-NACO	MEM 4880	49,743 (\pm 2,397)	373,358 (\pm 11,999)	7.5 (\pm 0.2)	Jun 2010

The large calibre propellants only experience 40% of the maximum applied pressure experienced by the small calibre propellants. However, grain-form dependent stress concentration at intergranular contact points is not measured in the experiments, and so the magnitude of the contact stresses are unknown. The FNH-025 web thickness is near identical to that of AR2211 and 20% smaller than that of AR2220. Manufacturer-supplied propellant data sheets show that the FNH-025 lot used for testing has more flaws than either the small calibre propellants or BS-NACO, with proportions of the grains being described as ‘cracked, aerated, badly cut ends and blind perforated granules’. This factor, in conjunction with the stress concentration effects due to grain aspect ratio, and lowered resistance to fracture due to smaller web thickness, proves sufficient to outweigh FNH-025’s superior MW distribution and plasticiser content, leading to the increased degree of fracture for FNH-025 over AR2211 and AR2220. A comparison of FNH-025 and BS-NACO is complicated by additional differences in composition, particularly the lower nitration level of the NC used in BS-NACO and the presence of *n*-butyl stearate. The BS-NACO lot used in this study has a significantly lower prevalence of flaws according to the lot data

sheet, 77% larger average web thickness and a slightly higher initial packing density, all of which would contribute to a lower degree of fracture. However, the BS-NACO lot tested has the lowest NC MW of all of the propellants tested (see Table 7) which, all else being equal, would be expected to increase the degree of fracture.

3.2.3 Time-Temperature Considerations

Owing to the dynamic forces created with ignition in the gun, propellant structural integrity across its operational temperature range is a key attribute in minimising the occurrence, and magnitude, of deleterious gun performance effects such as reduced efficiency [37], abnormally high pressures [38] and breechblow [15]. These effects are exacerbated at lower temperatures due to the nature of polymeric materials, which become brittle and prone to fracture as the temperature is lowered. This phenomenon may be understood by conceiving brittle fracture resistance and resistance to plastic flow as two independent processes, as per [39,40,41]. This results in the situation depicted in Figure 34(a), with low temperatures creating conditions in which the brittle stress is lower than the yield stress, beyond a crossover point known as the glass or brittle-ductile transition point. This point may also be achieved by increasing strain rate rather than lowering temperature, as shown in Figure 34(b). NC undergoes a glass transition at approximately -40°C [14,15], although the transition temperature increases with strain rate [6,13] as a consequence of the viscoelastic nature of the material [42] and is affected by the amount of plasticiser present, as mentioned in the Introduction. Consequently, for a given reference temperature and applied strain rate, a lowering of the test temperature can be used to simulate a higher strain rate environment. The choice of strain rate-temperature conditions will determine how closely the test is able to replicate the strain rates encountered during gun firings, typically $10 - 500 \text{ s}^{-1}$ [43,44,45]. To determine the most appropriate test temperature, all propellant natures in Table 1 (Section 2.1) were tested at ambient, -40°C and -60°C . In addition, BS-NACO was tested at -15°C .

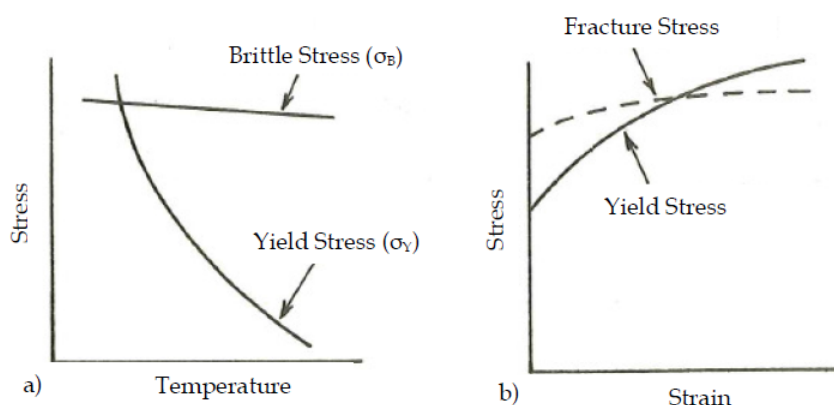


Figure 34: Diagrams illustrating the Ludwig-Davidenkov-Orowan theories of brittle-ductile transitions [5,40]

According to Lieb and Leadore [46], single-base propellants tested in uniaxial compression (single grains tested end-on) exhibit a strain rate-temperature relationship characteristic of viscoelastic materials, despite being semicrystalline in nature, as cautioned by Fong [5].

Fong [5] also cautions that the time-temperature superposition principle does not apply at temperatures below the glass transition temperature, quoting Andrews [47] who states that the principle only holds under conditions in which the free volume is expanding. The result in [46] was based on stress relaxation data acquired from -40°C to $+60^{\circ}\text{C}$ and at 1 s^{-1} .

The test material was M14 single base propellant with a composition of 89% NC (12.6% nitration level), 8% DNT, 2% Dibutylphthalate (DBP) and 1% DPA. The derived temperature-strain rate relationship was then confirmed for the same propellant at four combinations of strain rate-temperature predicted to be equivalent: (100 s^{-1} , 21°C), (10 s^{-1} , 11°C), (1 s^{-1} , 1°C) and (0.1 s^{-1} , -9°C). Confirmation was in the form of agreement in maximum stress, strain at maximum stress, yield stress and strain, compressive modulus, failure modulus and near-identical plots of stress versus strain [48]. Lieb and Leadore concluded that, for the M14 propellant, a decrease in test temperature by 10°C is equivalent to a ten-fold increase in the uniaxial compressive strain rate [46,48].

Table 8 gives the temperature-strain rate ranges simulated by the testing performed for the current study, assuming that the single-base relationship found in [46] applies to the propellants tested and that the bed compression strain rate applies to all of the grains in the bed, an assumption that will be examined in the following paragraph. That is, Table 8 tells us that, taking $20 - 200\text{ s}^{-1}$ to be the strain rate experienced by each grain in a typical gun firing (which is within the range given in [43], [44] or [45], although no data regarding the distribution of the 'typical' strain rates within the propellant charge is given), our test at -40°C simulates typical strain rates in a gun fired at between 0 and -10°C , and our test at -60°C simulates typical strain rates in a gun fired at -20 to -30°C . This conclusion is, however, speculative due to the assumptions mentioned.

Table 8: Strain rate and temperature of test conditions utilised, with corresponding uniaxial end-on grain compression conditions, based on the equivalencies in [46].

Test Conditions Used		Equivalent Compression Conditions	
Strain rate (s^{-1})	Temperature ($^{\circ}\text{C}$)	Strain rate (s^{-1})	Temperature ($^{\circ}\text{C}$)
0.02	-40	20	-10
		200	0
0.02	-60	20	-30
		200	-20

Now consider how the applied macroscopic strain rate (crosshead speed/initial bed height = 0.02 s^{-1}), manifests at the granular level. Initial compaction involves little strain as densification is achieved via grain rearrangement/reorientation [34], initially in the upper grain layers and transferring down into the granular bed [36] until a 'locked' aggregate is formed. Once this aggregate has been formed, force is transferred from the upper piston to the base of the die (and some proportion to the die walls via friction) along force networks comprising contacting grains [49,50]. For quasi-static compression of single base gun propellants, 80 to 95% of the force has been found to be transmitted to the base of the die

[1,2], the balance being either transmitted to the die walls or dissipated in plastic/frictional intergranular processes. Although initially many grains experience little force, as compression proceeds more grains become incorporated into the force network as they are brought closer into contact [51] and the distribution of intergranular force becomes more homogeneous and Gaussian.

Acquisition of actual stress and strain distributions within granular systems has only recently been made possible, through advanced imaging techniques such as high resolution x-ray computed tomography (micro-CT) and micro magnetic resonance imaging (micro-MRI), in conjunction with digital volume correlation (DVC) image analysis [52]. However, for the present study only qualitative statements are possible: grains are less strained the further they are from the piston [52]; intergranular contact points are more highly strained than grain interiors [2]; and, grains within force networks are more highly strained than those that are not [49,50] (noting that the proportion of grains in force networks increases as compression proceeds [51]). In order to relate the macroscopic strain rate to that within individual grains, we wish to know whether the strain rate within a grain (not including at contact stress concentrations) exceeds the average strain rate applied. For the moment, disregard fracture, as well as the intergranular effects of plastic deformation and relative motion. That is, consider a locked aggregate undergoing elastic deformation, but with frictional dissipation to die walls such that a strain gradient exists from the top of the bed to the bottom. As the macroscopic strain rate of 0.02 s^{-1} is an average quantity, being calculated using the pre-compression bed height, the trend across the bulk mass of lower strain towards the base of the bed necessitates, given the fixed piston displacement rate, an average strain rate that is higher than 0.02 s^{-1} towards the upper bed. As such, a level of heterogeneity in the strain rate applied across the grains in the bed exists and, therefore, as stated previously the equivalent compression conditions provided in Table 8 are indicative only.

3.2.4 Stress Relaxation Data

All of the bed compression experiments in the present study were performed with a 5 second hold at maximum test load; the data from between 1 and 5 seconds was used to determine the average relaxation modulus for each propellant-temperature combination using the time-temperature superposition analysis method of [46]. This was done to ascertain the relationship between the test temperature utilised and the equivalent strain rate. However, given the caveats summarised below, these relationships can be considered to be indicative only. Firstly, large-scale fracture is incompatible with the analysis, as it removes the possibility of calculating the macroscopic strain. For the small calibre natures which do not undergo significant fracture, the macroscopic strain is known from piston displacement. However, as is discussed in Section 3.2.3, local strain is not known quantitatively. Secondly, the stress relaxation analysis applies with more certainty to uniaxial compression of single grains, however it may be thought of as applying to average macroscopic strain rates, following on from the discussion of Section 3.2.3. Finally, the previously mentioned cautions of Fong [5] relating to the application of the time-temperature superposition principle for semi-crystalline materials and materials at or near the glass transition point apply.

The first step of the method of Lieb and Leadore [46] involves plotting the logarithm of relaxation modulus (E) against the logarithm of time; see for example Figure 35 for AR2220. The relaxation modulus is found by dividing the applied stress (which decays over the hold period) by the macroscopic strain (constant due to the fixed piston displacement during the hold). Although the test end-point differs in final applied stress between the large and small propellants, this discrepancy is ameliorated by comparing moduli rather than stresses.

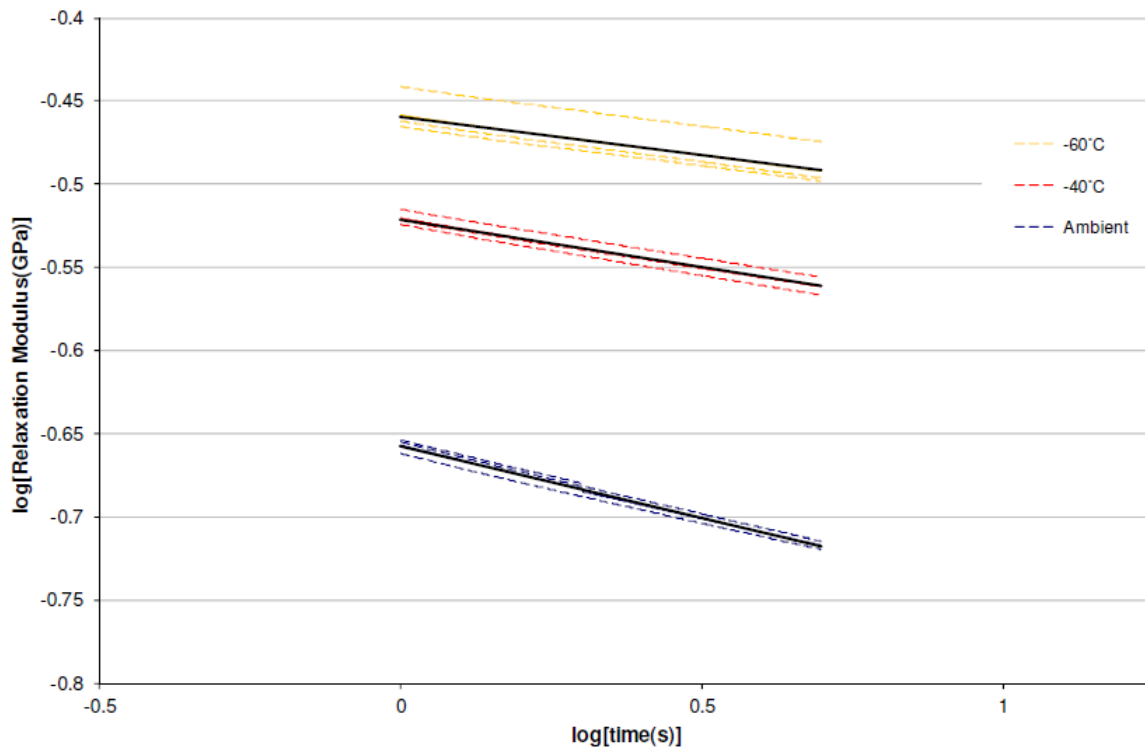


Figure 35: Log Relaxation Modulus versus Log Time for AR2220, data averaged for each temperature shown in solid black.

From the family of curves shown in Figure 35, the cold temperature data were shifted horizontally to form a single curve on an expanded time axis. This was achieved using the method described in [46]: averaging the data for each temperature condition; finding the least squares linear fit to the averaged data; shifting the -40°C curve such that the extrapolation of its linear equation intersects that of the ambient data at the midpoint between the datasets, along the vertical axis; performing the same operation to shift the -60°C data relative to the -40°C data. Vertical shifting was not employed, following the reasoning of the authors of [46], which was experimentally validated, at least for single-grain testing of a range of propellant types, in [48]. The resulting relaxation master curves are shown in Figure 36. The master curves for the small calibre propellants show very good fits to second order polynomial indicating multiple, competing relaxation processes (if the same inference carries over from single grain to bed compression) [46]. This should be treated with caution however, as BS-NACO also shows a very good fit to a second-order polynomial, despite being calculated without a knowledge of actual macroscopic strain. The unshifted ambient FNH-025 data, derived from compressions largely devoid of

fracture, are trustworthy and show an increased rate of relaxation compared with the other propellants. This may be evidence of the increased plasticising effect that the DNT and DBP present throughout the FNH-025 grains impart, although in comparing with BS-NACO, the plasticiser n-Butyl Stearate present in BS-NACO must be considered, along with the lower nitration level of the NC in BS-NACO which can promote improved toughness [53]. Time-temperature shift factors were calculated relative to 20°C, as per [46], and are given in Table 9 and Figure 37, with the single base, single grain M14 results from [46] shown for comparison. BS-NACO and FNH-025 are disregarded in Figure 37 and the remainder of this section, due to the afore-mentioned lack of knowledge of macroscopic strain, and hence relaxation modulus.

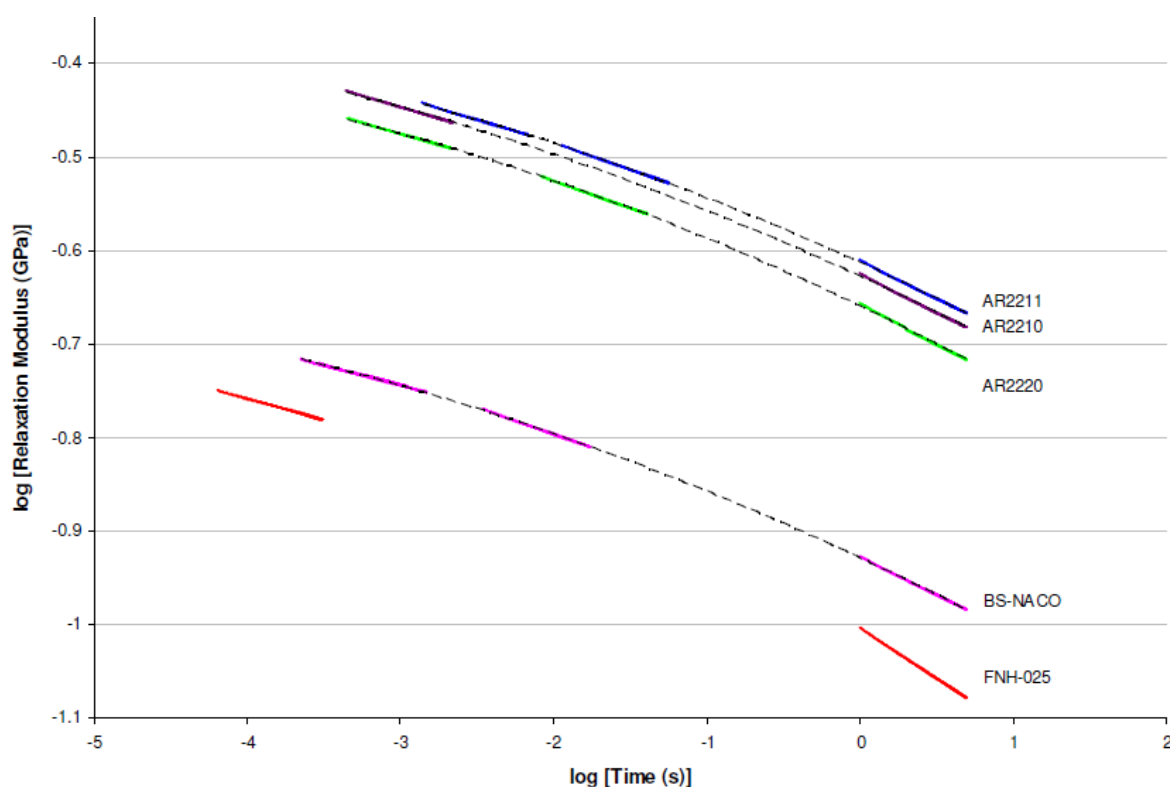


Figure 36: Master relaxation curves without temperature correction (vertical shifting). FNH-025 data incomplete as level of fracture precluded use of the analysis method of [46].

Table 9: Shift factors for AR2210, AR2211 and AR2220, relative to 20°C.

Temperature (°C)	$\log(a_T)$		
	AR2210	AR2211	AR2220
-40	-	1.9	2.1
-60	3.4	2.9	3.3

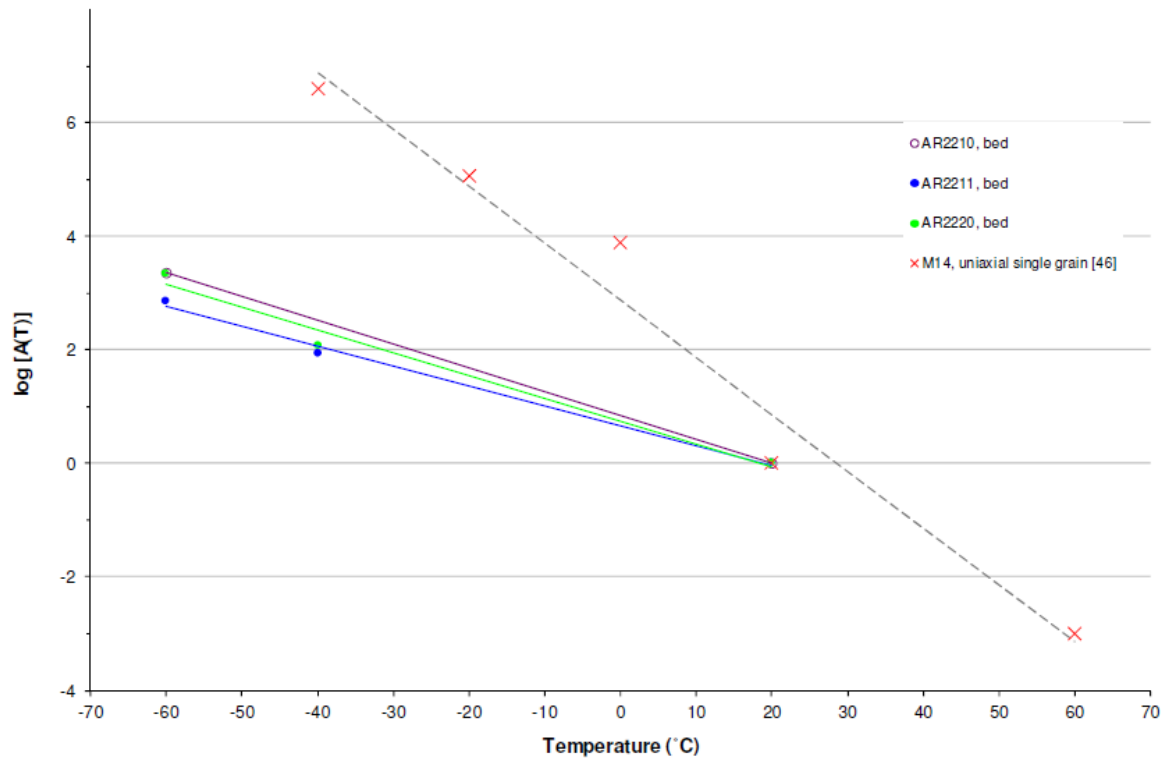


Figure 37: Shift factors used to generate the master curves.

Table 10 shows the results of applying the shift factors for the small calibre natures tested at cold temperatures, to their equivalent strain rates at ambient. It is thought that the equivalent ambient strain rates shown in Table 10 represent the equivalent average strain rate within grains. Referring to the discussion of Section 3.2.3, the strain rate at some points in the bed will be higher, and at some points lower, than this.

Table 10: Strain rate and temperature of test conditions utilised, with corresponding strain rate found using the shift factors in Table 9.

Propellant	Test Conditions Used		Equivalent 'Shifted' Conditions	
	Strain rate (s ⁻¹)	Temperature (°C)	Strain rate (s ⁻¹)	Temperature (°C)
AR2210	0.02	-40	-	20
		-60	45.0	
AR2211		-40	1.8	
		-60	14.5	
AR2220		-40	2.4	
		-60	44.0	

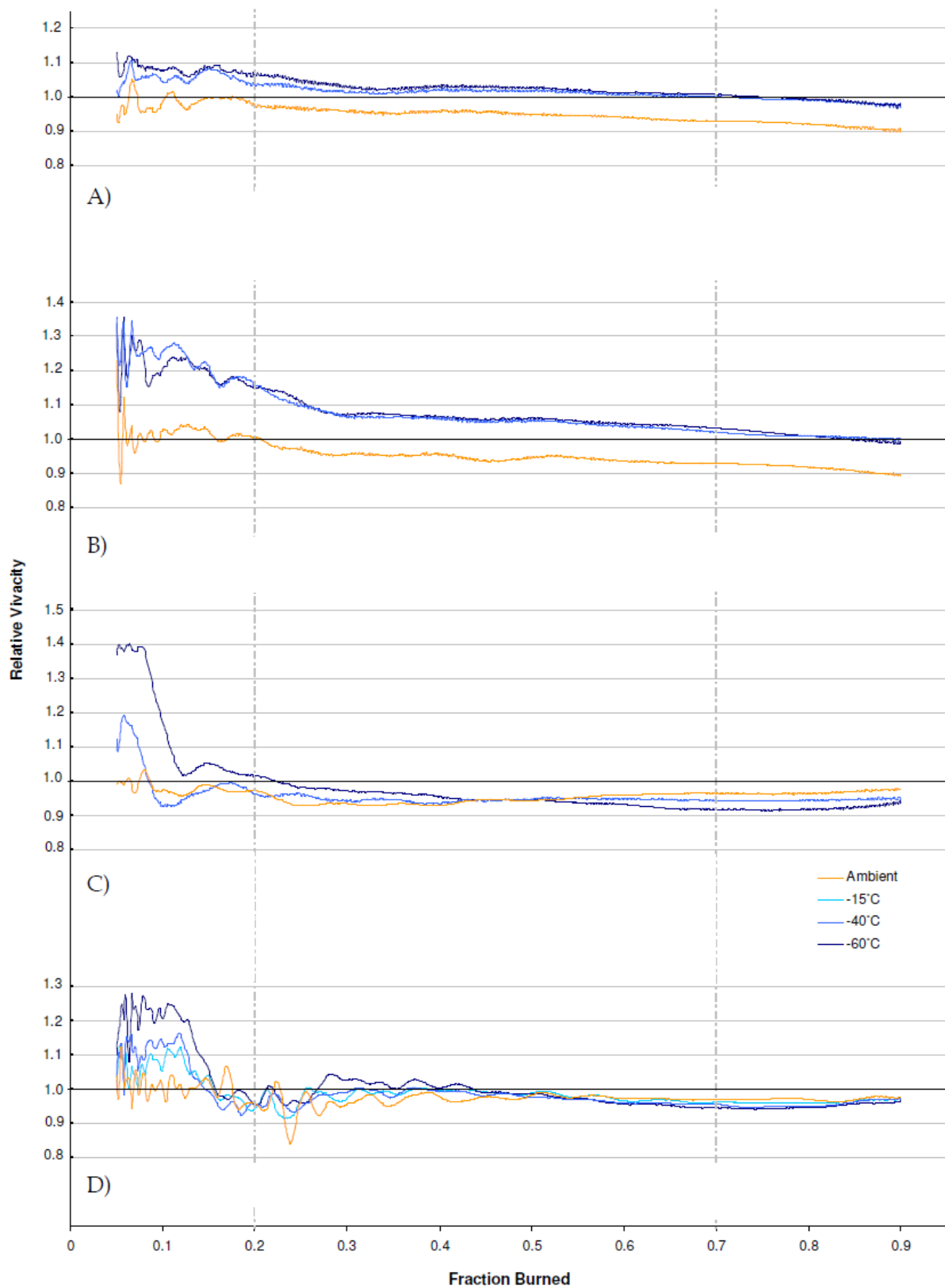
At a test temperature of -60°C , the equivalent strain rates are within the 10 to 500 s^{-1} given in [43,44,45] as strain rates expected in typical gun firings, whereas those at -40°C are somewhat lower. In addition, the visual observations and stress versus %TMD data indicated an increase in brittle behaviour of the propellants crushed at -60°C compared with those crushed at -40°C . Consequently, -60°C was selected as the most appropriate temperature for future testing.

3.3 Damage Induced Surface Area

3.3.1 Relative Vivacity Analysis

Relative vivacity plots are presented in Figure 38, with data presented from 0.05 to 0.9 fraction burned to avoid initial igniter effects and final grain slivering effects, although data prior to 0.1 fraction burned should be treated with caution due to flamespread and variability in propellant ignition [31]. The 0.1 fraction burned quoted by Oberle [31] was derived from simulations of staged sample ignition. It is noteworthy that [54] stipulates the use of 0.3 to 0.7 fraction burned for the plotting of vivacity, although no rationale is provided for the selection of this specific range. Each temperature trace was obtained by averaging the results of at least two closed vessel firings at that temperature. The uncrushed reference data that the results of the crushed samples are presented relative to is also taken as the average of at least two firings. The exception to this is the AR2211 propellant for which only a single uncrushed reference was used owing to spurious results in one of the reference firings.

The relative vivacity of the AR2211 and AR2220 propellants crushed at cold temperatures is greater than 1 throughout the majority of the burn, as shown in Figure 38 (A) and (B). AR2211 crushed at cold temperatures remains elevated until around 0.7 fraction burned, AR2220 until around 0.8. The elevated relative vivacities are likely due to the small grain form giving short combustion times, which, given the heterogeneous ignition associated with pyrotechnic ignition, leads to staged ignition of the sample. Hence, both fractured and unfractured material is being burned across the combustion cycle, leading to a greater burning surface area, and therefore vivacity, in the later stages of combustion. In addition, exposure of the faster burning non-deterred regions of the propellant grain interiors due to grain fracture will contribute to an increase in vivacity over and above the increase due solely to the additional surface area. The different deterrent concentrations and deterrent profiles between the AR2211 and AR2220 propellants, coupled with the differing levels of DISA between the two, will cause the magnitude of these effects to differ across the propellant types. DST Group has recently commissioned a methane-oxygen ignition system for its closed vessel testing that affords more homogeneous ignition [55], thus affording higher fidelity in the early stages of combustion and also mitigating the effects of staged ignition on the interpretation of the relative vivacity plots for small grained propellants with short combustion times. It is recommended that ongoing closed vessel studies being conducted at DST Group that involve deterred propellants include assessment using this ignition method.



The magnitude of the increase in vivacity for AR2220 when tested at low temperatures is greater than for AR2211 throughout the combustion cycle, as seen in Figure 38. The inferior initial packing of the AR2220 propellant due to a higher L/ϕ ratio (see Figure 4, Section 2.2.4), results in higher local contact stresses at a given applied stress. The greater length and reduced packing efficiency of the AR2220 grains also results in a greater proportion of the intergranular contact points occurring along the weaker transverse axis of the grains (the alignment of the NC polymeric chains parallel to the extrusion axis during the manufacturing process confers increased grain strength in the longitudinal direction). The AR2220 MW was also smaller than its AR2211 counterpart at the time of testing (see Table 7, Section 3.2.2). Given the similarity in formulation between the AR2211 and AR2220 propellants, this could lead to an enhancement in the structural integrity of the former, as the strength of the NC polymeric structure increases with increasing MW, as illustrated in Section 3.3.2. These complimentary effects will be offset to some extent by the 15% larger web thickness of AR2220 over AR2211 which, all else being equal, should increase the resistance to fracture. The net effect of these differences is that, at ambient test temperatures where a greater portion of stress relief occurs via plastic deformation, the AR2220 undergoes a greater level of bed consolidation at maximum applied pressure when compared with AR2211, despite having an inferior initial packing density (refer to Figure 31, Section 3.2.1). At cold test temperatures where brittle fracture predominates, the AR2220 undergoes greater levels of fracture than AR2211 as evidenced by the relative vivacity curves and as summarised in Table 11.

Table 11: Initial surface area relative to uncrushed reference, determined using the method of Stein and Jahnk [28]

Propellant	Ambient	-40°C	-60°C
AR2211	0.99	1.04	1.07
AR2220	0.99	1.14	1.14
FNH-025	0.92	0.95	1.02
BS-NACO	0.95	0.99	1.04

The large calibre propellants exhibit different behaviour to the small calibre propellants. For both FNH-025 and BS-NACO, heightened relative vivacities occur primarily in the initial 15% of the combustion cycle. From that point the relative vivacities drop in a more rapid fashion in terms of fraction burned compared to the small calibre propellants. This is attributed to the longer combustion times associated with the larger grained, slower burning propellant reducing the influence of heterogeneous ignition on the vivacity data over the combustion period of primary interest. In turn, this allows a better extrapolation of bed burning to grain burning behaviour. Figure 32 and Figure 33 of Section 3.2.2 show that, for FNH-025, bed compaction at both -40°C and -60°C produced significant amounts of: small, loose fragments; fines of different sizes; and internal cracking and crushing. The proportion of small fragments increases from -40°C to -60°C (Figure 33), with the proportion of grains experiencing some type of fracture also increasing at the expense of undamaged grains and grains with minor surface and web cracking. These small particles would be expected to be consumed during the initial phases of burning, contributing their mass to an increased rate of initial pressure rise and potentially providing an ignition enhancement effect. The larger the sample mass contained in these fragments, the lower the mass remaining later in the combustion cycle. This is reflected by the greater decline in

relative vivacity for the -60°C FNH-025 sample compared to its -40°C counterpart. The same trend is seen with BS-NACO across the range of cold testing temperatures. BS-NACO also exhibits oscillations in the vivacity data between approximately 0.15 and 0.3 fraction burned. This results from oscillations in the pressure data and is a characteristic of the BS-NACO propellant. The origin of these oscillations are perhaps explained by Pauly and Sheibel [56], who have found evidence of pressure oscillations due to standing pressure waves within perforations, however the propellants they studied exhibit larger oscillations than those observed for the BS-NACO propellant [57]. Regardless of their origin, as they occur around 0.2 fraction burned, they will affect the calculated DISA values.

The relative surface area values for the compressed samples are summarised in Table 11. They show a reduction in initial surface area at ambient for all propellants considered. This is attributed to the greater level of plastic deformation at ambient testing conditions resulting in a reduction in the initial surface area available for combustion due to perforation closure of a portion of grains in the propellant bed. FNH-025 and BS-NACO, having a higher proportion of surface area due to the perforations than AR2211 and AR2220, incur a larger decrease in initial surface area when perforations are closed. The previously-noted issues associated with the presence of deterred layers and the influence of heterogeneous ignition for the small calibre natures reduces confidence that the values for relative surface area can be used to quantify actual surface area changes, and should be taken only as relative measures applicable for a given propellant type. This is especially apparent as the visual evidence summarised in Figure 33(B) for AR2220 indicates only minor degrees of fracture, making its DISA values at cold temperature seem excessively high. However, whilst the reported DISA values may not relate specifically to the physical surface area generated when considering deterred propellants or surface impregnated propellants, they do reflect the effect of the mechanical damage incurred on the initial rate of gas generation in the gun and it is this parameter which is of primary relevance from the perspective of gun safety and performance.

For the large calibre FNH-025 and BS-NACO propellants, the longer combustion times and use of propellants that are either undeterred or have deterrent homogeneously distributed through the grain, lessen the effect that heterogeneous ignition will have on use of the relative vivacity method. Thus, the data presented in Figure 38 would be expected to provide better instantaneous measures of relative surface area throughout the combustion cycle than for the small calibre natures.

Considering then FNH-025, which when crushed at -60°C produced significant amounts of small grain fragments and minimal visual evidence of perforation closure, Figure 38 shows a high initial vivacity as previously described, however the DISA value of +2% in Table 11 is certainly lower than the actual increase in surface area. For FNH-025 crushed at -40°C, the -1% change in surface area is suspect, as the high levels of fracture, coupled with minimal observed levels of perforation closure would be expected to result in a net increase, not decrease in surface area. In fact, although results from the initial portions of the combustion cycle must be treated with caution due to igniter effects and flamespread, the initial elevated relative vivacities for the large calibre propellants seem to represent more closely the increases in surface area expected based on visual inspection than those predicted by the method of Stein and Jahnk [28]. This would lend justification to extending

the range of evaluated fraction burned data from 0.2 - 0.7, to closer to 0.1 - 0.7, to better capture DISA effects that are represented in the early stages of the combustion cycle. The improved ignition homogeneity associated with gaseous ignition in the Closed Vessel would allow more of the data in the 0 - 0.2 fraction burned region to be used with confidence in the DISA analysis.

3.3.2 Effect of Molecular Weight Distribution

The literature, e.g. [7], shows that MW distribution directly affects the mechanical integrity of a propellant. In order to study the effect that MW distribution has on the mechanical bed integrity of some of the propellants studied, artificial ageing studies were performed using AR2210, AR2220 and BS-NACO, and were reported in [58]. The BS-NACO applied stress versus %TMD results are reproduced in Figure 39, along with previously unpublished data acquired since publication of [58]. Figure 39 demonstrates the reduction in load bearing capacity of the BS-NACO propellant, with an associated increase in %TMD at a given applied stress, as the ageing duration is increased. Table 12 shows the effect of artificial ageing on the MW distributions for the BS-NACO samples in terms of Number Average Molecular Weight (M_N), Weight Average Molecular Weight (M_W) and the Polydispersity Index (PDI). M_N is that MW with an equal number of molecular chains of both greater and lesser weight. M_W is that MW with an equal weight of molecular chains of both greater and lesser weight. The PDI is the ratio of M_W to M_N and provides a measure of the width of the MW distribution. The measurements were performed using Gel Permeation Chromatography (GPC) and the results expressed relative to a polystyrene calibration standard. Each sample was run in quadruplicate and GPC data reduction was performed in accordance with the ICT method [59].

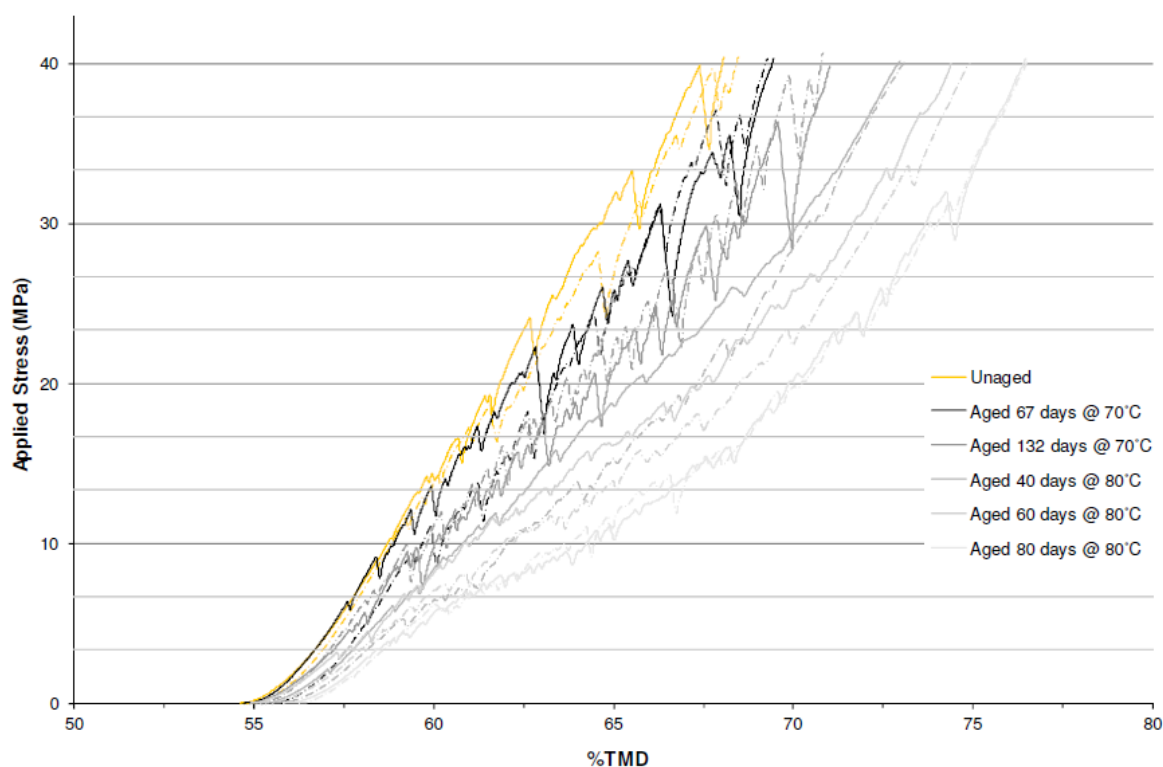


Figure 39: Effect of ageing on load-bearing capability of BS-NACO. Bed compression at -60°C and 0.02 s^{-1} .

Table 12 MW distribution data for BS-NACO aged for various time periods at 70°C and 80°C . Changes in MW values with age relative to the unaged propellant are shown in brackets.

Ageing	Equivalent years at 25°C *	M_N	M_W	PDI
-	0	49,040	370,220	7.5
67 days at 70°C	19.3	46,130	288,560	6.1
132 days at 70°C	37.9	36,880	174,590	4.7
40 days at 80°C	37.8	33,240	153,320	4.6
60 days at 80°C	56.7	25,440	126,280	5.0
80 days at 80°C	75.6	18,320	70,010	3.8

* Calculated assuming the conservative decomposition kinetics of [60]

Figure 40 shows the effect of ageing duration on degree of fracture when crushed at -60°C . The data in Figure 40 result from analysing the samples corresponding to the solid (as opposed to dashed) traces in Figure 39. The exception is the unaged data (reproduced from Figure 33(D)), which was acquired from analysis of one of the two unaged, -60°C crushed, samples presented in Figure 27 that had initial %TMD's within $\pm 0.5\%$. Figure C4.9 to Figure C4.12 in Appendix C give the visual photographic images resulting from the categorisation of these aged samples by degree of fracture.

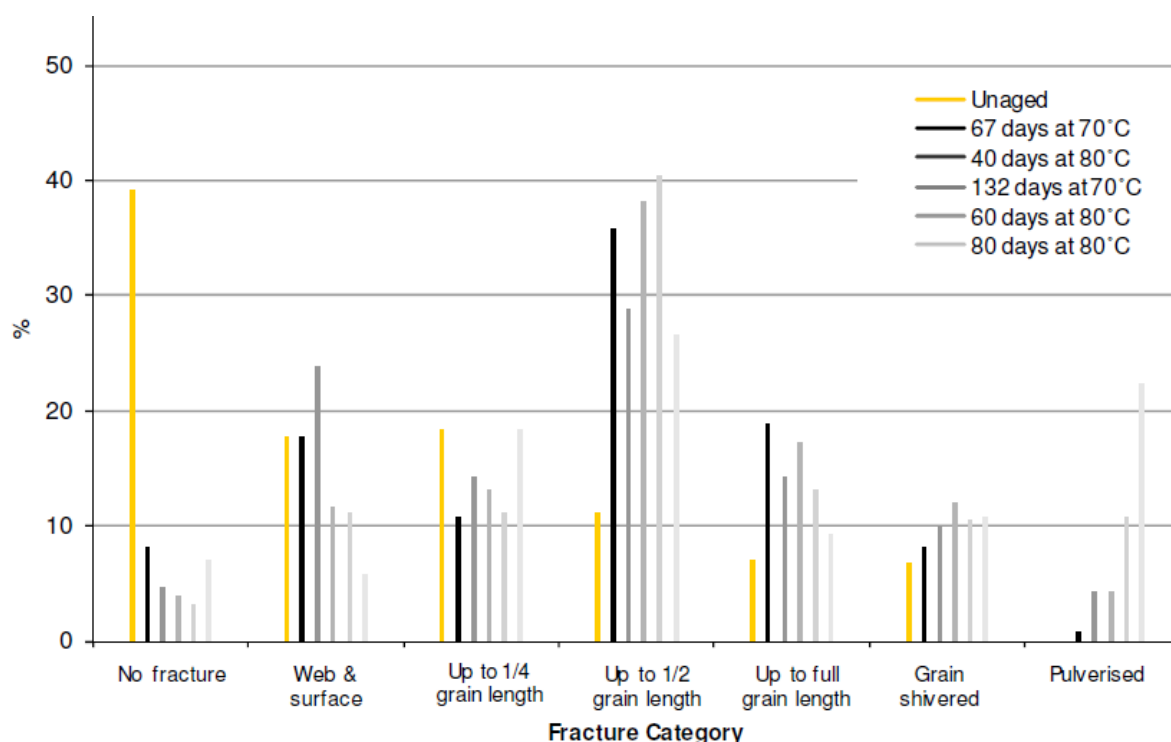


Figure 40: BS-NACO degree of fracture for different ageing periods at 70°C and 80°C. Results reported in terms of % number of grains.

A comparison of Figure 39 and Figure 40 indicates that the strongest correlation with the weakening of the propellant due to artificial ageing, is the proportion of pulverised grains and final %TMD attained following crushing. Figure 41 and Figure 42 show the relationship between MW distribution and final %TMD, and between MW distribution and % grains pulverised. Both parameters (which are derived through visual inspection and applied stress-%TMD data) show clear trends with average MW.

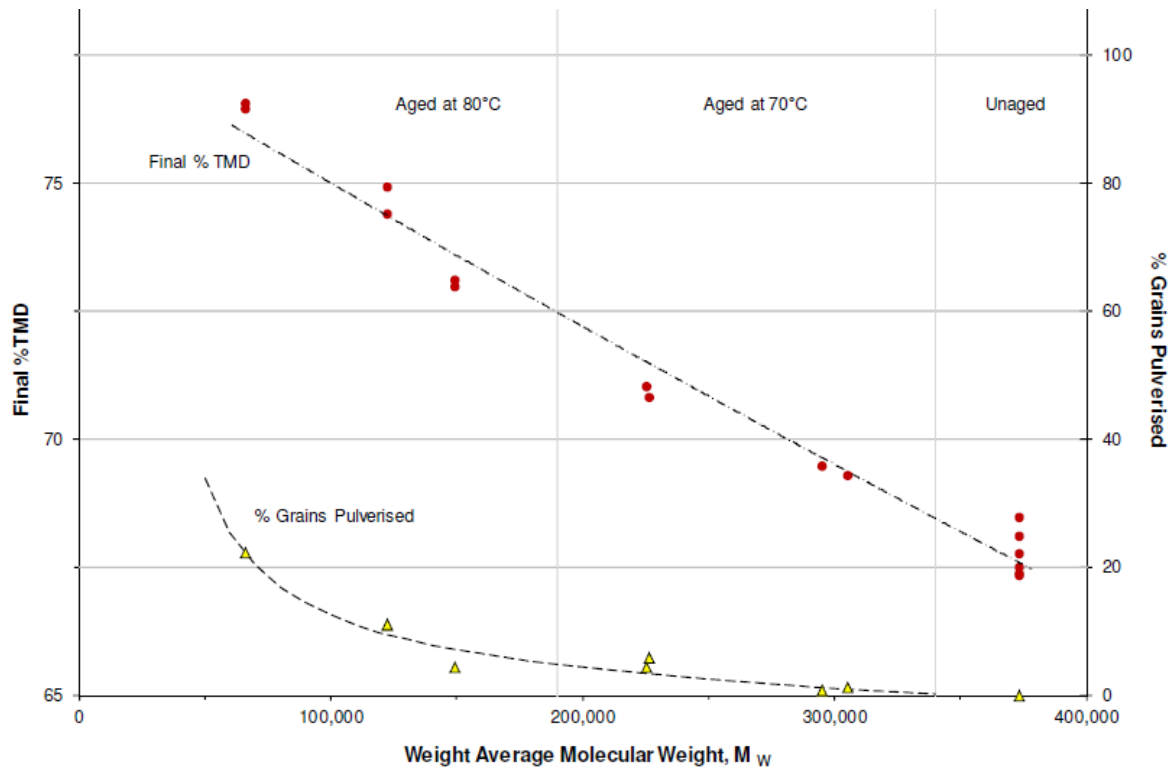


Figure 41: BS-NACO, effect of Weight Average Molecular Weight on Final % TMD and % Grains Pulverised. Samples compacted at -60°C .

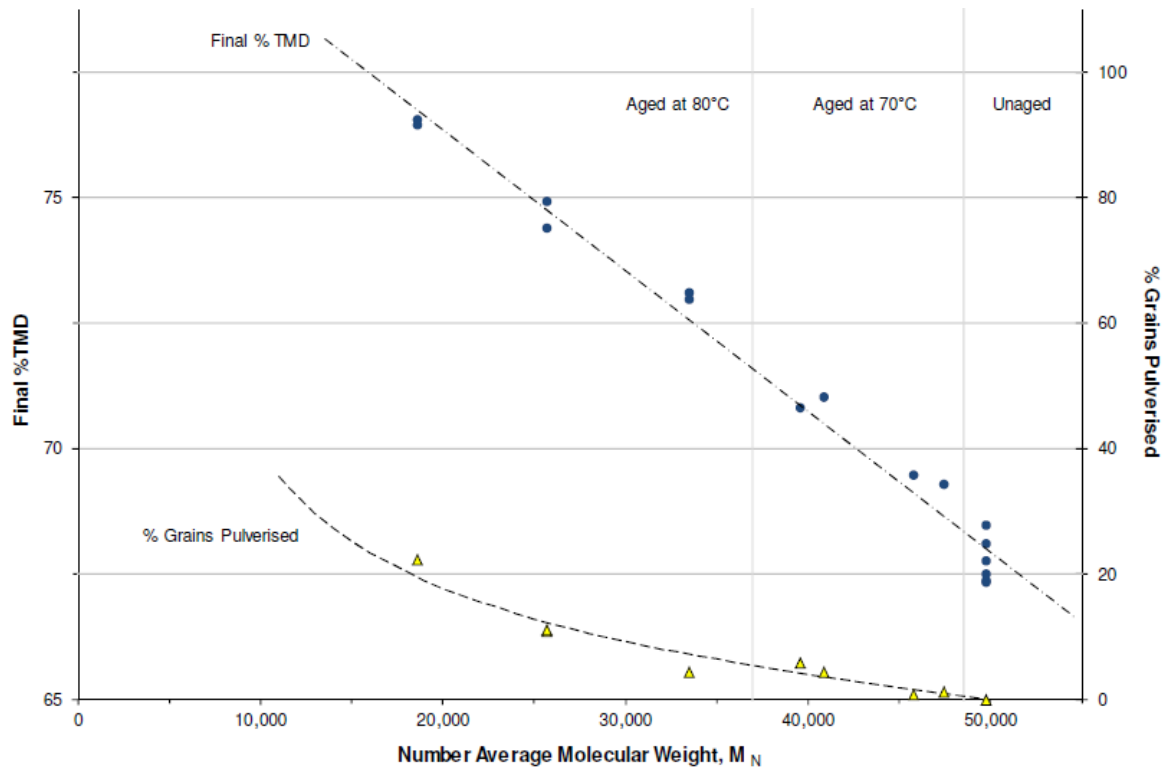


Figure 42: BS-NACO, effect of Number Average Molecular Weight on Final % TMD and % Grains Pulverised. Samples compacted at -60°C .

For the determination of DISA for the aged BS-NACO, the crushed samples were tested in the 700 cm³ vessel, while the aged uncrushed standards were tested in the 200 cm³ vessel due to limitations in the mass of available aged material. The uncrushed data was then scaled in terms of p and dp/dt to account for the use of different closed vessels, with scaling factors determined based on a comparison of the data acquired from testing unaged standard in the 200 cm³ and 700 cm³ vessels. Figure 43 and Figure 44 show the DISA values plotted against M_W and M_N , shown on a logarithmic MW scale, as a strong logarithmic correlation was found to exist. The DISA values as a function of artificial ageing duration are provided in Table 13. Appendix C.4 has photographs of the aged BS-NACO samples following categorisation. Figure 45 and Figure 46 show that for BS-NACO (and presumably other high aspect ratio grains exhibiting significant degrees of fracture when crushed at reduced temperatures), the final %TMD achieved upon bed compaction at -60°C may be used as a predictor of the value for DISA that would result from burning in the closed vessel.

Table 13: DISA due to compaction at -60°C, results shown are for duplicate samples.

Ageing Conditions	DISA	
Unaged	1.07	(1.06, 1.08)
67 days at 70°C	1.13	(1.12, 1.14)
132 days at 70°C	1.27	(1.25, 1.28)
40 days at 80°C	1.31	(1.26, 1.35)
60 days at 80°C	1.51	(1.49, 1.52)
80 days at 80°C	1.75	(1.69, 1.80)

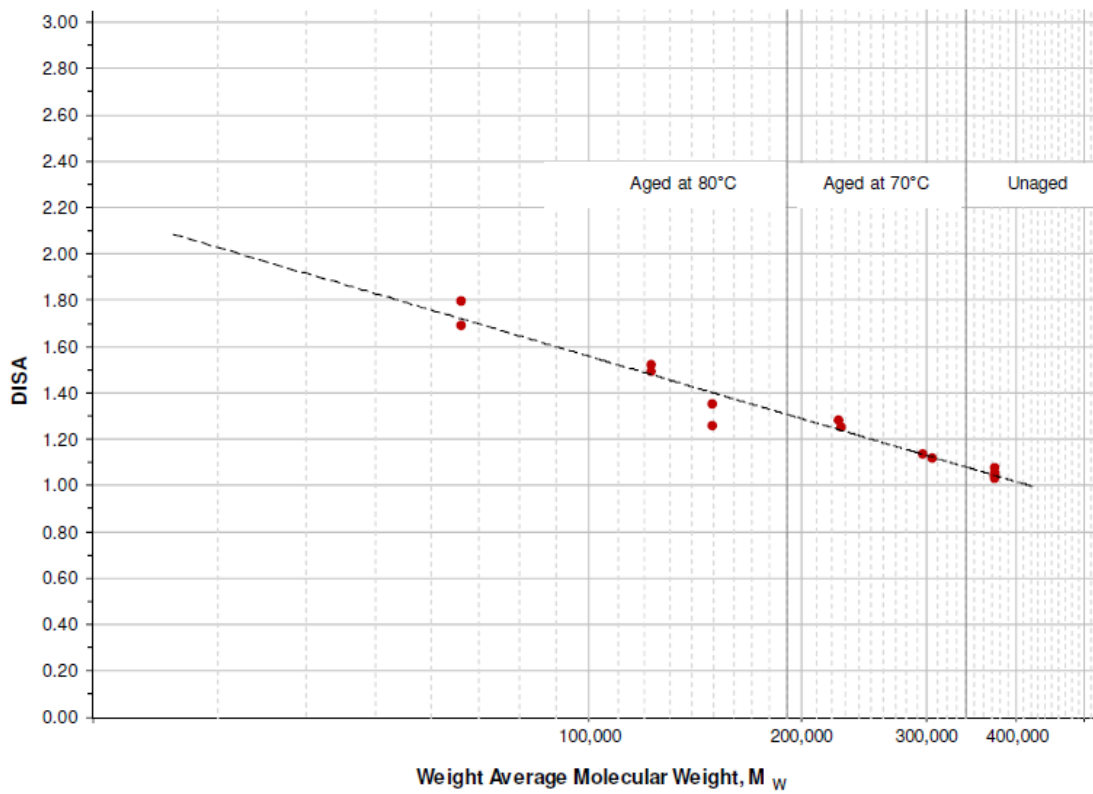


Figure 43: Weight Average Molecular Weight versus DISA, BS-NACO compacted at -60°C .

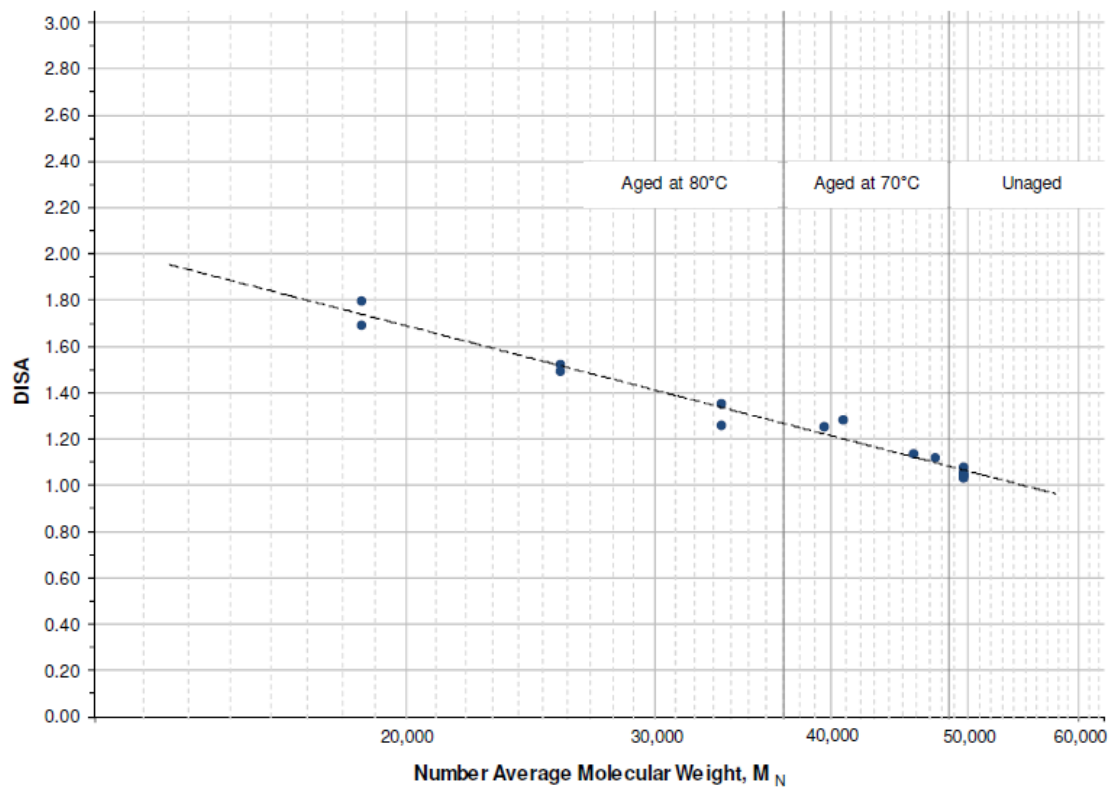


Figure 44: Number Average Molecular Weight versus DISA, BS-NACO compacted at -60°C .

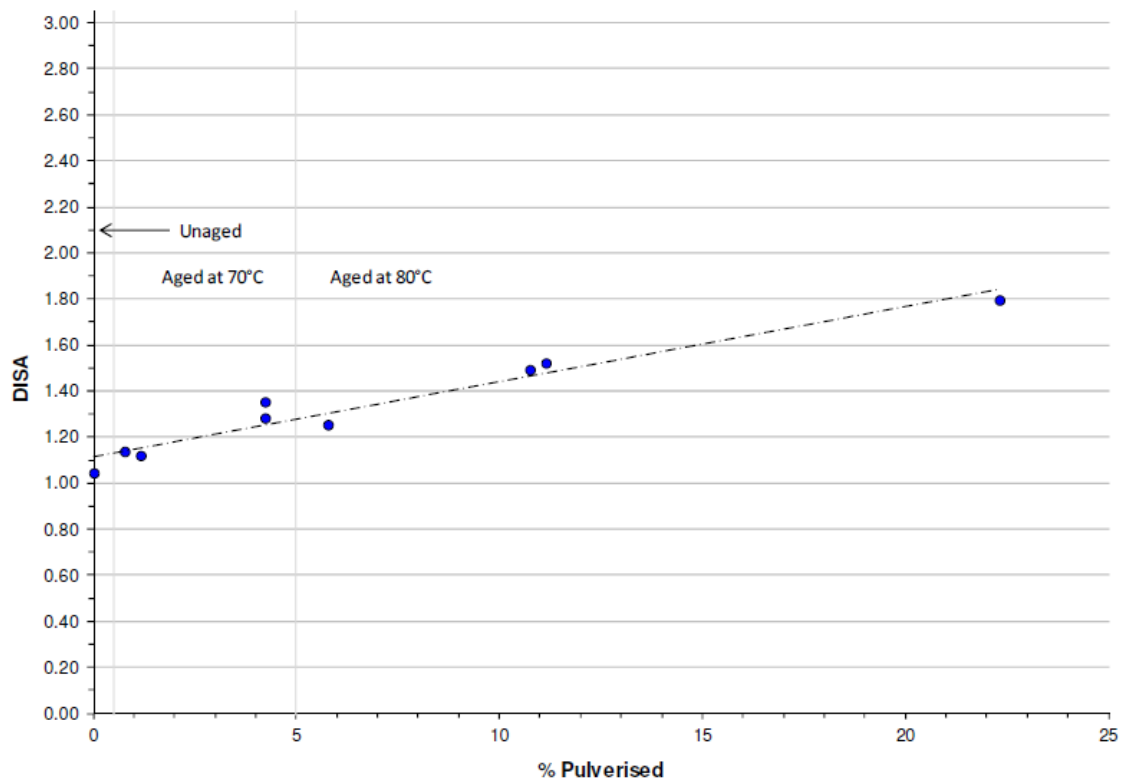


Figure 45: Percentage of Grains Pulverised versus DISA, BS-NACO compacted at -60°C.

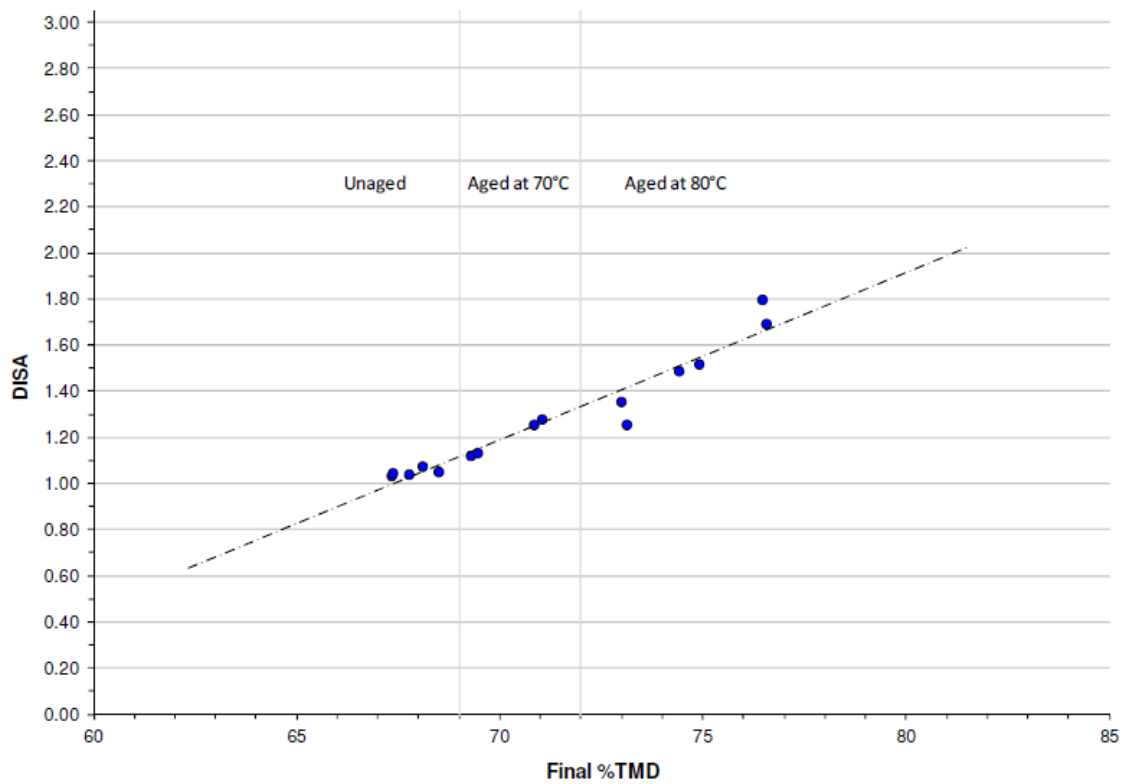


Figure 46: Final % TMD versus DISA, BS-NACO compacted at -60°C.

4. Conclusions and Recommendations

The low strain-rate bed compression test detailed in this report has been shown to provide valuable information regarding compression and fracture behaviour of propellant in representative bed configurations. This provides a useful capability for comparison of the mechanical integrity of propellant natures at low temperatures.

The test results were found to be repeatable, given consistent initial bed packing densities. The repeatable results were firstly attributed to meeting the grain/die dimensional heuristics, which ensures that it is bulk behaviour rather than behaviour overly influenced by that of individual grains that is measured. Other contributing factors include: use of a repeatable bed packing method; use of appropriate temperature conditioning durations; and, use of precise data analysis including radial and axial compliance correction and initial contact point detection method. The largest grained propellant considered, BS-NACO, had a maximum grain dimension to bed diameter ratio larger than that recommended in the literature. The repeatability of results for this propellant crushed at ambient temperature indicated that propellant types no larger than BS-NACO should be tested using this apparatus.

Maximum applied pressures of 100 MPa and 40 MPa were chosen for small and large calibre propellants respectively. Whilst for the large diameter test assembly, the maximum pressure is constrained by the test frame, for the small calibre natures 100 MPa represents a pressure that both produces measureable fracture damage at low test temperatures and is considered to be at the upper end of actual peak chamber pressure differences likely to be encountered during the interior ballistics cycle for small calibre systems. Testing at -60°C, the lower terrestrial temperature of military interest, was found to provide the most brittle response, as expected, with the highest levels of fracture, especially for the large calibre propellants. This was seen via visual inspection, applied stress versus %TMD plots, bulk modulus plots, DISA relative vivacity analysis and via time-temperature shift factors derived from stress relaxation measurements. As the much higher strain rates that act on a propellant bed during ignition in the gun will lead to a predominately brittle response, testing at -60°C provides the advantage of better representing the nature of fracture/deformation expected in the gun environment when compared with bed compaction testing at higher temperatures.

Closed vessel analysis provides insight into the relative amount of fracture, with the same trend found, of increasing DISA with lowering test temperature, as was found by visual inspection and, for the large calibre propellants, from applied stress versus %TMD plots. The accuracy of the DISA evaluation method described in [28] is, however, adversely affected by non-simultaneity of bed ignition and also, for the small calibre propellants, the effect of deterred layers. Ongoing closed vessel studies at DST Group with methane-oxygen ignition are recommended to investigate the effect that more homogenous ignition has on the accuracy of DISA values for both small and large calibre propellants.

All else being equal, a decrease in MW leads to a propellant with lower strength: for a given applied load the propellant undergoes higher levels of fracture under compression at -60°C, with a greater proportion of pulverised grains, lower average bed modulus (i.e. higher final %TMD) and higher DISA.

5. Acknowledgements

The authors gratefully acknowledge the support and assistance of Mr Mark Champion, Mr Mark Davies, Mr Tony Ferschl, Dr Greg Freebairn, Mr Garry Hale, Dr Roger Li, Mr Alby Madaras, Mr Samuel Marmion, Mr Steve Odgers and Mr Michael Ruge.

6. References

- 1 Elban, W. L. (1984) *Quasi-static compaction studies for DDT investigations: Ball Propellants, Propellants, Explosives and Pyrotechnics*, 9, 119 – 129.
- 2 Sandusky, H. W. and Elban, W. L. (1996) *Quasi-static compaction of porous propellant beds. II. Experiments and application of lattice compaction model to cannon propellants*, **Powder Technology**, 89, 219 - 229.
- 3 Lieb, R. J. and Leadore, M. G. (1993) *Mechanical response of gun propellant beds at low strain rates*, **ARL-TR-78**, Aberdeen Proving Ground, Maryland, US Army Research Laboratory
- 4 van Driel, C. A. and de Klerk, W. P. C. (2001) *Functional lifetime of gun propellants*, **Proceedings of the 19th International Symposium of Ballistics**, IB16 139 – 145.
- 5 Fong, C. W. (1979) *Mechanical properties of gun propellants – an assessment of possible approaches to laboratory testing*, **WSRL-0120-TM**, Salisbury, South Australia, Weapons Systems Research Laboratory.
- 6 Pinto, J., Georgevitch, D., Nicolaidis, S. and Wiegand, D. A. (1984) *Dynamic mechanical properties of candidate LOVA and nitrocellulose base gun propellants after up to 18 months of accelerated (high temperature) ageing*, **ARLCD-TR84006**, Dover, New Jersey, Large Caliber Weapon Systems Laboratory.
- 7 Volk, F., Bohn, M. A. and Wunsch, G. (1987) *Determination of chemical and mechanical properties of double base propellants during ageing*, **Propellants, Explosives and Pyrotechnics** 12, 81 – 87.
- 8 Warren, R. C. (1993) *The development of an impact fracture test for large grain gun propellants*, **MRL-TR-93-27**, Maribyrnong, Victoria, Materials Research Laboratory.
- 9 Zimmerman, G. (1985) *Mechanical behaviour of propellant grains under heavy dynamic load*, **AGARD Conference Proceedings No. 392**, September 9 – 11, Florence, Italy pp. 6-1/6-15.
- 10 Fong, C. W. (1985) *Crack initiation in perforated propellants under high strain rate impact conditions*, **Propellants, Explosives and Pyrotechnics**, 10, 91 – 96.
- 11 Lieb, R. J. (1996) *Mechanical response and morphological characterisation of gun propellant*, **ARL-TR-1205**, Aberdeen Proving Ground, Maryland, US Army Research Laboratory.
- 12 Warren, R. C., Odgers, S. G. and Berry, P. (1988) *The effect of various plasticizers on transitions in nitrocellulose*, **WSRL-TM-22/88**, Salisbury, South Australia, Weapons Systems Research Laboratory.
- 13 Wiegand, D. A. (2003) *Changes in the mechanical properties of energetic materials with aging*, **Journal of Energetic Materials**, 21(2), 125 – 140.

- 14 Nicolaidides, S., Wiegand, D. A. and Pinto, J. (1982) *The mechanical behaviour of gun propellant grains in interior ballistics*, **ARLCD-TR-82010**, Dover, New Jersey, Large Caliber Weapons Systems Laboratory.
- 15 Jiang, S.-P., Rui, X.-T., Hong, J., Wang, G. P., Rong, B. and Wang, Y. (2011) *Numerical simulation of impact breakage of gun propellant charge*, **Granular Matter**, 13, 611 – 622.
- 16 Warren, R. C., Odgers, S. G. and Berry, P. (1988) *The effect of various plasticizers on transitions in nitrocellulose*, **WSRL-TM-22/88**, Salisbury, South Australia, Weapons Systems Research Laboratory.
- 17 Krauskopf, L. G and Godwin, A. (2005) *Plasticizers*; in Wilkes, C. E., Summers, J. W. and Daniels, C. (Eds) (2005) **PVC Handbook**. Hanser Verlag. ISBN 1-56990-379-4.
- 18 Sears, J. K., & Darby, J. R. (1982) *The technology of plasticizers*, **Society of Plastics Engineers Monographs**, University of Michigan.
- 19 Australian Defence Standard, DEF (AUST) 5623 (1983) *Methods of test for propellants*, Method 502/83.
- 20 Micromeritics (2008) AccuPyc II 1340 Manual.
- 21 Kooker, D. E., Sandusky, H. W., Elban, W. L. and Conroy, P. J. (1995) *Quasi-static compaction of large-caliber granular gun propellant*, **Proceedings of the 15th International Symposium on Ballistics**, Vol. 3, 1-9, Jerusalem, Israel.
- 22 Zhang, W. (2006) *Experimental and computational analysis of random cylinder packings with applications*, [Doctoral thesis] Baton Rouge, LA, Cain Department of Chemical Engineering.
- 23 NATO Standardisation Agreement (STANAG) 2895, Edition 1 (February 1990) *Extreme climatic conditions and derived conditions for use in defining design/test criteria for NATO forces materiel*.
- 24 Allied Ordnance Publication (AOP) 7, Edition 2, (2004) *Manual of data requirements and tests for the qualification of explosive materials for military use*, CH/102.01.090.
- 25 Lamé, G. and Clapeyron, B. P. É. (1833) *Mémoire sur l'équilibre intérieur des corps solides homogènes*, Mémoires présentés par divers savans, Vol. 4.
- 26 Timoshenko, S. (1948) *Strength of materials part 2: Advanced theory and problems*. Toronto, D. van Nostrand Company, 2nd Edition, p. 239.
- 27 Roark, R. J. and Young, W. C. (1975) *Formulas for stress and strain*, New York, McGraw-Hill, 5th Edition, p. 504.
- 28 Stein, W. W. and Jahnk, H. (1988) *Determination of the grain fracture behaviour of propellant beds*, **Proceedings of the 4th International Propellant and Propulsion Symposium**, V-363 – 372.

- 29 Homan, B. E. (2000) *XLGB burning rate reduction program for Excel 97, Version 3.0*, Aberdeen Proving Ground, Maryland, US Army Research Laboratory.
- 30 Homan, B. E. and Juhasz, A. A. (2001) *XLGB: A new closed-bomb data acquisition and reduction program*, **ARL-TR-2491**, Aberdeen Proving Ground, Maryland, US Army Research Laboratory.
- 31 Oberle, W. F. (2001) *Dynamic vivacity and its application to conventional and electrothermal-chemical (ETC) closed chamber results*, **ARL-TR-2631**, Aberdeen Proving Ground, Maryland, US Army Research Laboratory.
- 32 Hart, A. (2009) *Small-scale gun propellant vulnerability screening tests*, **DSTO-TR-2320**, Salisbury, South Australia, Weapons System Division.
- 33 Heckel, R. W. (1961) *Density-pressure relationships in powder compaction*, **Transactions of the Metallurgical Society of AIME**, 221, 671 – 675.
- 34 Mahmoodi, F. (2012) *Compression mechanics of powders and granular materials probed by force distributions and a micromechanically based compaction equation*. [Doctoral thesis] Acta Universitatis Upsaliensis. Digital comprehensive summaries of Uppsala dissertations from the Faculty of Pharmacy 159, ISBN 978-91-554-8319-7.
- 35 Denny, P. J. (2002) *Compaction equations: a comparison of the Heckel and Kawakita equations*, **Powder Technology**, 127(2), 162 – 172.
- 36 Kong, C. M. and Lannutti, J. J. (2000) *Localized Densification during the Compaction of Alumina Granules: The Stage I-II Transition*, **Journal of the American Ceramic Society**, 83(4), 685 – 690.
- 37 Lieb, R. J. and Rocchio, J. J. (1984) *The effects of grain fracture on the interior ballistic performance of gun propellants*, **Proceedings of the 8th International Symposium on Ballistics**, October 23 - 25, APDA, I-25 – I-34.
- 38 Fong, C. W. and Moy, B. K. (1982) *Ballistic criteria for propellant grain fracture in the GAU-8A 30 mm gun*, **AFATL-TR-82-21**, Ballistics Branch, Direct Fire Weapons Division, Florida, Air Force Armament Laboratory.
- 39 Ioffe, A. F. (1929) *Physics of Crystals*, (Gosizdat, Leningrad; University Microfilms, Ann Arbor, 1966).
- 40 Ward, I. M. and Sweeney, J. (2012) *Mechanical properties of solid polymers*. Chichester, John Wiley & Sons, 3rd Edition, p. 414.
- 41 Evstifeev, A. D., Gruzdkov, A. A. and Petrov, Y. V. (2013) *Dependence of the type of fracture on temperature and strain rate*, **Technical Physics** 58(7), 989 – 993.

- 42 Bose, P. and Pandey, K. M. (2012) *Desirability and assessment of mechanical strength characteristics of solid propellant for use in multi barrel rocket launcher*, **International Journal of Chemical Engineering and Applications**, 3(2), 114 – 124.
- 43 Lieb, R. J. (1991) *High strain-rate response of gun propellant using the Hopkinson split bar*, **BRL-TR-3200**, Aberdeen Proving Ground, Maryland, US Army Research Laboratory.
- 44 Tzeng, J. T. and Abrahamian, A. S. (1995) *Dynamic compressive properties of composites at interior ballistic rates of loading - experimental method*, **Composites Engineering** 5(5), 501 – 508.
- 45 Varga, L. (1992) *Impact testing methods for gun propellants*, **Propellants, Explosives and Pyrotechnics**, 17, 126 – 130.
- 46 Lieb, R. J. and Leadore, M. G. (1993) *Time-temperature shift factors for gun propellants*, **ARL-TR-131**, Aberdeen Proving Ground, Maryland, US Army Research Laboratory.
- 47 Andrews, E. H. (1968) *Fracture in Polymers*, Edinburgh, Oliver and Boyd, pp. 16, 72.
- 48 Lieb, R. J. and Leadore, M. G. (1993) *Mechanical response comparison of gun propellants evaluated under equivalent time-temperature conditions*, **ARL-TR-228**, Aberdeen Proving Ground, Maryland, US Army Research Laboratory.
- 49 Drescher, A. and de Josselin de Jong, G. (1972) *Photoelastic verification of a mechanical model for the flow of a granular material*, **Journal of the Mechanics and Physics of Solids**, 20(5), 337 – 340.
- 50 Liu, C. -h., Nagel, S. R., Schecter, D. A., Coppersmith, S. N., Majumdar, S., Narayan, O. and Witten, T. A. (1995) *Force fluctuations in bead packs*, **Science**, 269, 513 – 515.
- 51 Makse, H. A., Johnson, D. L. and Schwartz, L. M. (2000) *Packing of Compressible Granular Materials*, **Physical Review Letters**, 84(18), 4160 – 4163.
- 52 Pan, B., Wu, D. and Wang, Z. (2012) *Internal displacement and strain measurement using digital volume correlation: a least squares framework*, **Measurement Science and Technology**, 23(4), 045002.
- 53 Odgers, S.G. (1994) *The interrelationship between processing, mechanical and ballistic properties for a nitrocellulose based nitramine (RDX) propellant*, **DSTO-TR-0079**, Salisbury, South Australia, Explosive Ordnance Division.
- 54 NATO Standardisation Agreement (STANAG) 4115, Edition 2 (June 1997) *Definition and determination of ballistic properties of gun propellants*.
- 55 Freebairn, G., Huf, J. and Hale, G. (2013) *Evaluation of a methane-oxygen ignition system for closed bomb testing*, **11th Australian Explosives Ordnance Symposium**, November 11-14, Canberra, Australia.

56 Pauly, G. and Sheibel, R. (2008) *Accelerated burning of gun propellants caused by pressure oscillations within the perforations of propellant grains*, **43rd Annual Armament Systems: Gun & Missile Systems Conference & Exhibition**, April 21 – 24, New Orleans, United States of America.

57 Mortimer, J., Huf, J., Weapons and Combat Systems Division, unpublished data, 2013.

58 Hart, A., Mortimer, J., Huf, J., Prior, C., Odgers, S. and Sarunic, M. (2013) *Ageing characteristics of Mulwala Redevelopment Project comparison propellants*, **11th Australian Explosives Ordnance Symposium**, November 11-14, Canberra, Australia.

59 Pontius, H., Dörich, M., Bohn, M., (2008), *Gel Permeation Chromatography of Nitrocellulose (NC) and NC Containing Substances, Part 1*, **39th International Annual Conference of ICT**, June 24 -27, Karlsruhe, Germany.

60 Allied Ordnance Publication (AOP) 48, Edition 2, (2008) *Explosives, nitrocellulose-based propellants, stability test procedures and requirements using stabiliser depletion*, Section 4.4.

61 Miller, M. (1994) *Specific heats of solid gun propellants*, **Combustion Science and Technology**, 102, 273 – 281.

62 Miller, M. (1997) *Thermophysical Properties of Six Solid Gun Propellants*, **ARL-TR-1322**, Aberdeen Proving Ground, Maryland, US Army Research Laboratory.

63 Kadoya, K., Matsunaga, N. and Nagashima, A. (1985) *Viscosity and thermal conductivity of dry air in the gaseous phase*, **Journal of Physical and Chemical Reference Data**, 14(4), 947–970.

Appendix A Engineering Drawings

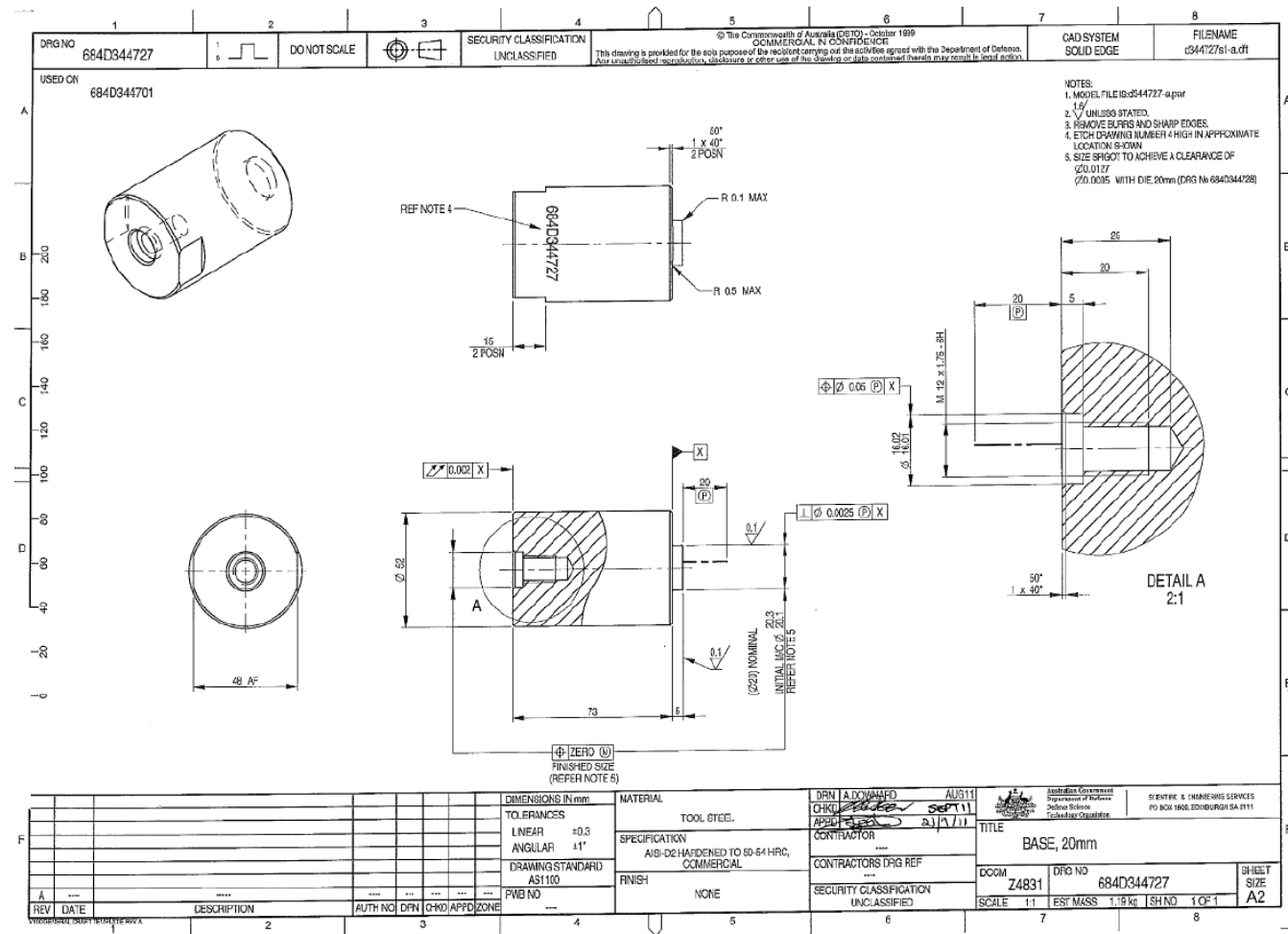


Figure A.1: 20 mm base engineering drawing

UNCLASSIFIED

DST-Group-TR-3291

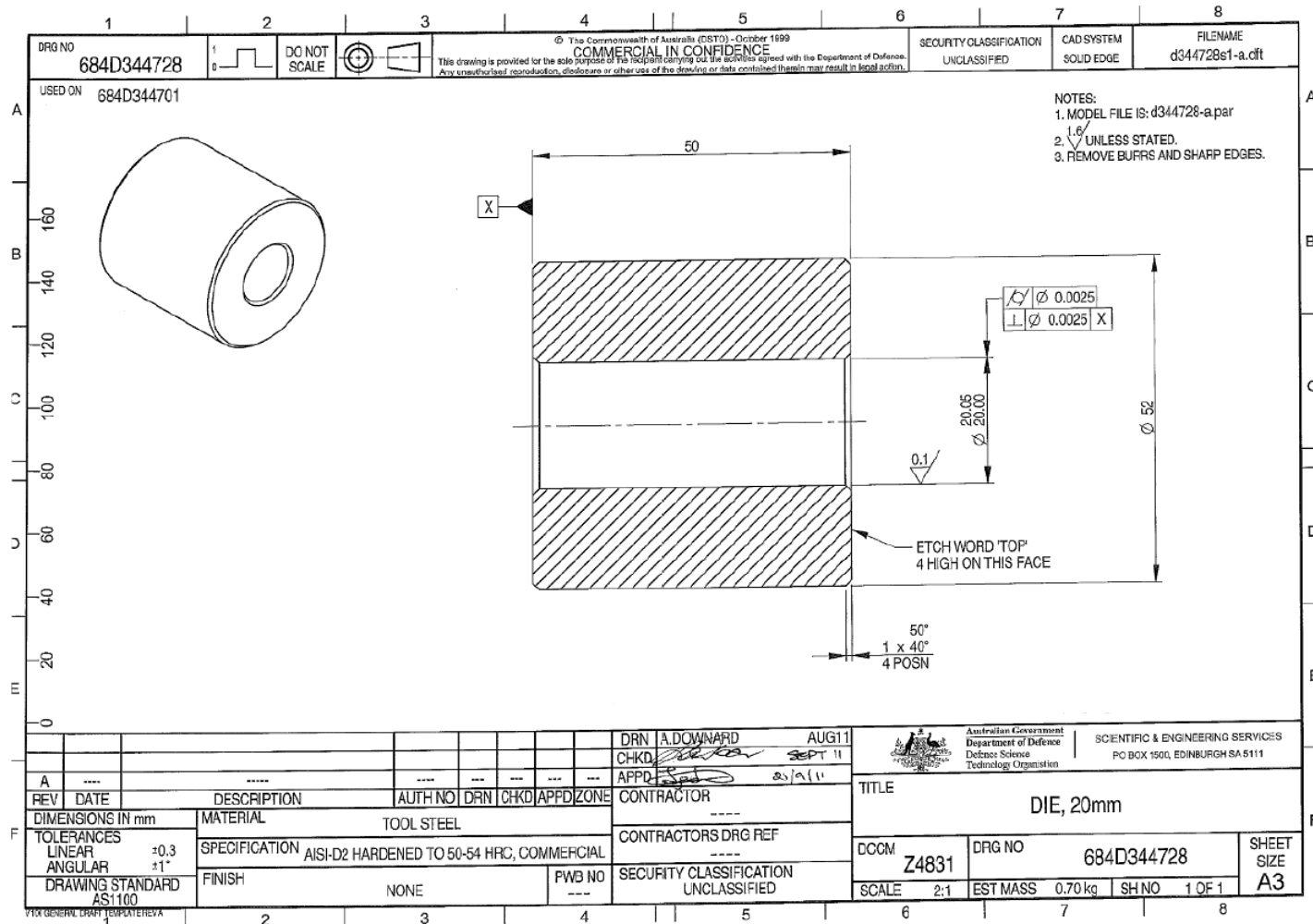


Figure A.2: 20 mm die engineering drawing

UNCLASSIFIED

UNCLASSIFIED

DST-Group-TR-3291

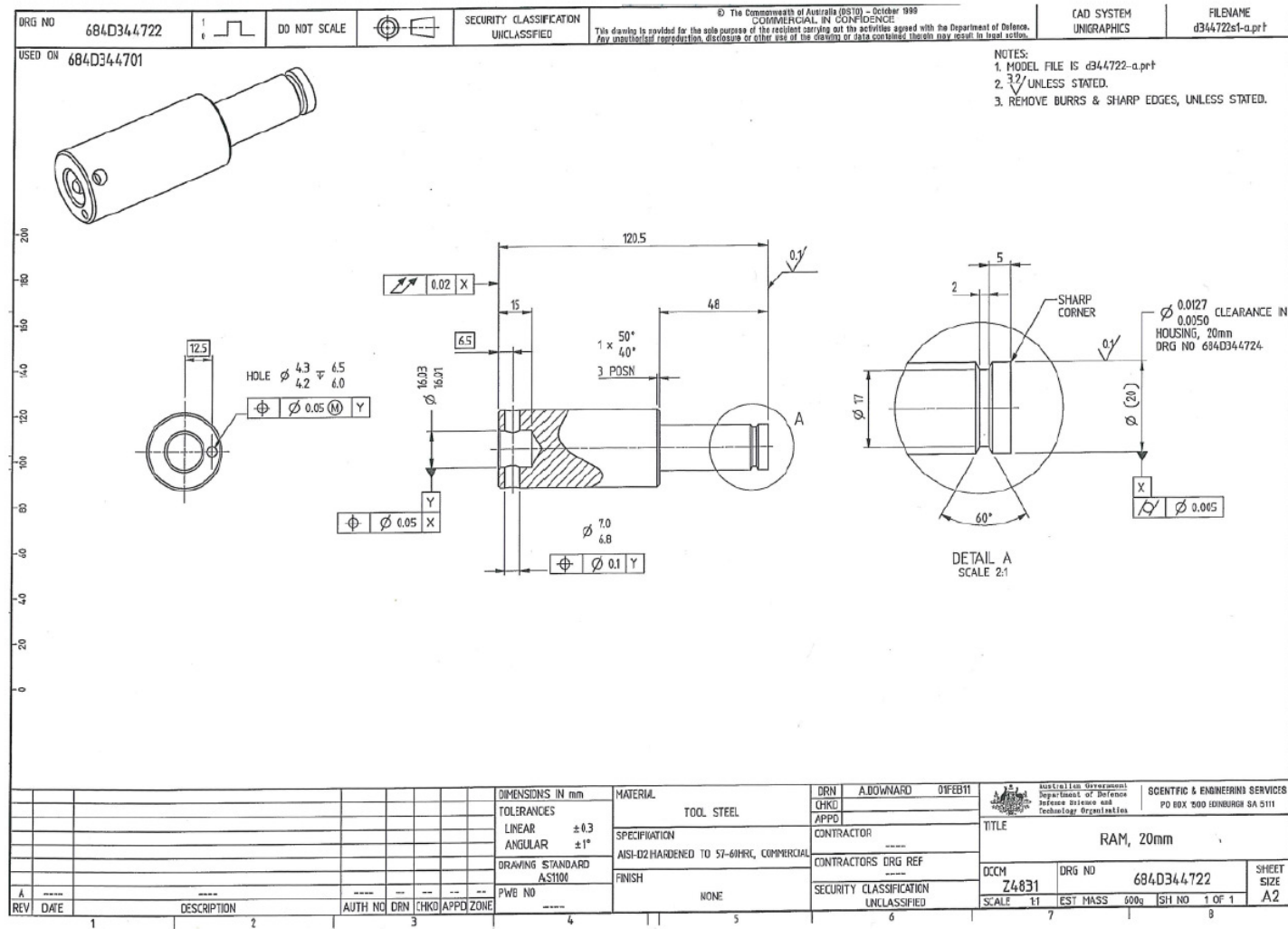


Figure A.3: 20 mm piston engineering drawing

UNCLASSIFIED

UNCLASSIFIED

DST-Group-TR-3291

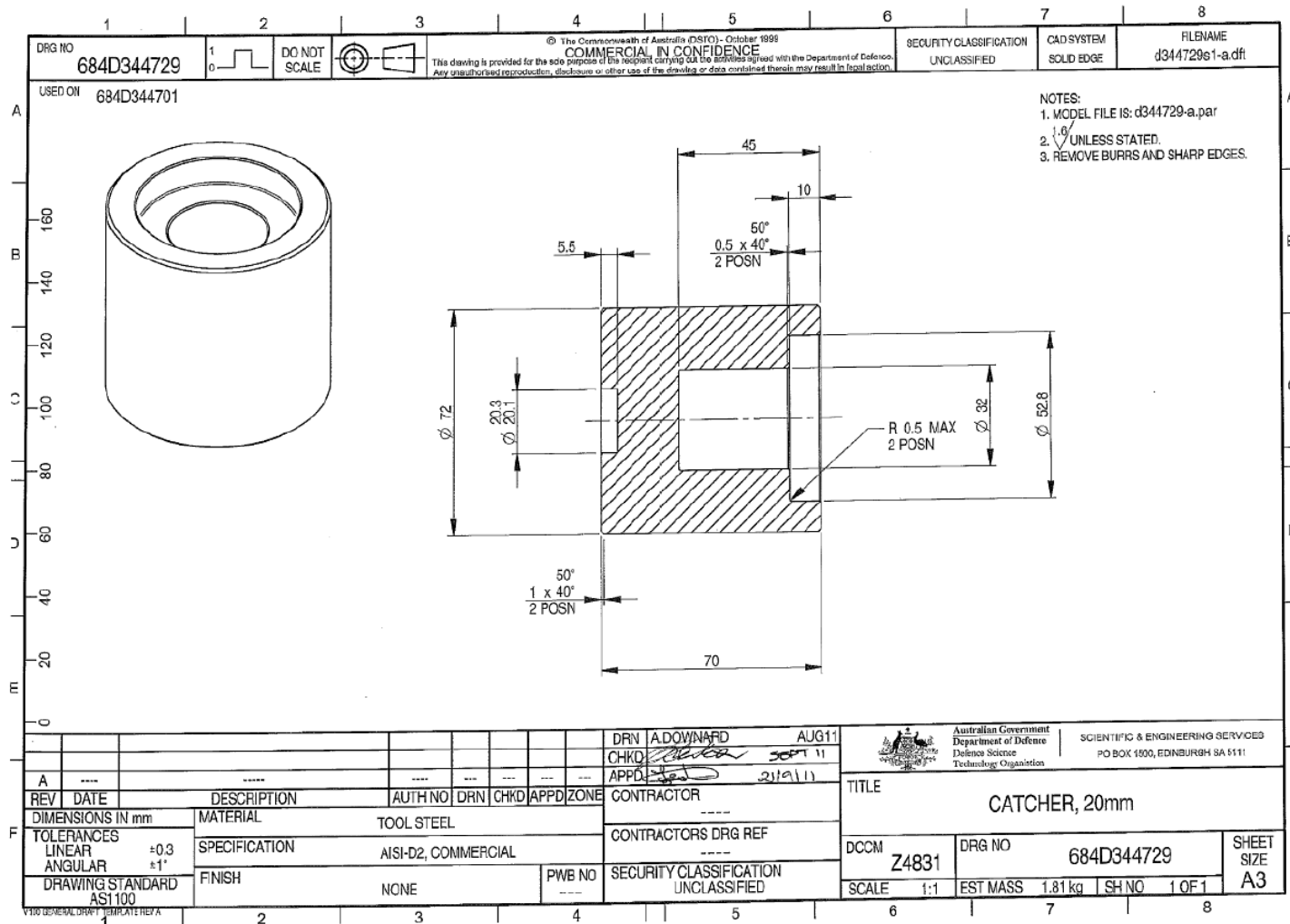


Figure A.4: 20 mm catcher engineering drawing

UNCLASSIFIED

UNCLASSIFIED

DST-Group-TR-3291

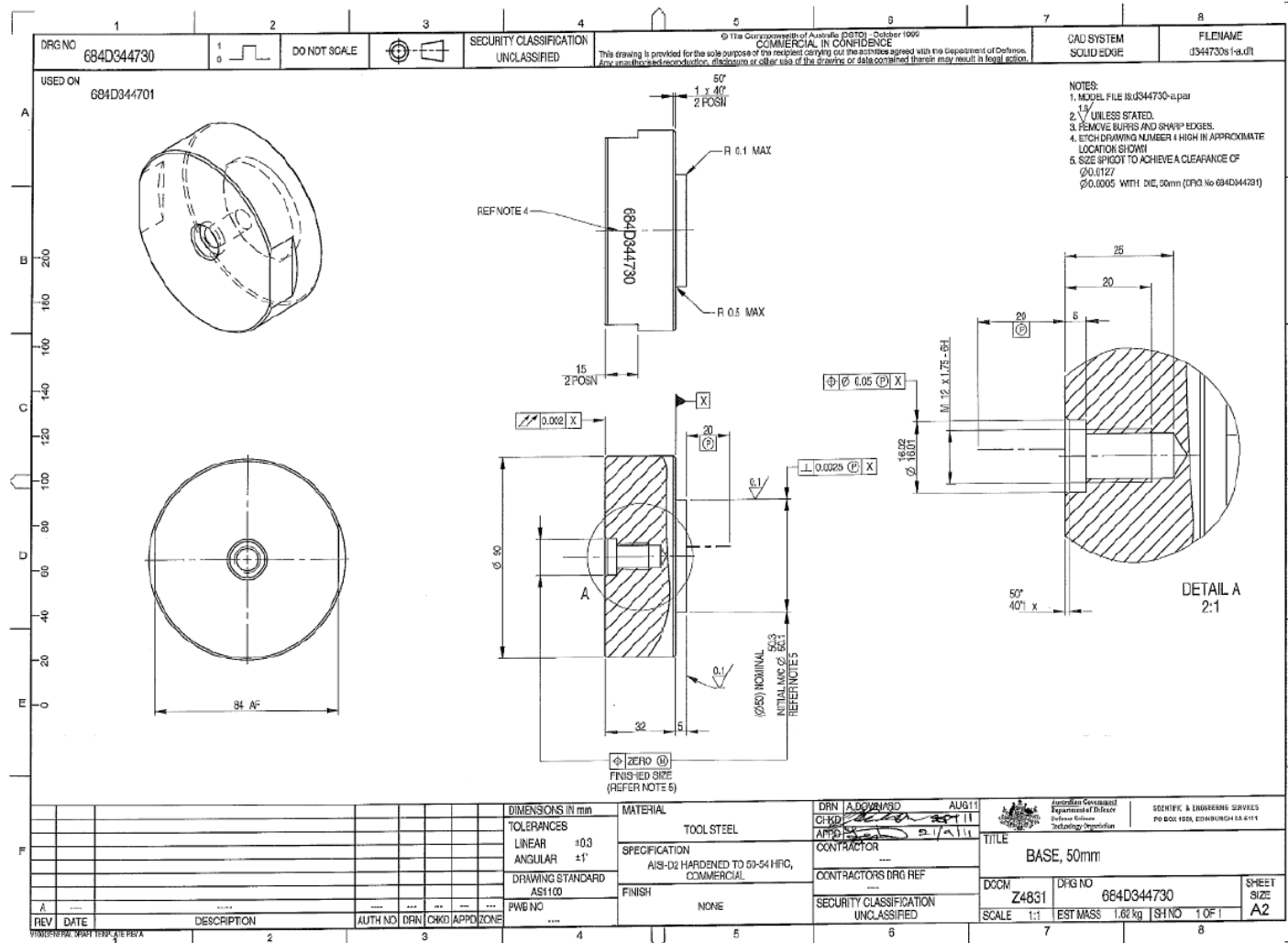


Figure A.5: 50 mm base engineering drawing

UNCLASSIFIED

UNCLASSIFIED

DST-Group-TR-3291

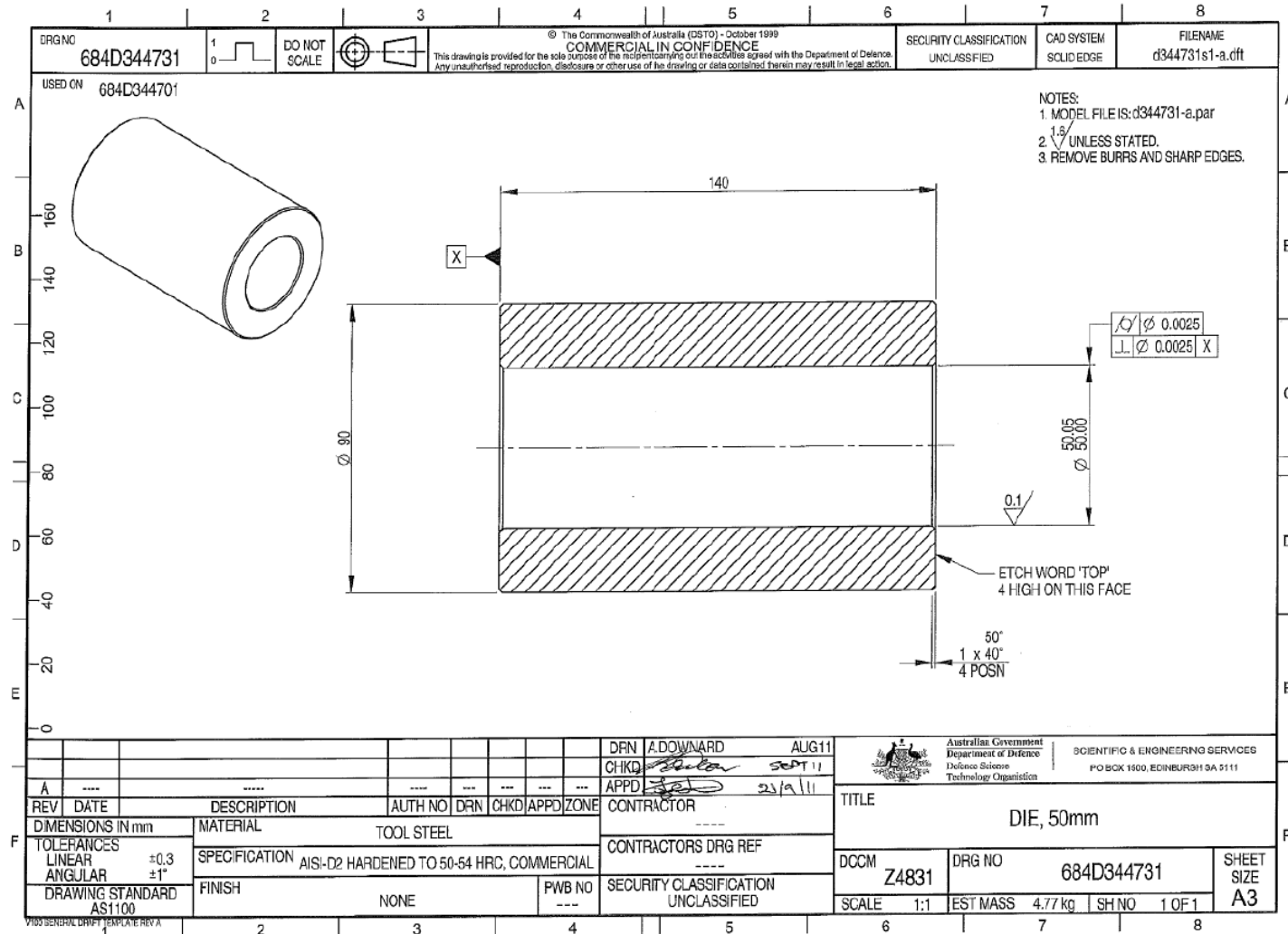


Figure A.6: 50 mm die engineering drawing

UNCLASSIFIED

UNCLASSIFIED

DST-Group-TR-3291

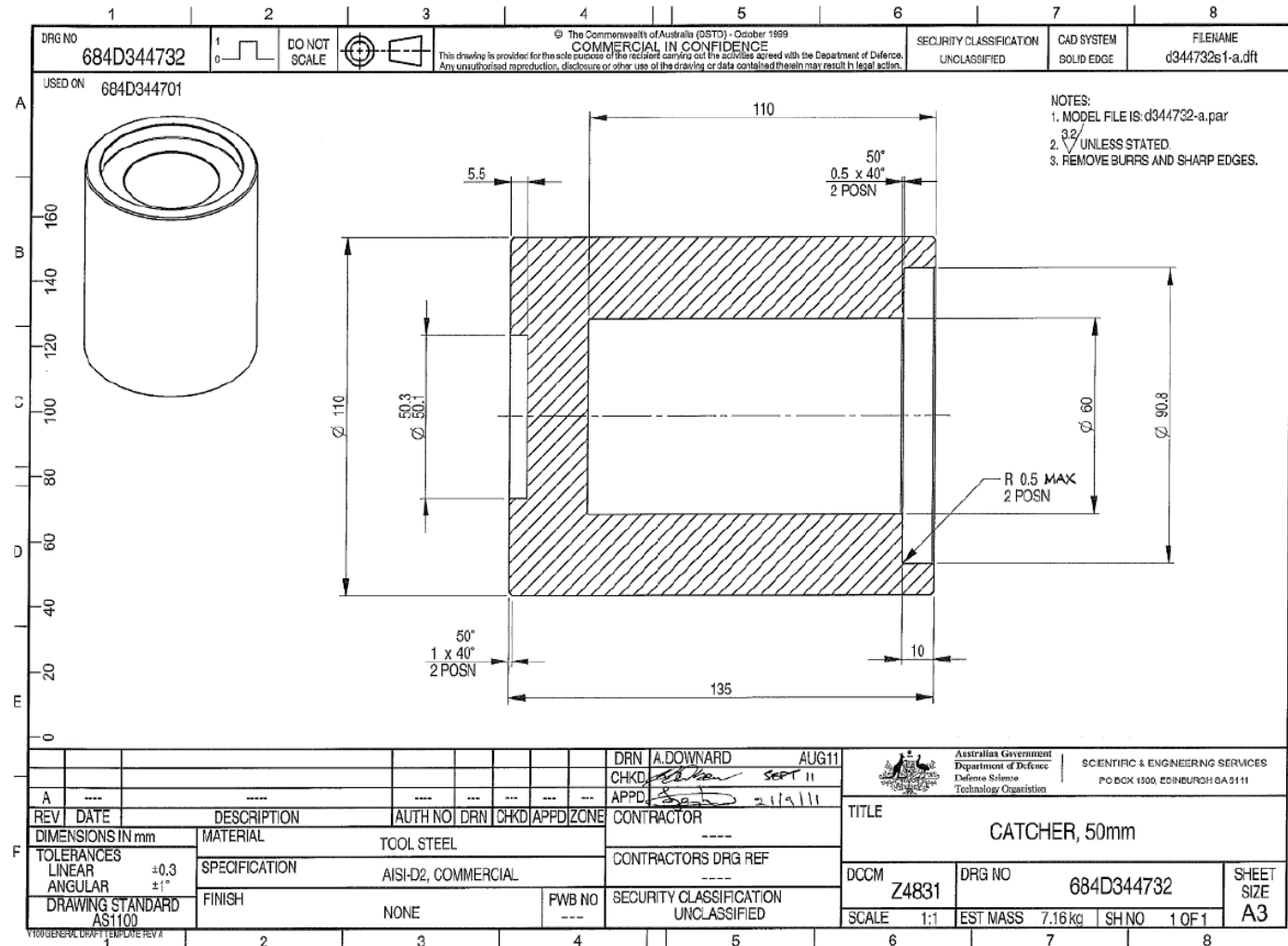


Figure A.8: 50 mm catcher engineering drawing

UNCLASSIFIED

Appendix B Adiabatic Compression Calculations

A basic model was developed to estimate propellant surface temperature increases owing to adiabatic compression of voids between and within propellant grains during propellant bed compression.

The model was represented as a spherical air bubble fully encapsulated by a solid propellant and the following assumptions were employed:

- The air in the bubble behaves as an ideal gas;
- The compression of the air bubble occurs adiabatically;
- The number of moles of air contained within the bubble remains constant over the compression process; and
- Heat transfer from the air bubble to the propellant is via conduction and free convection. Radiative heat transfer is considered negligible given that both nitrogen and oxygen are essentially transparent so do not radiate to any appreciable extent.

The degree to which the air bubble is compressed is dictated by the level of piston displacement over the course of the compression event. The rate of compression is dictated by the applied cross-head speed, in-line with the desired test strain rate.

For the purposes of the model, the compression of the propellant bed (and therefore the air bubble) was represented as a series of step changes in the die volume, with the numerical analysis procedure used to determine transient heat flows applied to each of these step changes.

Governing Equations:

$$(\rho C_p)_{prop} \frac{\partial T}{\partial t} = k_{prop} \frac{\partial^2 T}{\partial x^2} \quad (B.1)$$

The following boundary conditions are employed:

At the propellant surface, $x = 0$, $t > 0$:

$$-k_{prop} \frac{\partial T}{\partial x} = q''(t) \quad (B.2)$$

The propellant was modelled as a cylinder with a 10 mm wall thickness around the spherical air bubble. The propellant temperature at the periphery of the propellant was set at 20°C to represent the die wall temperature under ambient testing conditions, i.e. at $x = L$, $t > 0$:

$$T_{prop, x=L} = T_{die} = 20^\circ C \quad (B.3)$$

In equations (B.1) and (B.2), ρ , C_p and k are the relevant thermophysical properties of the propellant. These properties were assumed constant and were taken from the single base propellant thermophysical properties reported in [61,62]. T is the temperature of the propellant at a distance x from the air bubble/propellant interface and the incident heat flux from the air bubble onto the propellant surface is denoted q'' , where:

$$q''(t) = h(T_{air\ bubble} - T_{prop,x=0}) \quad (B.4)$$

In equation (B.4), h is the convective heat transfer co-efficient evaluated using the Nusselt number for free convection:

$$h = \frac{k_{air\ bubble}}{r_{air\ bubble}} \quad (B.5)$$

The thermal conductivity of air was calculated for each time step as a function of temperature and pressure using the empirical correlation of [63].

Equation (B.1) was solved with respect to propellant temperature by applying a centred finite difference method to the second derivative term, and a forward finite difference method to the first derivative. A centred finite difference method was applied to the boundary condition of equation (B.2). The resultant expressions for the internal nodes and exposed surface are presented in equations (B.6) and (B.7) respectively.

$$T_i^{l+1} = Fo(T_{i+1}^l + T_{i-1}^l) + T_i^l(1 - 2Fo) \quad (B.6)$$

$$T_0^{l+1} = T_0^l + 2Fo \left(\frac{q'' \Delta x}{k_{prop}} + T_1^l - T_0^l \right) \quad (B.7)$$

where:

i = distance step

l = time step

and the Fourier number, $Fo = \frac{k_{prop} \Delta t}{(\rho C_p)_{prop} \Delta x^2}$ (B.8)

To ensure solution stability with equations (B.6) and (B.7), the number of spatial nodes was set such that $Fo = 0.2$.

After a step change in compression, the air bubble will initially attain a new level of internal energy, commensurate with the temperature and pressure changes it has undergone (see equations B.9 - B.11). At this given compression level, the heat flux to the propellant surface will change with time as the air bubble transfers heat to the propellant surface. To more accurately capture the transient heat flux, and associated changes in air bubble and propellant surface temperature, each time increment over which the step

change in compression was applied was sub-divided and the relevant parameters determined after each of these time steps. For example, for the small diameter fixture, a compression rate of 40 mm/min equates to a strain rate of 0.02 s⁻¹ and typical durations for the compression phase of the experiments are 15 s. In the model, step changes in compression level were applied at 0.1 s intervals, with this time scale then sub-divided into 0.002 s increments for the heat transfer calculations.

Using the adiabatic compression assumption, the air bubble temperature, pressure and internal energy are given by:

$$T_{air\ bubble, f} = T_{air\ bubble, o} \left(\frac{V_{air\ bubble, o}}{V_{air\ bubble, f}} \right)^{\gamma-1} \quad (B.9)$$

$$P_{air\ bubble, f} = \frac{nRT_{air\ bubble, f}}{V_{air\ bubble, f}} \quad (B.10)$$

$$U = m_{air\ bubble} C_{P\ air} T_{air\ bubble} \quad (B.11)$$

In equations (B.9) – (B.10), subscripts *o* and *f* refer to the initial and final conditions over that sub-iteration. For a given set of sub-iterations, the volume ratio is held constant until the next step change in compression level.

The energy lost from the air bubble over each sub-iteration, calculated using equation (B.12), is used to calculate the ‘new’ air bubble internal energy which then sets the starting air bubble temperature and pressure for the next sub-iteration until it is time to apply the next step change in compression level.

$$\Delta U = q''(t) A_{air\ bubble} t_s \quad (B.12)$$

where:

$A_{air\ bubble}$ is the surface area of the air bubble at the relevant compression level; and

t_s is the sub-iteration time-step.

Results from the modelling are provided in Figure B.1 and Figure B.2 for the large and small diameter dies respectively. A range of conditions were modelled, for the large diameter fixture:

- Air bubble radii corresponding to: realistic enclosed void volumes based on propellant grain form considerations (0.6 mm radius); and, a larger, less realistic bubble volume to assess model sensitivity (2.5 mm radius).

- Rate of compression corresponding to the strain rate (0.02 s^{-1}) used in experiments, 100 mm/min; and, a compression rate one order of magnitude higher to assess model sensitivity, 1000 mm/min.

Using the same rationale, for the small diameter fixture the bubble radii modelled were 0.5 and 1.0 mm with compression rates of 40 and 400 mm/min.

Depending on the propellant nature and test temperature, compression ratios (ratio of final volume occupied by the propellant to the initial volume) typically ranged between 1.3 - 1.8.

Given the ignition temperature for propellants of this type is of the order of 160°C , the results show that, in all cases modelled, the propellant surface temperature increase is inconsequential when compared with the temperature increase necessary to induce a potential ignition risk.

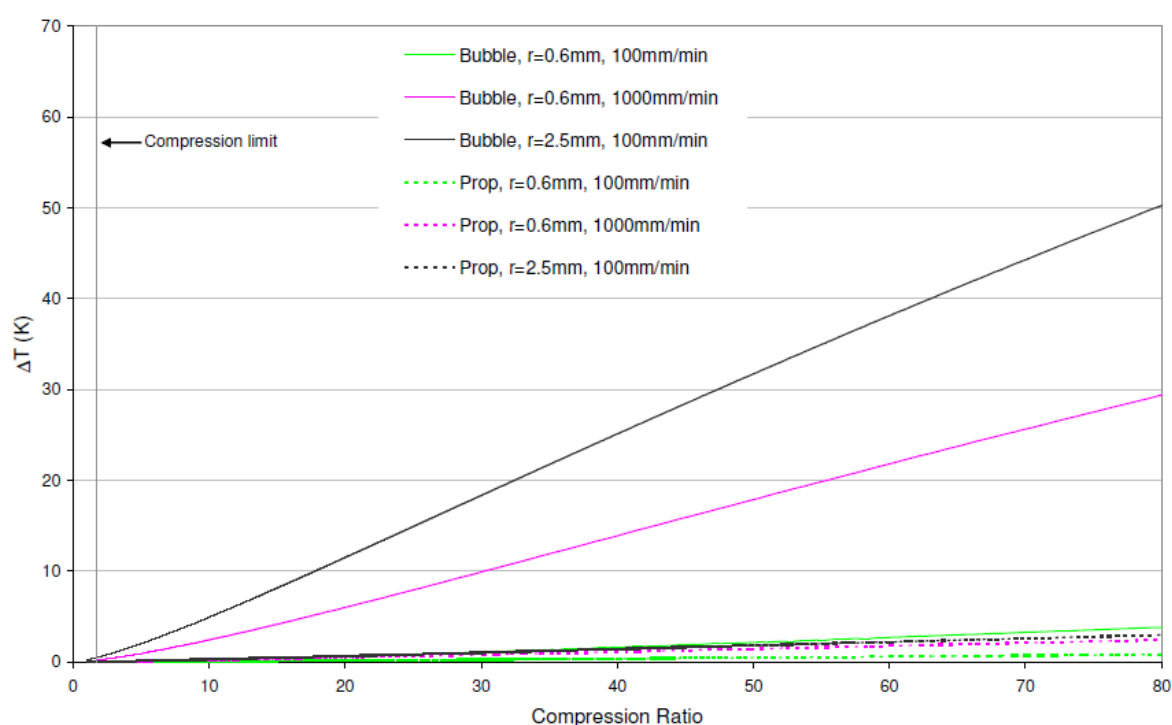


Figure B.1: Change in air bubble and propellant surface temperature as a function of compression ratio for a range of void sizes and compression rates. Large diameter test fixture.

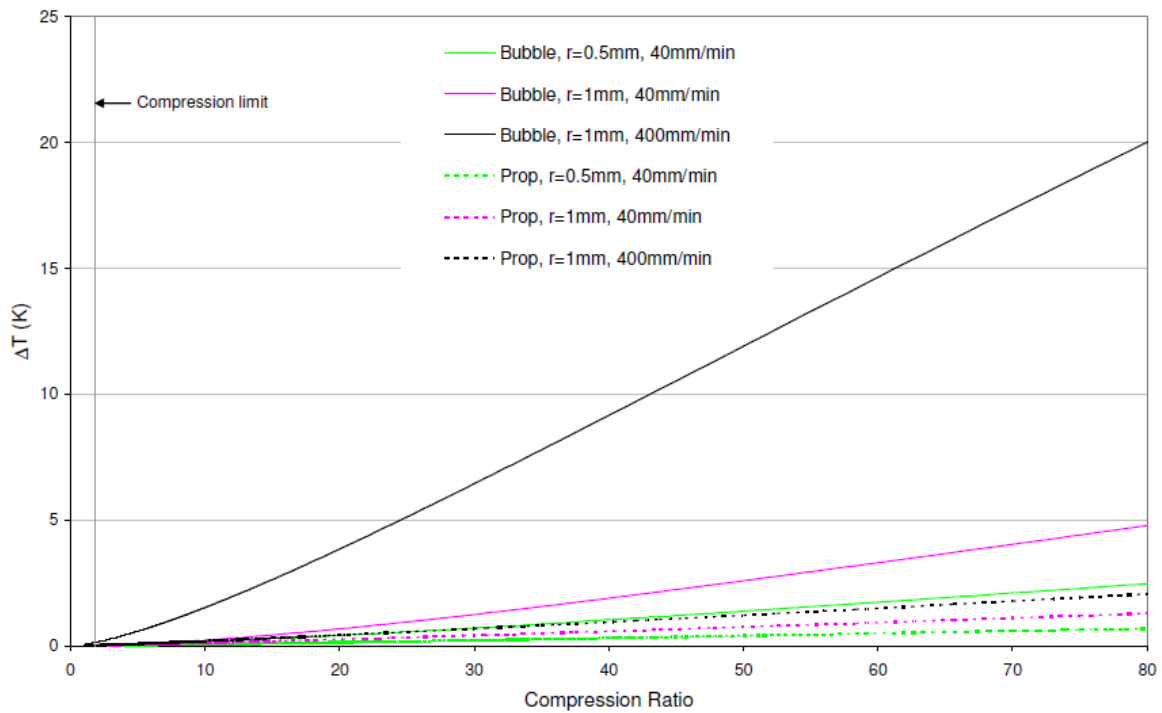


Figure B.2: Change in air bubble and propellant surface temperature as a function of compression ratio for a range of void sizes and compression rates. Small diameter test fixture.

Appendix C Propellant Visual Inspection

C.1 AR2211



Figure C1.1: AR2211 exemplar grains post-compaction testing at ambient: A) side view; and B) top view.

In Figure C.1.2 and C.1.3, the presented categories, e.g. SA100, SA105, SA115, correspond to grains having nominally 100% of pre-crushing surface area (SA), 105% and 115%. These categories were defined following analysis of the FNH-025 samples crushed at -40°C , particularly the microscopy shown in Figure C.3.3. Modelling these exemplar grains using geometrical surfaces for fracture surfaces, a rough link between degree of fracture (for each grain, from visual inspection) and percentage increase in SA was determined. The criteria thus developed were used both to calculate an approximate increase in SA for the FNH-025 sample (including the SA of the fragments shown in Figure C.3.2) for comparison with closed vessel-derived DISA values, as well as to guide the categorisation of the AR2211 samples shown in Figures C.1.2 and C.1.3. For these samples a microscope was used to examine the grains, as the graphite coating and small grain size obscured evidence of fracture. This was identified as a problem when examining AR2220 samples, as microscopy often revealed fracture that was not visible using the naked eye, even when using an illuminated magnifier. However, deriving SA increases using this method was deemed unfeasible due to the inherent level of uncertainty involved and the time that would be required to undertake such an analysis on a routine basis.



Figure C1.2: Exemplar AR2211 grains compacted at -40°C: A) SA100; B) SA105; C) SA115; D) SA125; and E) SA135 categories.



Figure C1.3: Exemplar AR2211 grains compacted at -60°C: A) SA100; B) SA105; C) SA115; D) SA125; E) SA135; and F) SA155 categories.

C.2 AR2220

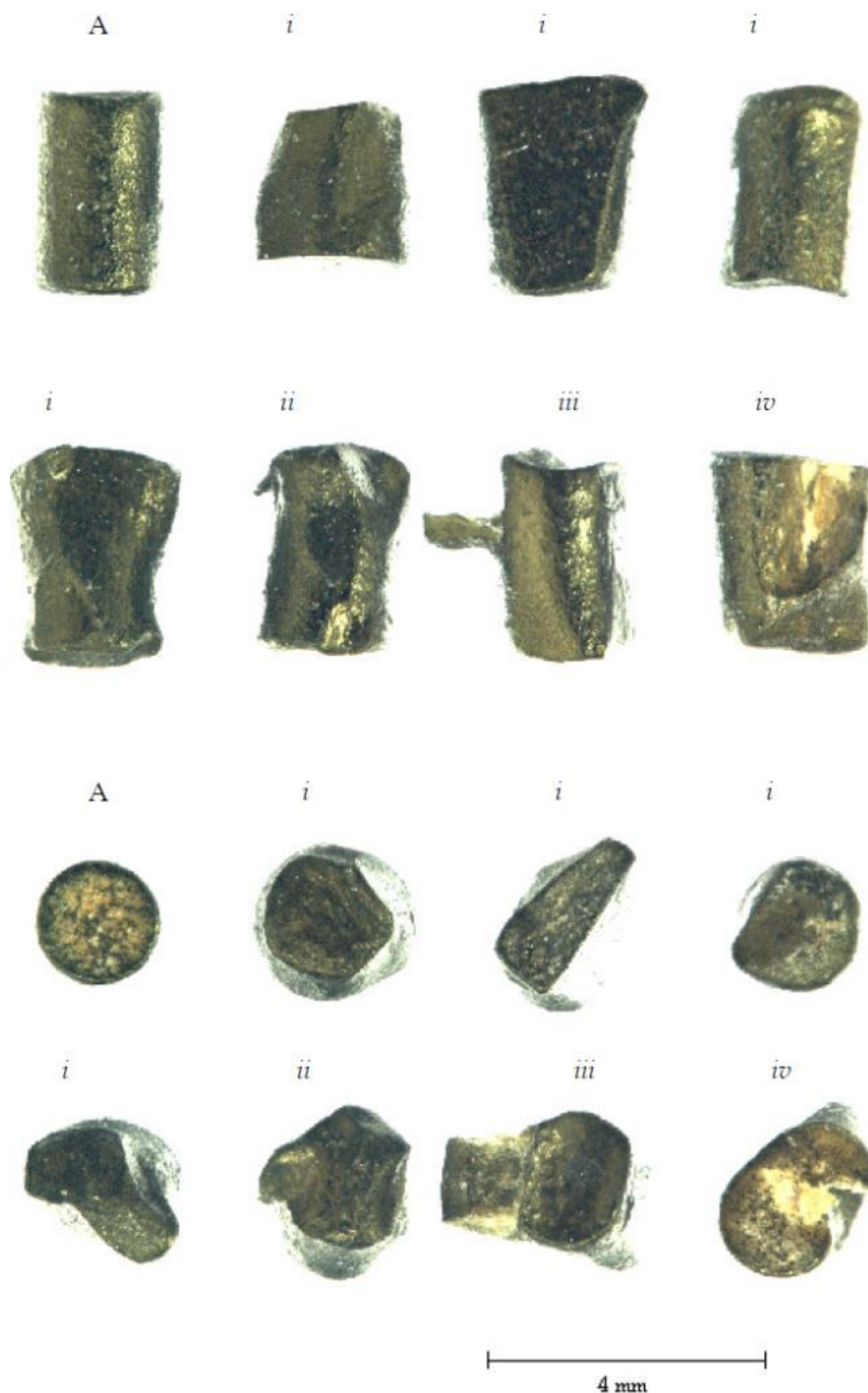


Figure C2.1: AR2220 exemplar grains post-compaction testing at ambient: A) uncrushed; i) no visible fracture; ii) web and surface fracture only; iii) fracture up to $\frac{1}{4}$ grain length; and iv) fracture up to $\frac{1}{2}$ grain length.

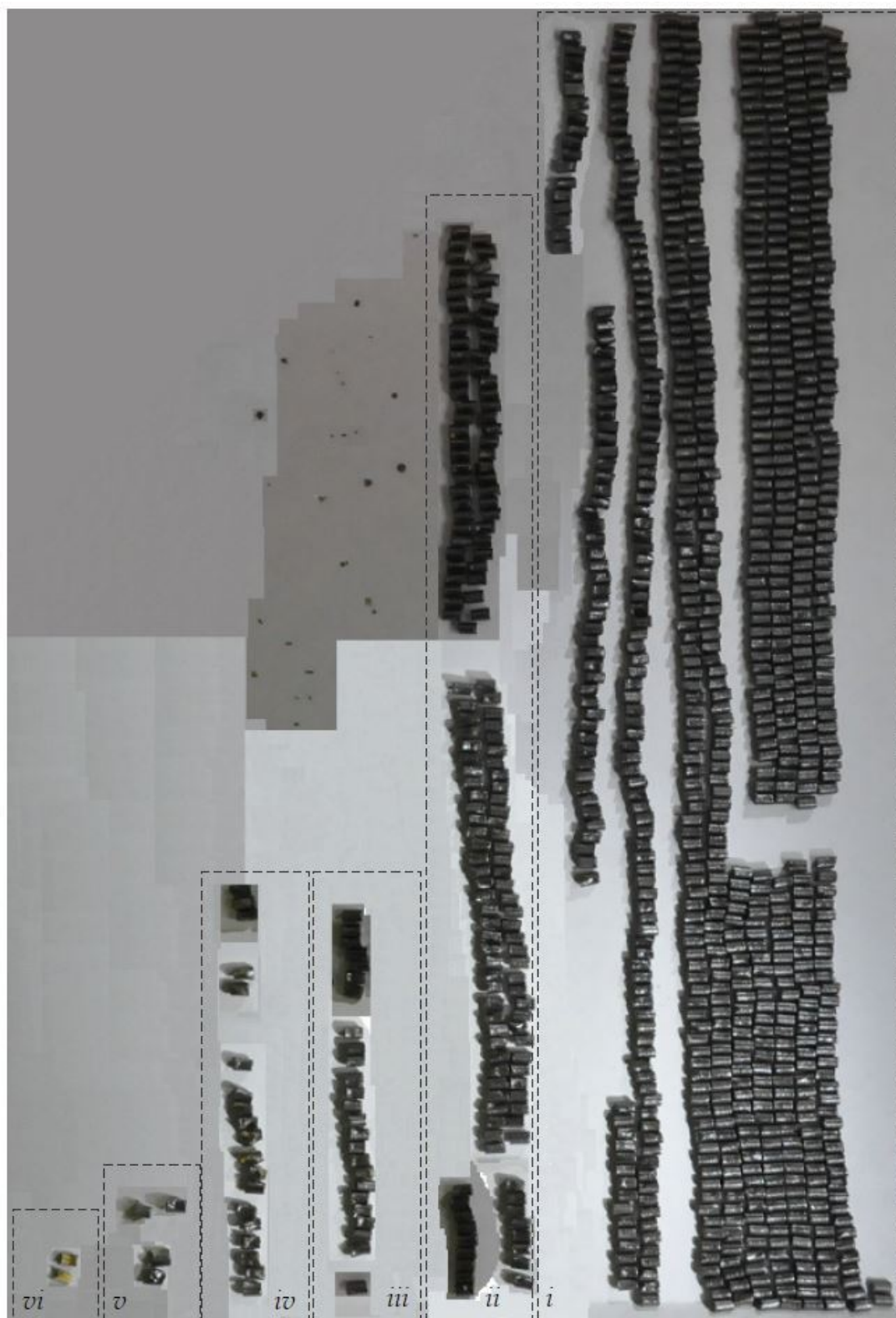


Figure C2.2: AR2220 bed post-compaction testing at -40°C : i) no visible fracture; ii) web and surface fracture only; iii) fracture up to $\frac{1}{4}$ grain length; iv) fracture up to $\frac{1}{2}$ grain length; v) fracture up to full grain length; and vi) grain shivered.



Figure C2.3: Exemplar AR2220 grains post-compaction at a -40°C test condition: i) no visible fracture; ii) web and surface fracture only; iii) fracture up to $\frac{1}{4}$ grain length; iv) fracture up to $\frac{1}{2}$ grain length; v) fracture up to full grain length; and vi) grain shivered.

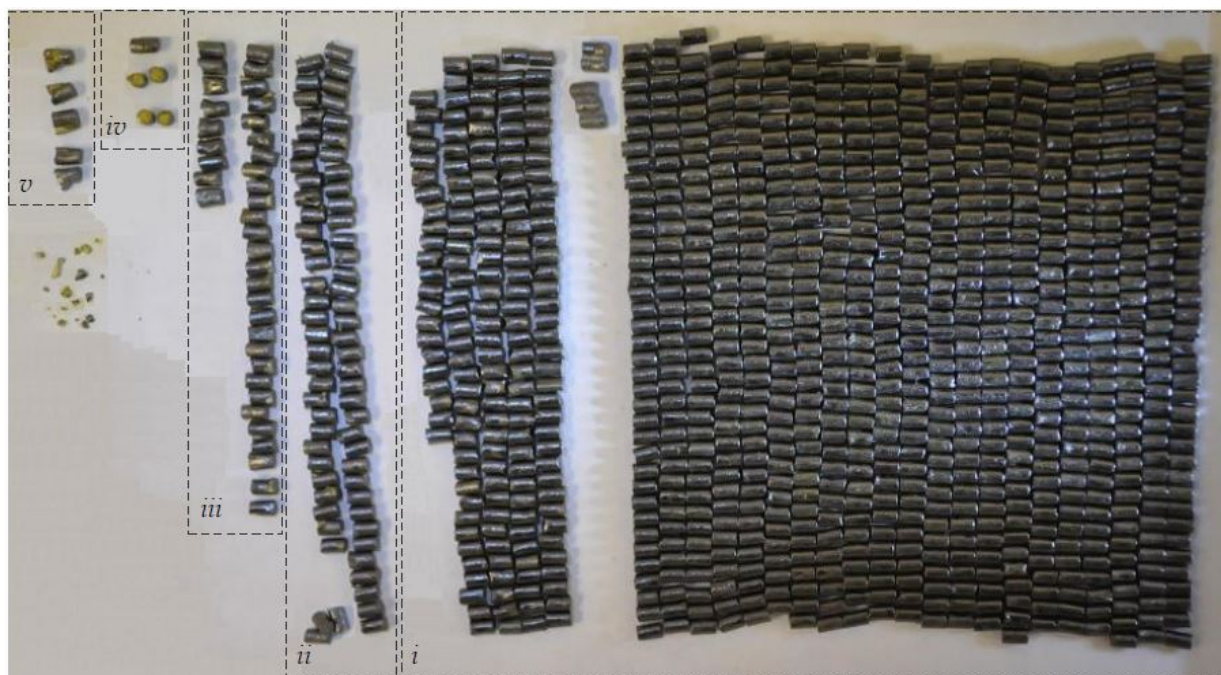


Figure C2.4: AR2220 bed post-compaction at a -60°C test condition: i) no visible fracture; ii) web and surface fracture only; iii) fracture up to $\frac{1}{4}$ grain length; iv) fracture up to $\frac{1}{2}$ grain length; and v) fracture up to full grain length.

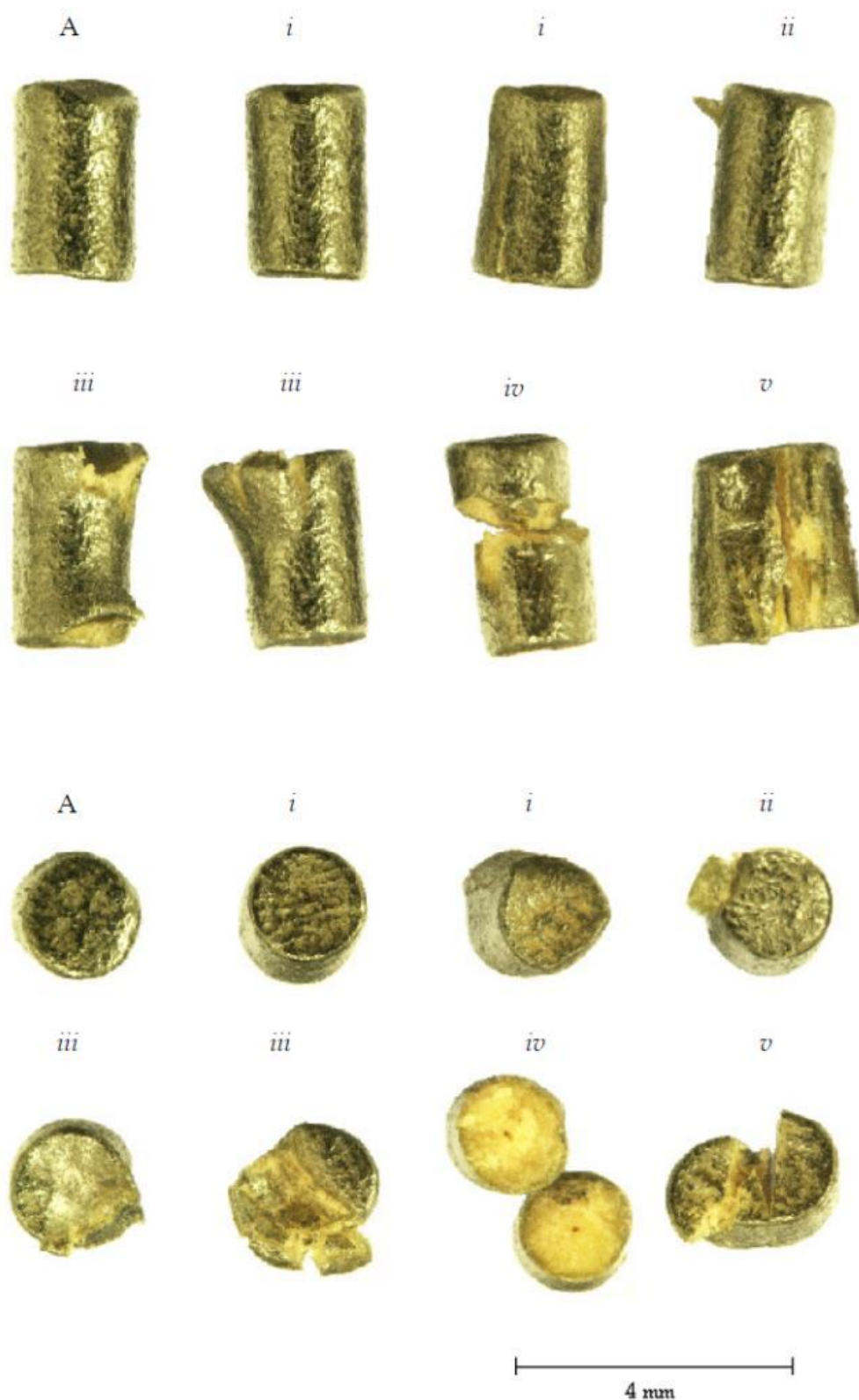


Figure C2.5: Exemplar AR2220 grains post-compaction at a -60°C test condition: A) uncrushed; i) no visible fracture; ii) web and surface fracture only; iii) fracture up to $\frac{1}{4}$ grain length; iv) fracture up to $\frac{1}{2}$ grain length; and v) fracture up to full grain length.



Figure C2.6: AR2220, aged for 42 days at 70°C, bed compaction at -60°C: i) no visible fracture; ii) web and surface fracture only; iii) fracture up to $\frac{1}{4}$ grain length; iv) fracture up to $\frac{1}{2}$ grain length; v) fracture up to full grain length; and vi) grain pulverised.



Figure C2.7: AR2220, aged for 86 days at 70°C, bed compaction at -60°C: i) no visible fracture; ii) web and surface fracture only; iii) fracture up to $\frac{1}{4}$ grain length; iv) fracture up to $\frac{1}{2}$ grain length; v) fracture up to full grain length; vi) grain shivered; and vii) grain pulverised.

C.3 FNH-025

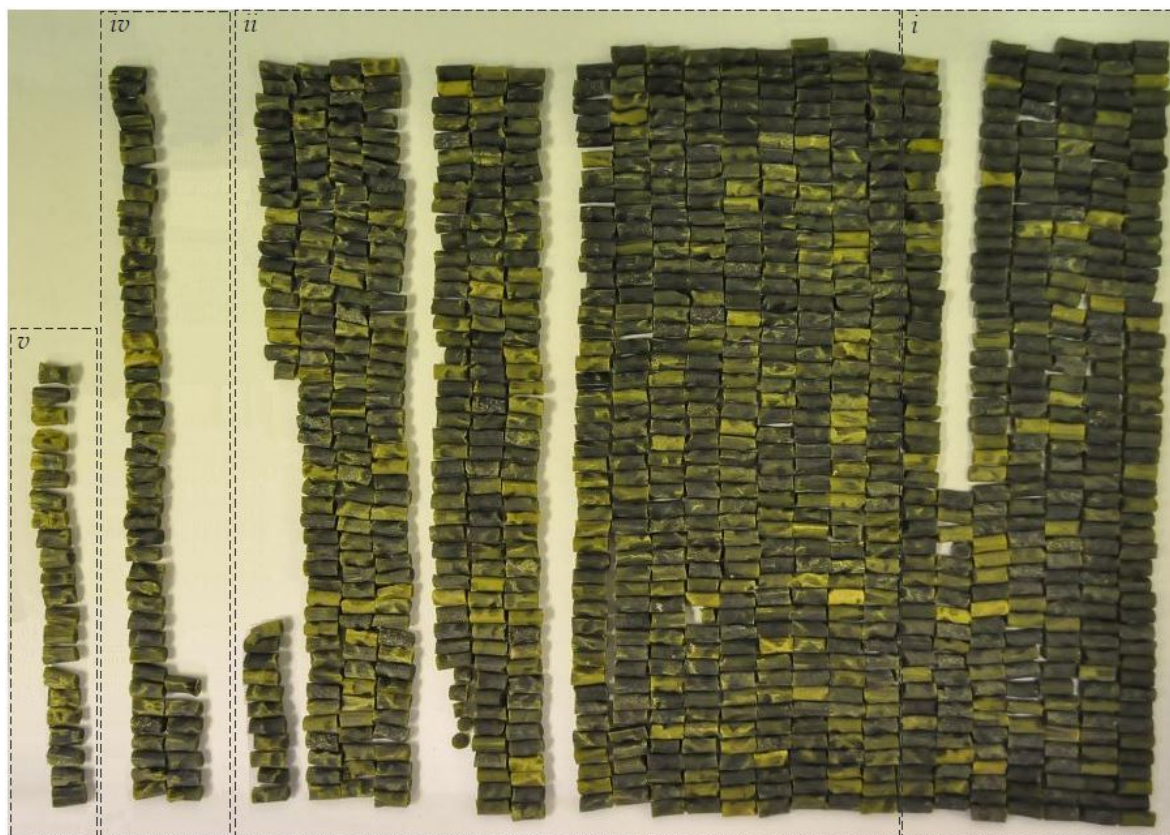


Figure C3.1: FNH-025 bed post-compaction at ambient test conditions: i) no visible fracture; ii) web and surface fracture only; iii) fracture up to $\frac{1}{4}$ grain length; iv) fracture up to $\frac{1}{2}$ grain length; and v) fracture up to full grain length.

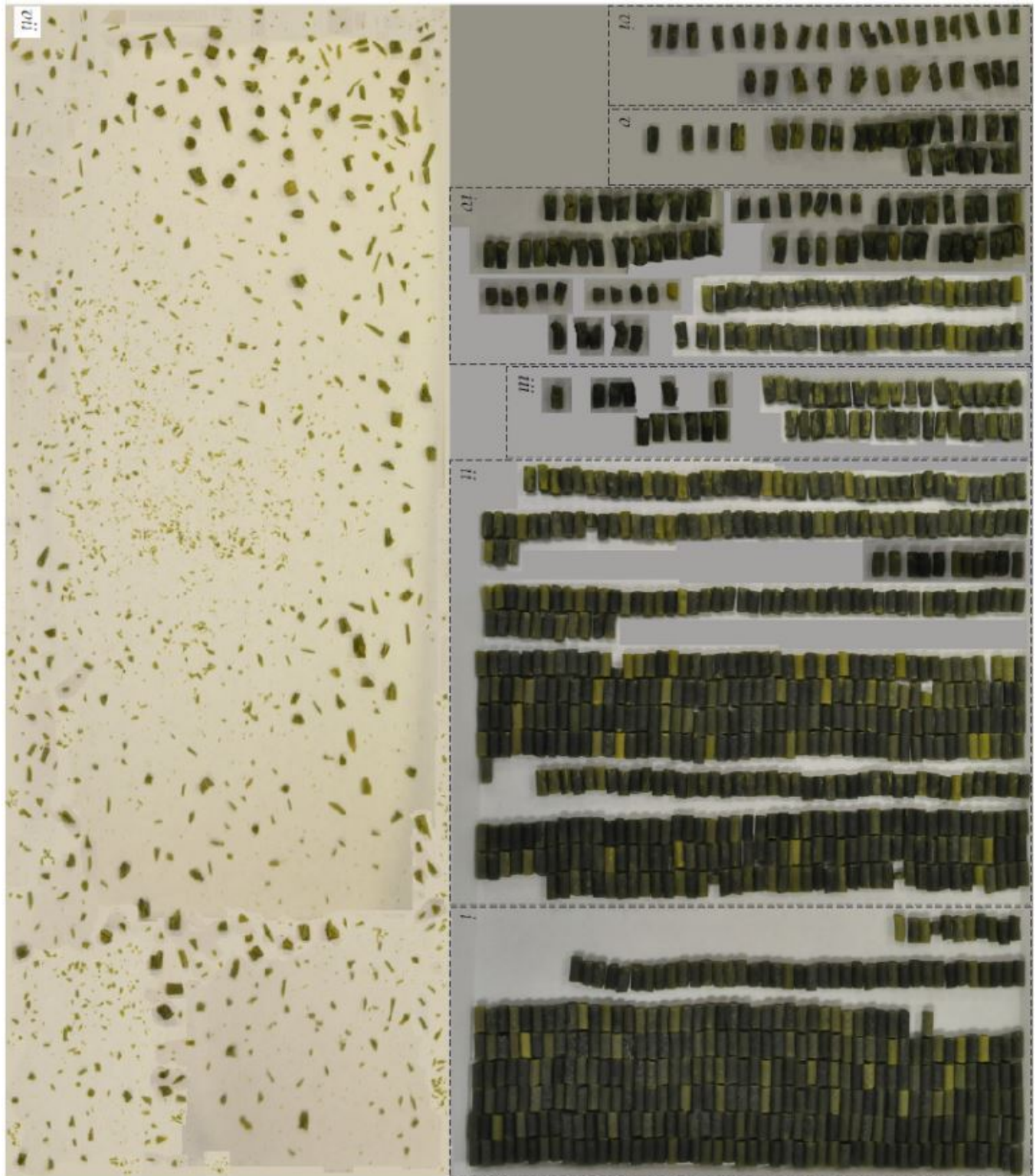


Figure C3.2: FNH-025 bed post-compaction at a -40°C test condition: i) no visible fracture; ii) web and surface fracture only; iii) fracture up to $\frac{1}{4}$ grain length; iv) fracture up to $\frac{1}{2}$ grain length; v) fracture up to full grain length; and vi) grain shivered; and vii) grains pulverised.



Figure C3.3: Exemplar FNH-025 grains post-compaction at a -40°C test condition: i) no visible fracture; ii) web and surface fracture only; iii) fracture up to $\frac{1}{4}$ grain length; iv) fracture up to $\frac{1}{2}$ grain length; v) fracture up to full grain length; and vi) grains shattered.

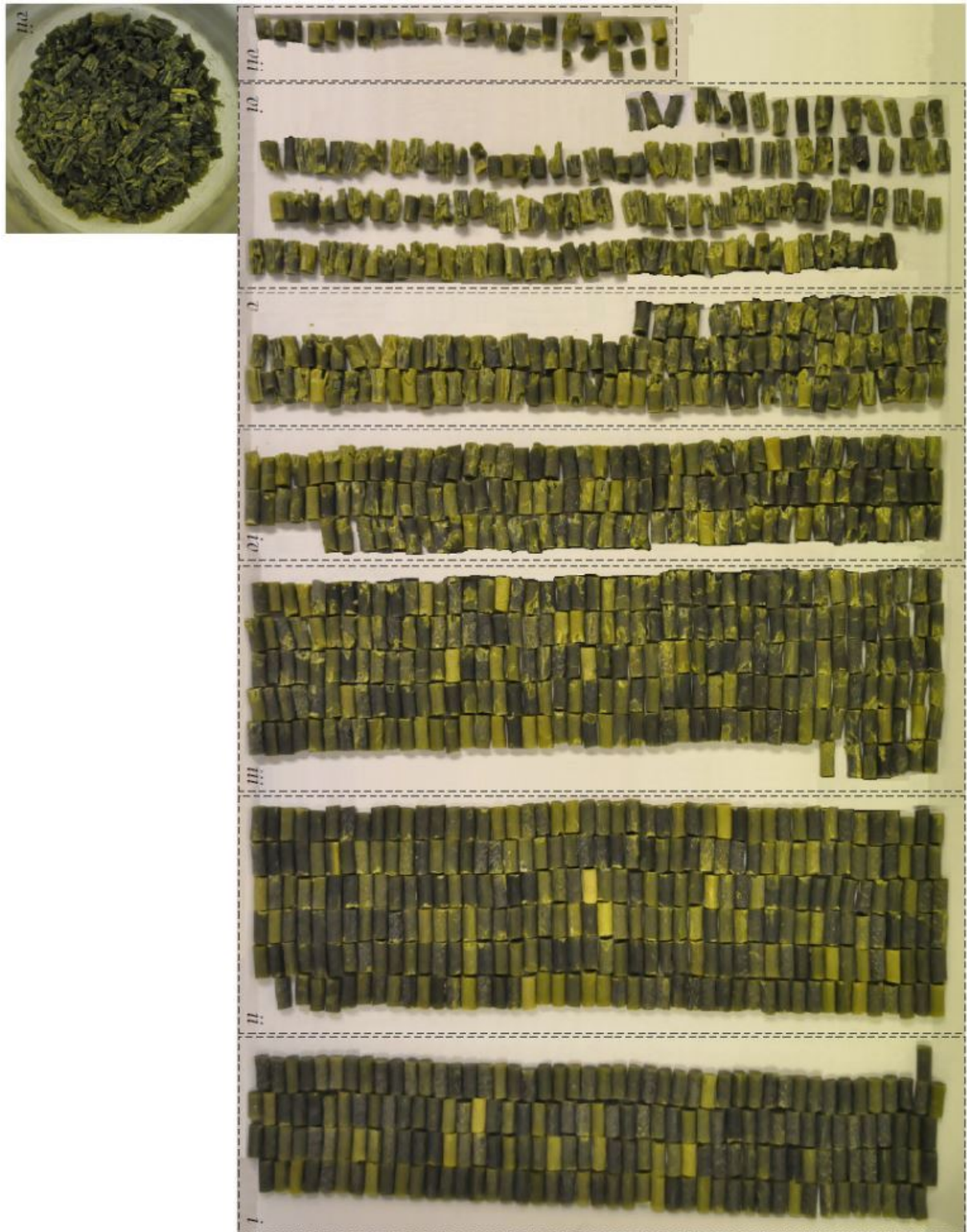


Figure C3.4: FNH-025 bed post-compaction at a -60°C test condition: i) no visible fracture; ii) web and surface fracture only; iii) fracture up to $\frac{1}{4}$ grain length; iv) fracture up to $\frac{1}{2}$ grain length; v) fracture up to full grain length; and vi) grain shivered; and vii) grains pulverised.

C.4 BS-NACO



Figure C4.1: BS-NACO bed post-compaction at an ambient temperature test condition: i) no visible fracture; ii) web and surface fracture only; and iii) fracture up to $\frac{1}{4}$ grain length.

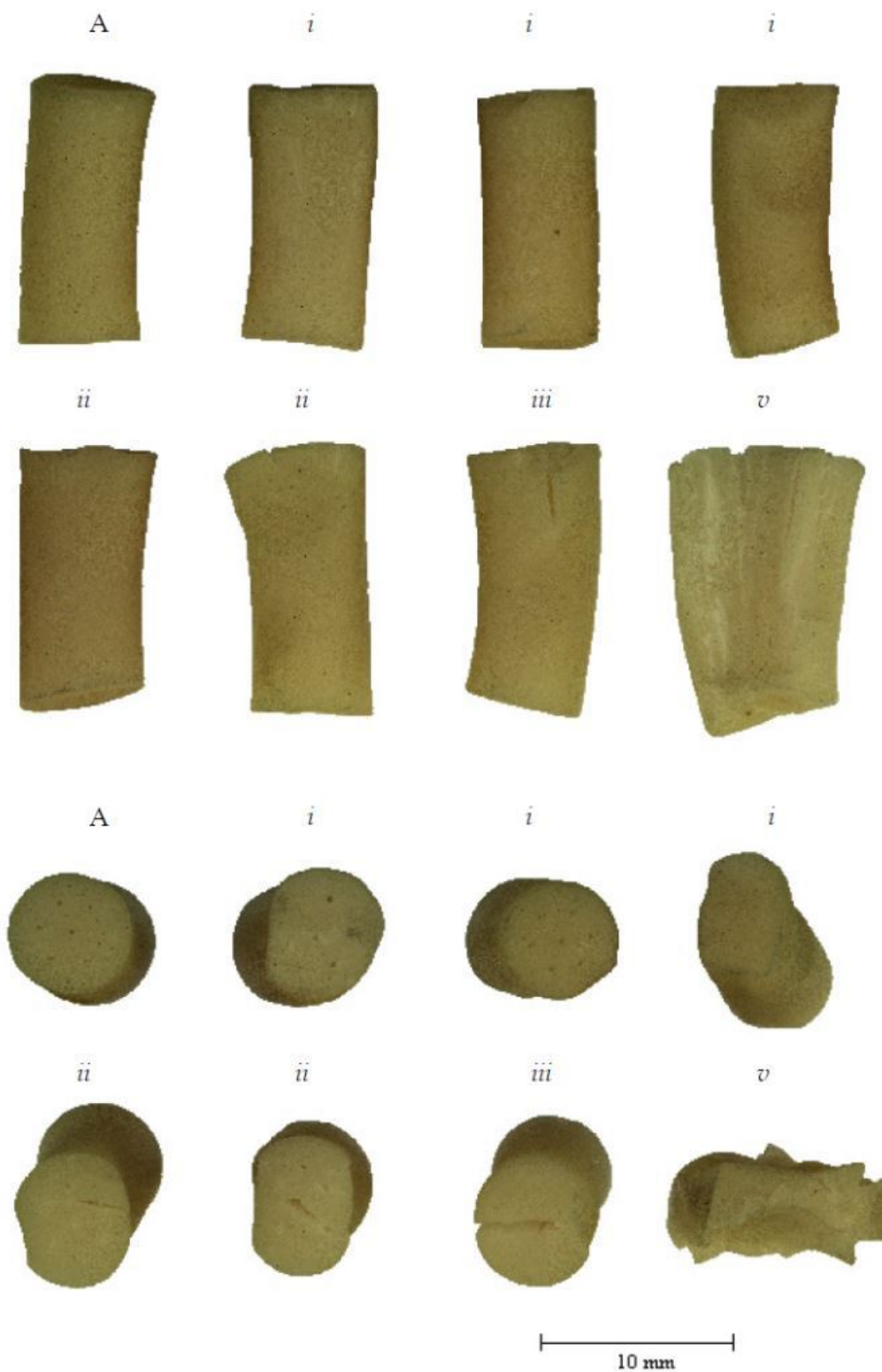


Figure C4.2: Exemplar BS-NACO grains post-compaction at an ambient test temperature condition: A) uncrushed; i) no visible fracture; ii) web and surface fracture only; iii) fracture up to $\frac{1}{4}$ grain length; iv) fracture up to $\frac{1}{2}$ grain length; and v) fracture up to full grain length.



Figure C4.3: BS-NACO bed post-compaction at a -15°C test condition: i) no visible fracture; ii) web and surface fracture only; iii) fracture up to $\frac{1}{4}$ grain length; iv) fracture up to $\frac{1}{2}$ grain length; v) fracture up to full grain length; and vi) grain shivered.

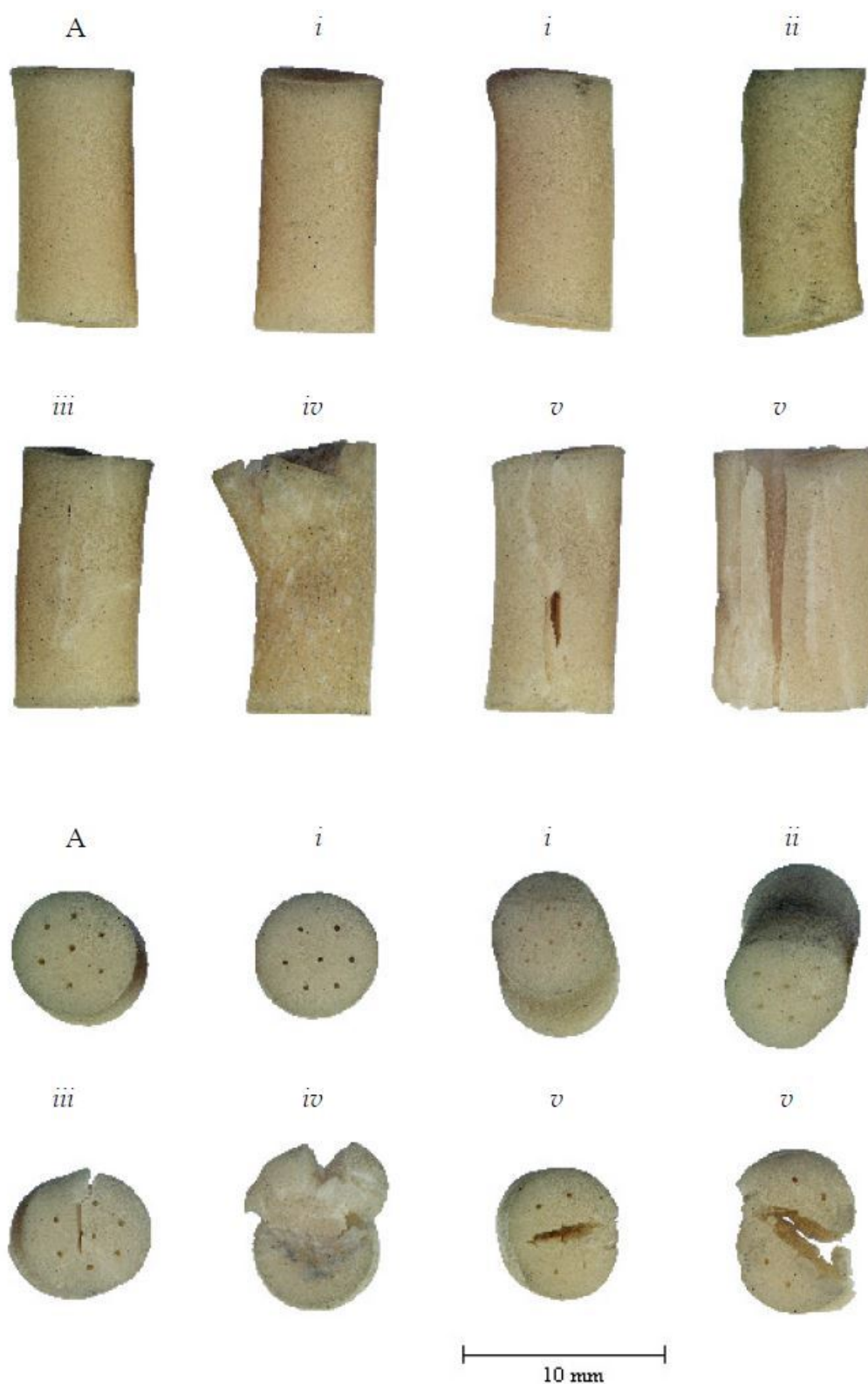


Figure C4.4: Exemplar BS-NACO grains post-compaction at a -15°C test condition: A) uncrushed; i) no visible fracture; ii) web and surface fracture only; iii) fracture up to 1/4 grain length; iv) fracture up to 1/2 grain length; and v) fracture up to full grain length.

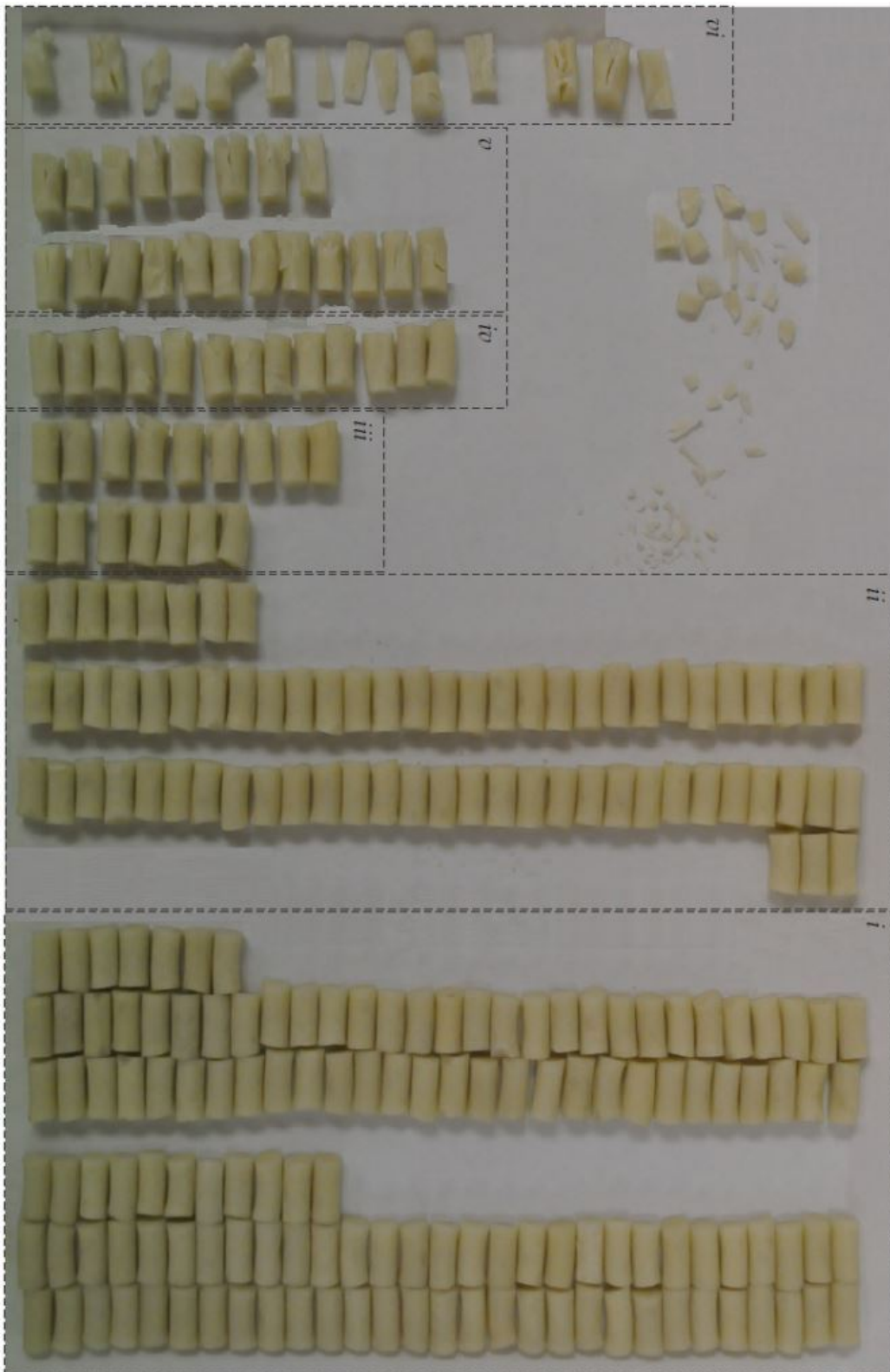


Figure C4.5: BS-NACO bed post-compaction at a -40°C test condition: i) no visible fracture; ii) web and surface fracture only; iii) fracture up to $\frac{1}{4}$ grain length; iv) fracture up to $\frac{1}{2}$ grain length; v) fracture up to full grain length; and vi) grain shivered.

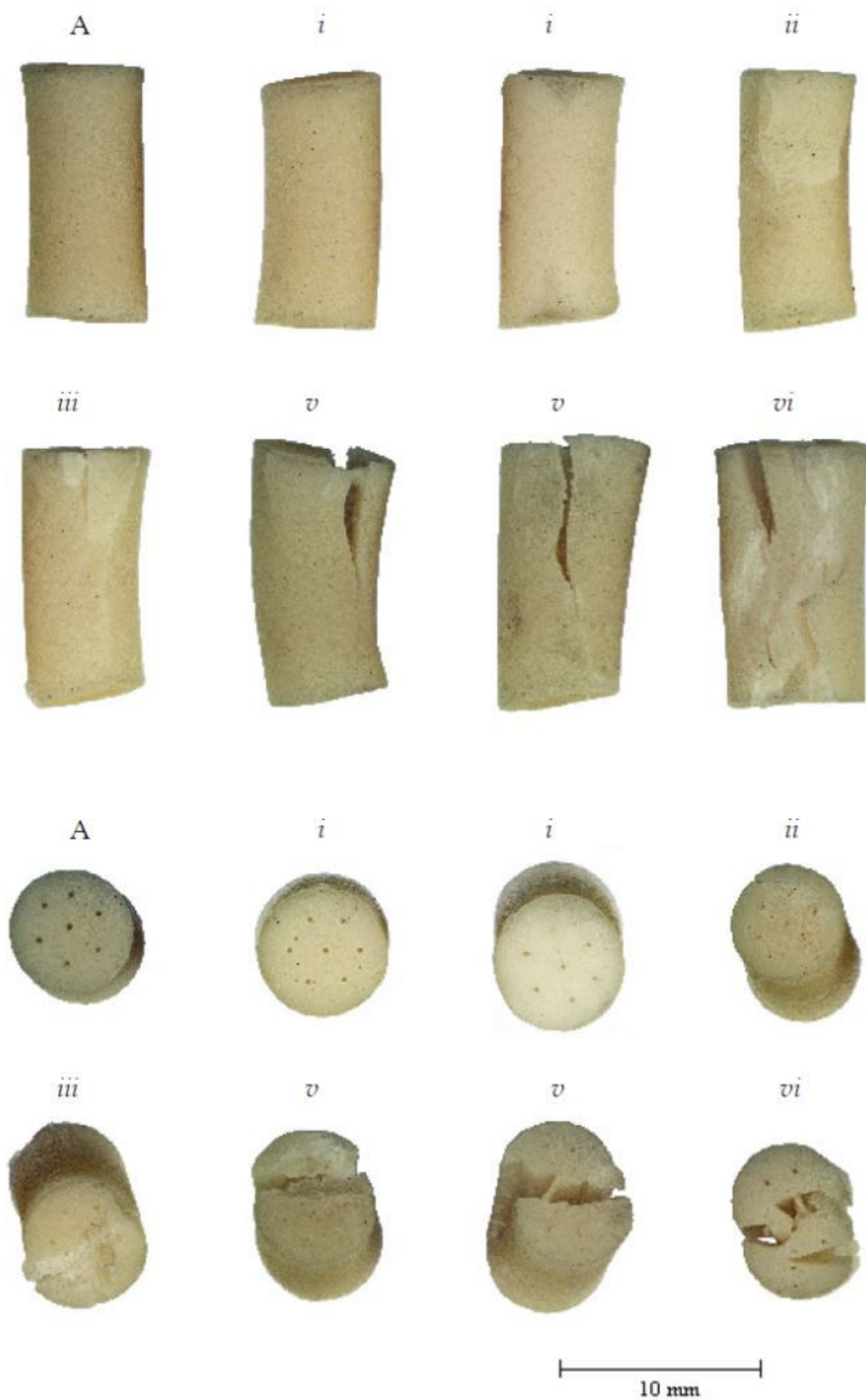


Figure C4.6: Exemplar BS-NACO grains post-compaction at a -40°C test condition: A) uncrushed); i) no visible fracture; ii) web and surface fracture only; iii) fracture up to $\frac{1}{4}$ grain length; iv) fracture up to $\frac{1}{2}$ grain length; v) fracture up to full grain length; and vi) grain shivered.



Figure C4.7: BS-NACO bed post-compaction at a -60°C test condition: i) no visible fracture; ii) web and surface fracture only; iii) fracture up to $\frac{1}{4}$ grain length; iv) fracture up to $\frac{1}{2}$ grain length; v) fracture up to full grain length; and vi) grain shattered.

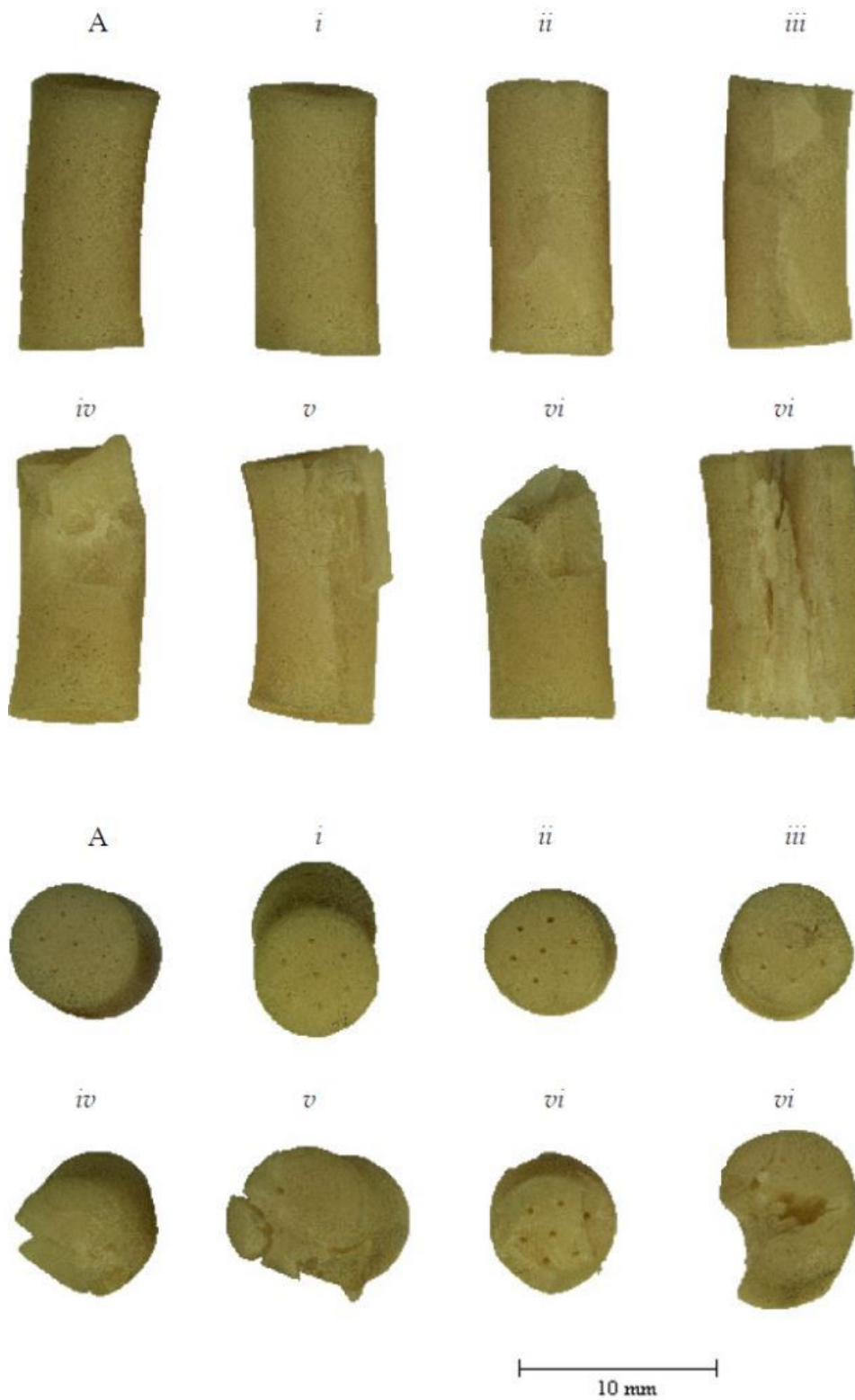


Figure C4.8: Exemplar BS-NACO grains post-compaction at a -60°C test condition: A) uncrushed; i) no visible fracture; ii) web and surface fracture only; iii) fracture up to $\frac{1}{4}$ grain length; iv) fracture up to $\frac{1}{2}$ grain length; v) fracture up to full grain length; and vi) grain shivered.



Figure C4.9: BS-NACO, aged for 67 days at 70°C, bed compaction at -60°C: i) no visible fracture; ii) web and surface fracture only; iii) fracture up to $\frac{1}{4}$ grain length; iv) fracture up to $\frac{1}{2}$ grain length; v) fracture up to full grain length; vi) grain shattered; and vii) grain pulverised.



Figure C4.10: BS-NACO, aged for 40 days at 80°C, bed compaction at -60°C: i) no visible fracture; ii) web and surface fracture only; iii) fracture up to $\frac{1}{4}$ grain length; iv) fracture up to $\frac{1}{2}$ grain length; v) fracture up to full grain length; vi) grain shivered; and vii) grain pulverised.



Figure C4.11: BS-NACO, aged for 60 days at 80°C, bed compaction at -60°C: i) no visible fracture; ii) web and surface fracture only; iii) fracture up to $\frac{1}{4}$ grain length; iv) fracture up to $\frac{1}{2}$ grain length; v) fracture up to full grain length; vi) grain shivered; and vii) grain pulverised.



Figure C4.12: BS-NACO, aged for 80 days at 80°C, bed compaction at -60°C: i) no visible fracture; ii) web and surface fracture only; iii) fracture up to $\frac{1}{4}$ grain length; iv) fracture up to $\frac{1}{2}$ grain length; v) fracture up to full grain length; vi) grain shivered; and vii) grain pulverised.

Appendix D Bulk Modulus and Heckel Plots

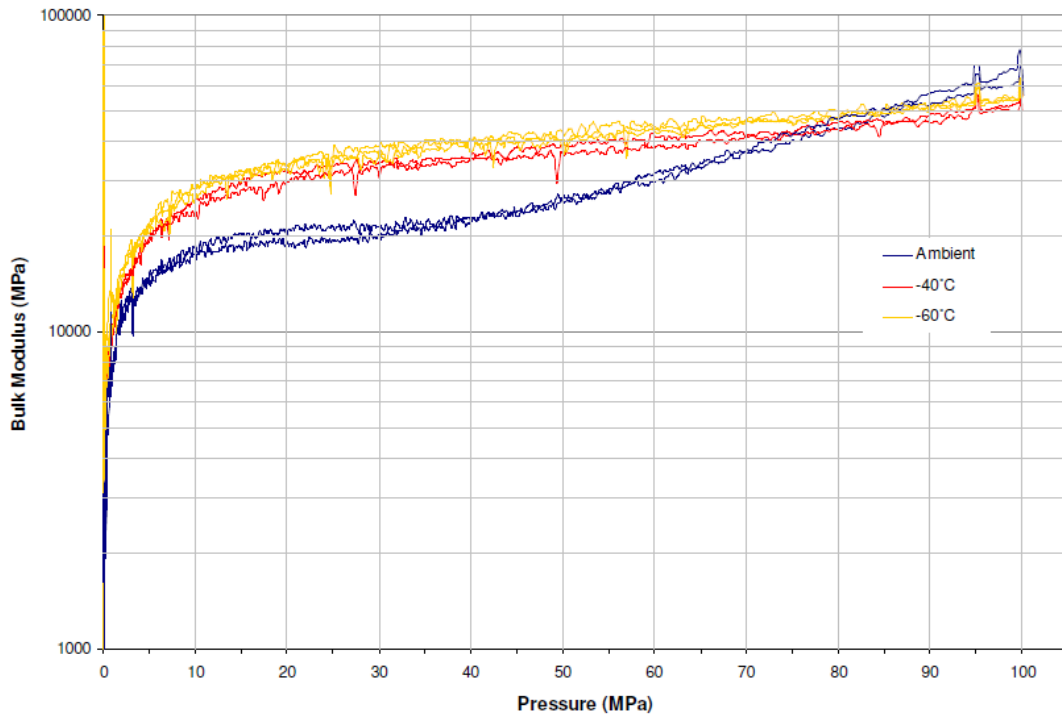


Figure D.1: AR2211 bulk modulus versus pressure results at ambient, -40°C and -60°C testing temperatures. Only results within ± 0.5 initial %TMD plotted.

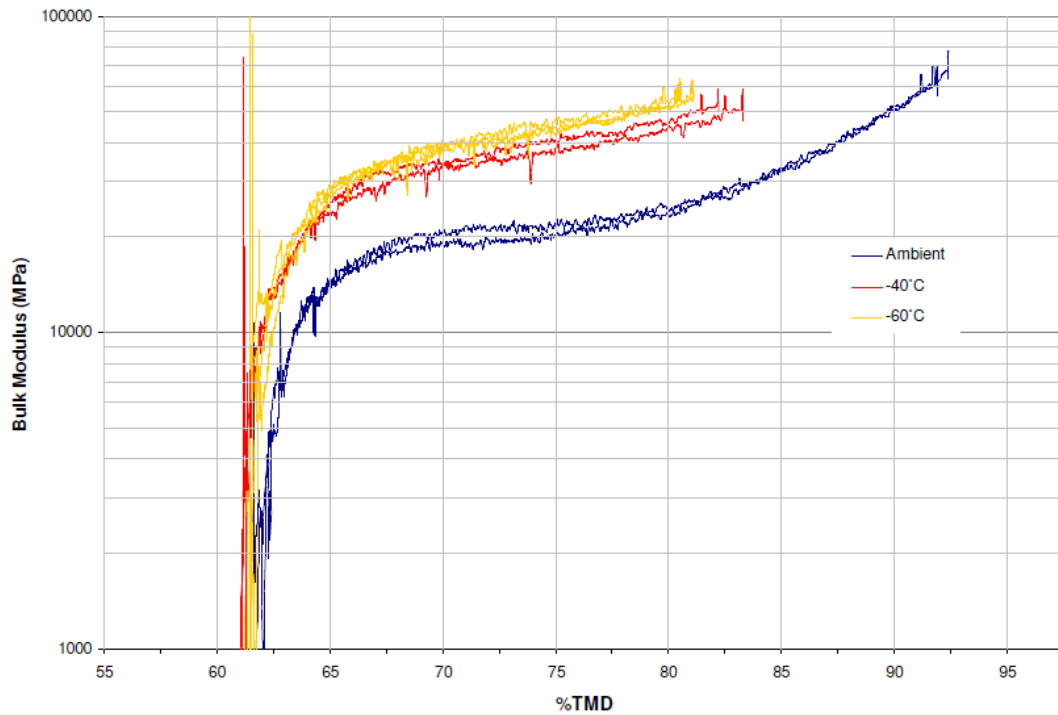


Figure D.2: AR2211 bulk modulus versus %TMD results at ambient, -40°C and -60°C testing temperatures. Only results within ± 0.5 initial %TMD plotted.

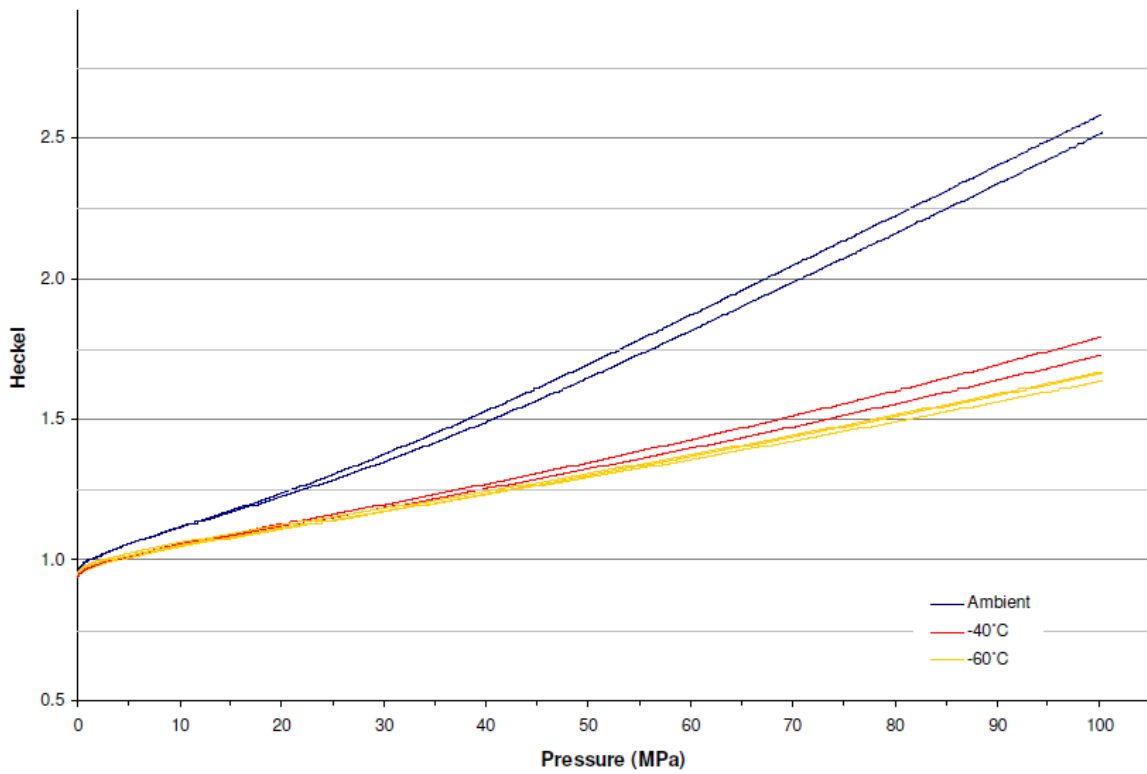


Figure D.3: AR2211 Heckel plot for results at ambient, -40°C and -60°C testing temperatures. Only results within ± 0.5 initial %TMD plotted.

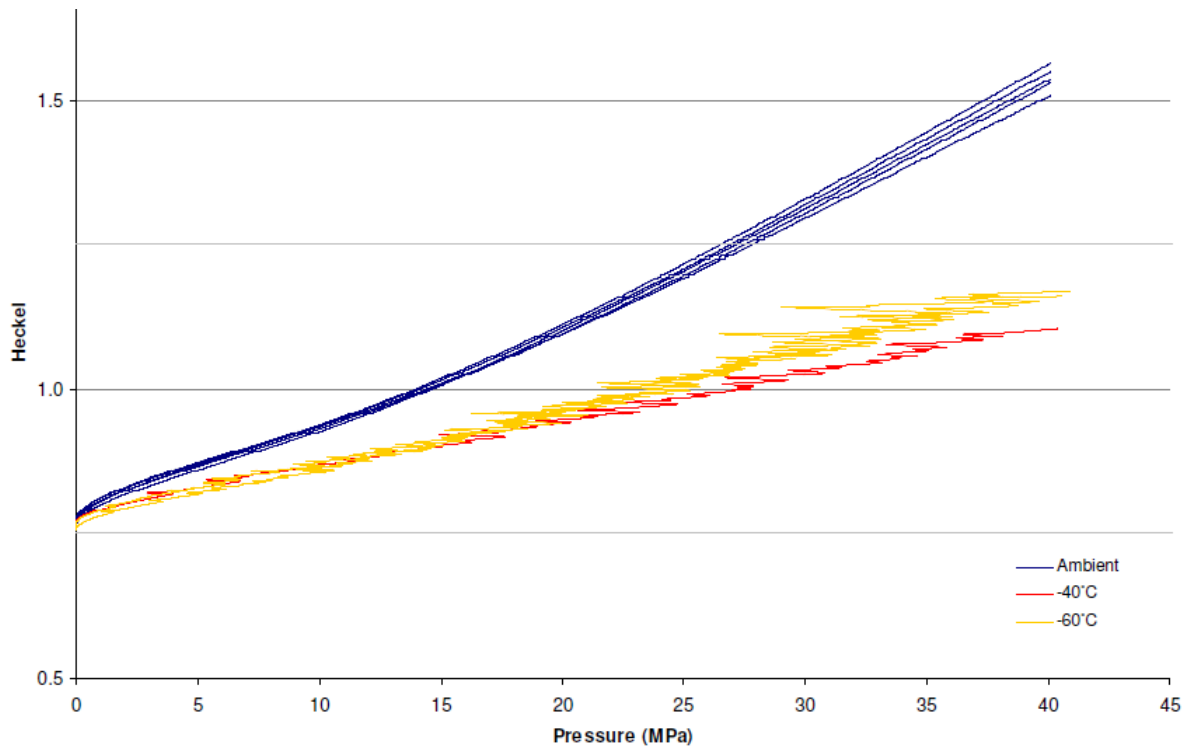


Figure D.4: FNH-025 Heckel plot for results at ambient, -40°C and -60°C testing temperatures. Only results within ± 0.5 initial %TMD plotted.

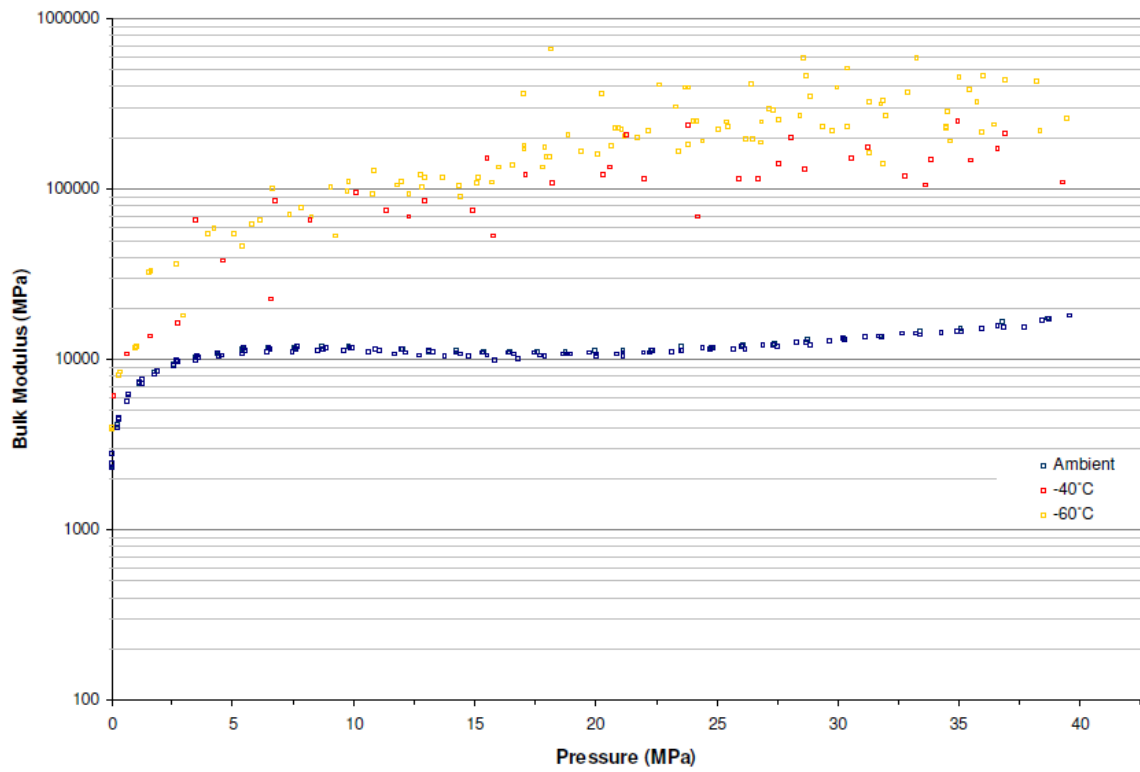


Figure D.5: FNH-025 bulk modulus (local maximum) versus pressure results at ambient, -40°C and -60°C testing temperatures. Only results within ± 0.5 initial %TMD plotted.

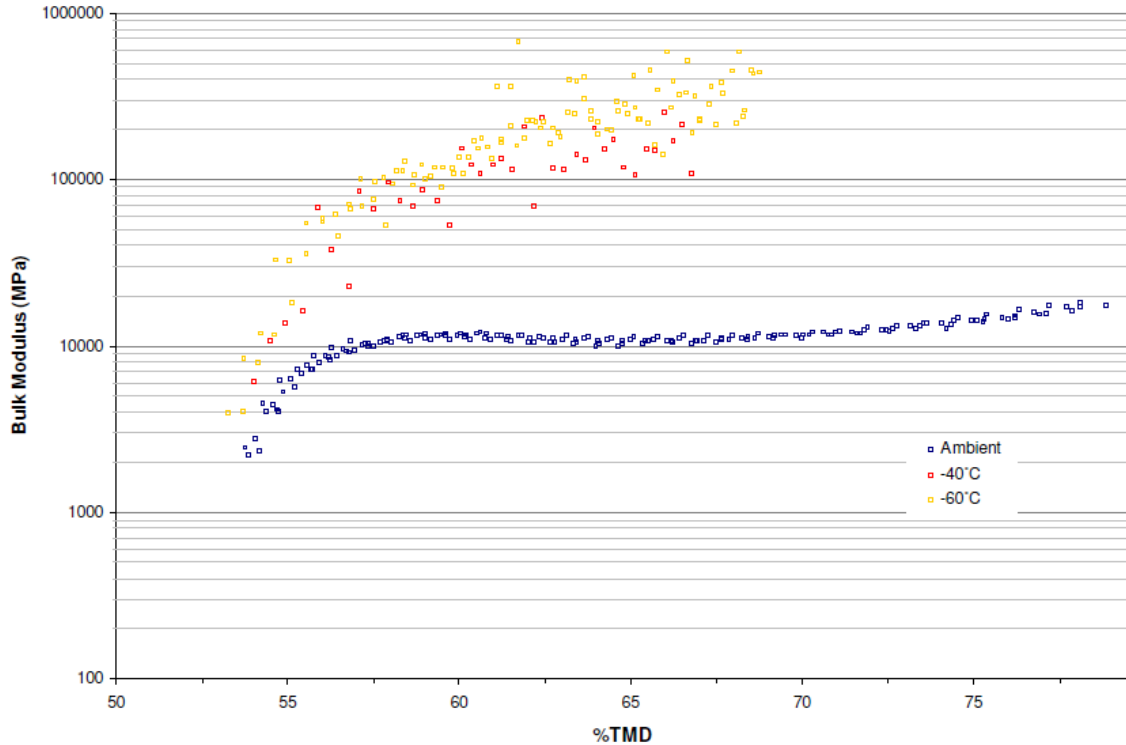


Figure D.6: FNH-025 bulk modulus (local maximum) versus %TMD results at ambient, -40°C and -60°C testing temperatures. Only results within ± 0.5 initial %TMD plotted.

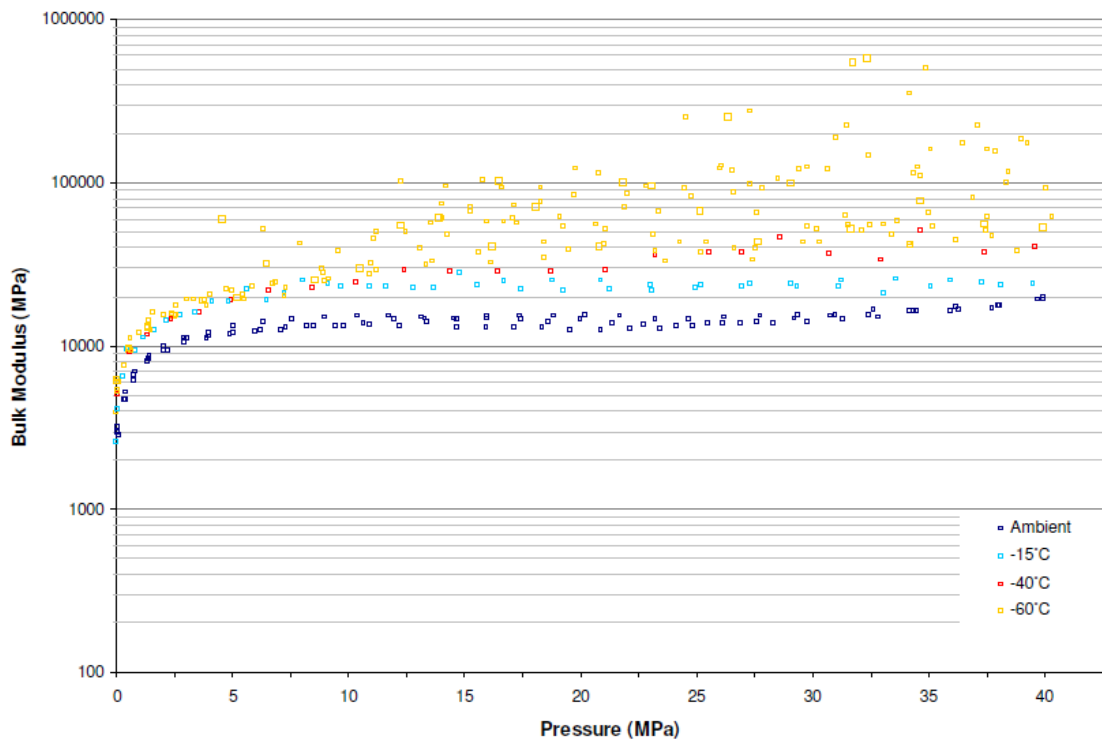


Figure D.7: BS-NACO bulk modulus (local maximum) versus pressure results at ambient, -15°C, -40°C and -60°C testing temperatures. Only results within ± 0.5 initial %TMD plotted.

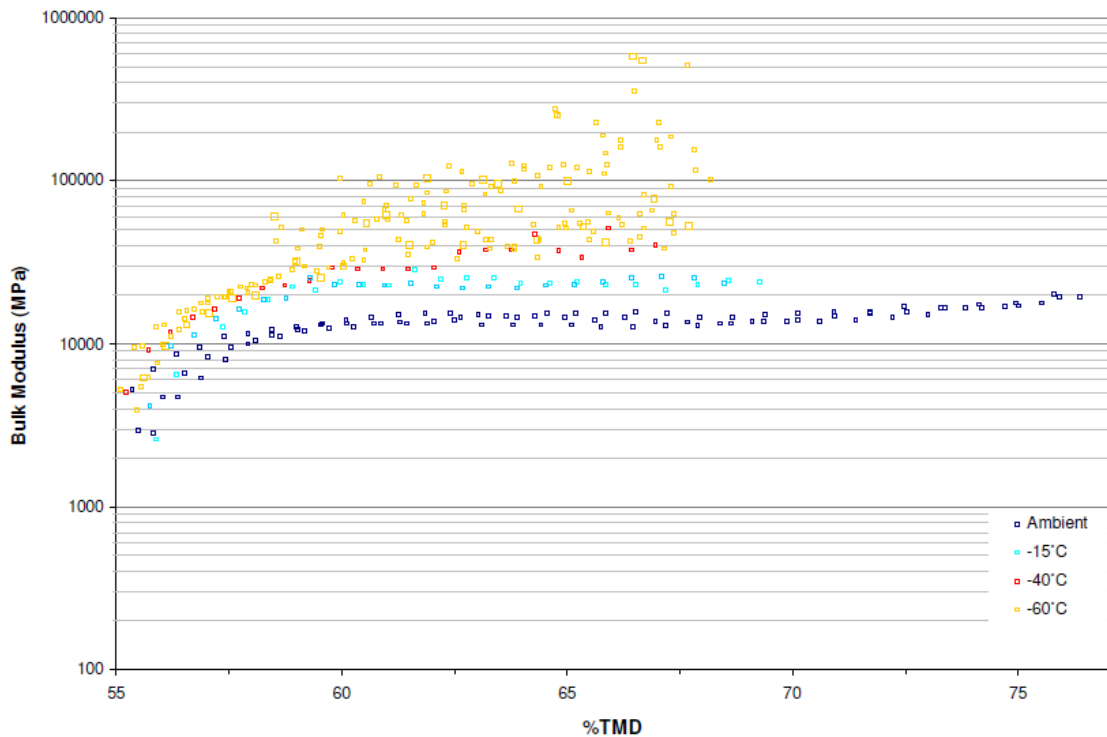


Figure D.8: BS-NACO bulk modulus (local maximum) versus %TMD results at ambient, -15°C, -40°C and -60°C testing temperatures. Only results within ± 0.5 initial %TMD plotted.

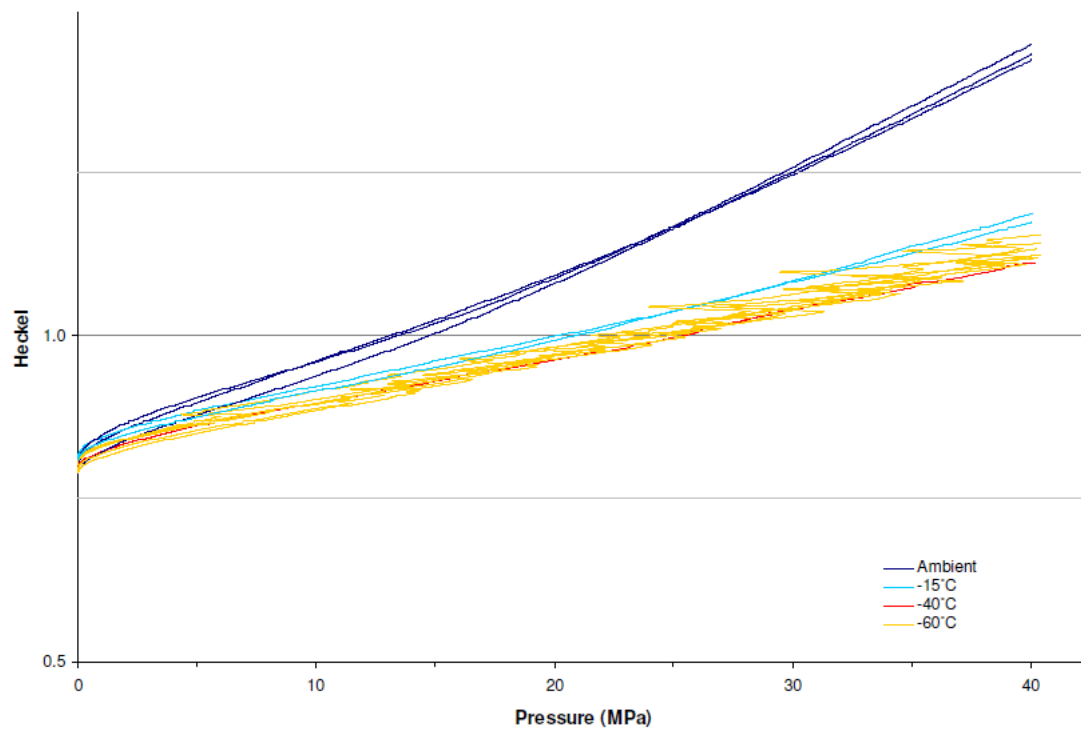


Figure D.9: BS-NACO Heckel plot for results at ambient, -15°C, -40°C and -60°C testing temperatures. Only results within ± 0.5 initial %TMD plotted.

UNCLASSIFIED

DEFENCE SCIENCE AND TECHNOLOGY GROUP DOCUMENT CONTROL DATA			
		1. DLM/CAVEAT (OF DOCUMENT)	
2. TITLE Development of a Low Strain-Rate Gun Propellant Bed Compression Test and its Use in Evaluating Mechanical Response		3. SECURITY CLASSIFICATION (FOR UNCLASSIFIED REPORTS THAT ARE LIMITED RELEASE USE (U/L) NEXT TO DOCUMENT CLASSIFICATION) Document (U) Title (U) Abstract (U)	
4. AUTHOR(S) Joel R. Mortimer, Andrew H. Hart, Joel Huf		5. CORPORATE AUTHOR Defence Science and Technology Group PO Box 1500 Edinburgh SA 5111	
6a. DST Group NUMBER DST-Group-TR-3291	6b. AR NUMBER AR-016-684	6c. TYPE OF REPORT Technical Report	7. DOCUMENT DATE September 2016
8. Objective ID AV14506802	9. TASK NUMBER CDF 16/0036	10. TASK SPONSOR MunSPO	
13. DOWNGRADING/DELIMITING INSTRUCTIONS		14. RELEASE AUTHORITY Chief, Weapons and Combat Systems Division	
15. SECONDARY RELEASE STATEMENT OF THIS DOCUMENT <p style="text-align: center;"><i>Approved for Public Release</i></p>			
16. DELIBERATE ANNOUNCEMENT No limitations			
17. CITATION IN OTHER DOCUMENTS Yes			
18. RESEARCH LIBRARY THESAURUS Propellants; mechanical properties; mechanical testing; strain rate; ageing tests			
19. ABSTRACT The mechanical integrity of the propellant bed is a key factor in safe and consistent gun performance. To inform in this regard, a low strain-rate bed compression test was developed, primarily for use at low temperatures and, in conjunction with the time-temperature superposition principle, to simulate the high strain rates that exist in the gun chamber during ignition. A range of single-base propellants was used to determine the appropriate test temperature, strain rate and maximum load to, as close as possible, simulate the mechanical response of the propellant bed during ignition in the gun. Results of this testing are given in terms of visual fracture categorisation, applied stress versus bed density, relative vivacity (following burning of crushed and reference samples) and stress relaxation. Artificial ageing programs were also employed to develop relationships between propellant mechanical integrity and propellant molecular weight distributions as a function of age.			

UNCLASSIFIED